

Computational Methods for Structure-Property Relations in Heterogeneous Materials

Submitted in partial fulfillment of the requirements for

the degree of

Doctor of Philosophy

in

Computational Mechanics

Xiaoyao Peng

B.S. Civil Engineering, Shijiazhuang Tiedao University

M.S. Civil Engineering, Carnegie Mellon University

Carnegie Mellon University

Pittsburgh, PA

May 2021

This page intentionally left blank.

Keywords: grain growth, dislocation motion, phase field, homogenization.

*Dedicated to my parents, who want nothing but me being happy,
and to Hong, my favorite person in the whole world, you make me happy.*

Acknowledgements

I would like to take this opportunity to express my sincere gratitude to my advisors, Prof. Kaushik Dayal (committee chair) and Dr. Abigail Hunter. It has been a wonderful journey studying and doing research with them. The lessons in the past four years from them will be always treasured and motivate me in the future. I would also like to thank the members of my proposal and defense committee, Prof. Matteo Pozzi, Prof. Carmel Majidi, Prof. Hae Young Noh, and Prof. M. Ravi Shankar for their time and valuable suggestions. A special thank you to all my collaborators, Prof. Gregory Rohrer, Prof. Robert Suter, Dr. Aditi Bhattacharya, Dr. Nithin Mathew, Dr. Ricardo Lebensohn, Prof. Enrique Martinez and Prof. Irene J. Beyerlein, whom I enjoy working with.

My deepest thanks go to my parents Min and Yong. They showed me constant support and understanding. And to Hong, for not disrupting me when I was writing this dissertation and being the only person that is capable of doing so.

I am also thankful to my friends from the MMC group, Esteban, Kshiteej, Mina, Kiana, Ankit, Sulagna, Janel. I want to express special thanks to Esteban for always pushing my limits in the gym and ruining my diet with cakes, to Kshiteej for always being there for me even though his jokes are not as funny as he thinks, and to Bhakti for planning interesting weekend events with me during this pandemic. A huge thank you to my dearest and first friend at CMU, Jaime, and all the friends I am lucky to meet at Pittsburgh, Isa, Ana, Luke, Jiaan, Tania, Carolyn and last but not least my friends from China, Jiahui, Boya, Yalan, Xiangwei, Min, Yan and Shanshan. I can not imagine my time at CMU without their cheers and encouragements.

I would also like to extend special thanks to Maxine Leffard and David Vey for their efforts and help over the last few years.

I acknowledge support from NSF DMREF program (1628994), XSEDE program (TG-DMR120046), the Materials project within ASC-PEM program and Institute of Material Science at Los Alamos National Laboratory.

Abstract

The overall theme of the research is focused on the behavior of heterogeneous functional and structural materials; more specifically, on new computational methods for the prediction of structure-property relations in settings that existing methods cannot handle. Under this theme, there are three distinct though related projects:

(1) **Grain Evolution with Experimentally-derived Interface Properties.** Threshold dynamics model is applied to simulate 3D isotropic grain growth with experiment data. The simulations use the reconstructed microstructures from experiment of a nickle sample before annealing as the input, and try to match the experimentally observed microstructures at different anneal states. Statistical analyses on both simulated and observed microstructures are conducted and compared. While the isotropic simulations are validated to promote grain growth isotropically, it cannot fully reproduce the observed microstructures. Possible reasons for the mismatch are studied and presented.

(2) **Modeling of Dislocation Dynamics in Metals.** The 3D Phase Field Dislocation Dynamics (PFDD) model is extended to body-centered cubic (BCC) metals by accounting for the dependence of the Peierls barrier on the line-character of the dislocation. Simulations of the expansion of a dislocation loop belonging to the $\{110\} \langle 111 \rangle$ slip system are presented with direct comparison to Molecular Statics (MS) simulations. The extended PFDD model is able to capture the salient features of dislocation loop expansion predicted by MS simulations. The model is also applied to simulate the motion of a straight screw dislocation through kink-pair motion. Furthermore, PFDD formulation is adapted to use non-orthogonal grids that are constructed with lattice primitives. Simulations with the non-orthogonal grids show improved performance when comparing to the rotated grids used before. A test with two dislocation loops on two non-coplanar slip planes annihilating each other demonstrates the advantages of using the non-orthogonal grids.

(3) **Computational Methods for High-contrast Composites.** This project applies the Recursive Projection Method (RPM) to the problem of finding the effective mechanical response of a periodic heterogeneous solid. Previous works apply the Fast Fourier Transform (FFT) in combination with various fixed-point methods to solve the problem on the periodic unit cell. These have proven extremely powerful in a range of problems ranging from image-based modeling to dislocation plasticity. However, the fixed-point iterations can converge very slowly, or not at all, if the elastic properties have high contrast, such as in the case of voids. The

reasons for slow, or lack of convergence, are examined in terms of a variational perspective. In particular, when the material contains regions with zero or very small stiffness, there is lack of uniqueness, and the energy landscape has flat or shallow directions. Therefore, in this work, the fixed-point iteration is replaced by the RPM iteration. The RPM uses the fixed-point iteration to adaptively identify the subspace on which fixed-point iterations are unstable, and performs Newton iterations only on the unstable subspace, while fixed-point iterations are performed on the complementary stable subspace. This combination of efficient fixed-point iterations where possible, and expensive but well-convergent Newton iterations where required, is shown to lead to robust and efficient convergence of the method. In particular, RPM-FFT converges well for a wide range of choices of the reference medium, while usual fixed-point iterations are usually sensitive to this choice.

Contents

Acknowledgements	iv
Abstract	v
List of Figures	x
List of Tables	xiv
1 Introduction	1
1.1 Grain Evolution with Experimentally-derived Interface Properties	1
1.2 Modeling of Dislocation Dynamics in Metals	3
1.2.1 A 3D Phase Field Dislocation Dynamics Model for Body-centered Cubic Crystals . .	4
1.2.2 Non-orthogonal Computational Grids for Studying Dislocation Motion in Phase Field Approaches	7
1.3 Computational Methods for High-contrast Composites	8
2 Grain Evolution with Experimentally-derived Interface Properties	13
2.1 Methods	13
2.1.1 Threshold Dynamics	13
2.1.2 Model Validation	15
2.1.3 Data Processing for Comparison	17
2.1.3.1 Establishing the common volume.	17
2.1.3.2 Establishing the time scale.	18
2.2 Results	20

2.3	Conclusions	27
3	Modeling of Dislocation Dynamics in Metals	28
3.1	A 3D Phase Field Dislocation Dynamics Model for Body-centered Cubic Crystals	28
3.1.1	Phase Field Dislocation Dynamics (PFDD)	28
3.1.2	Extension to BCC Metals	31
3.1.2.1	Calculating the Dislocation Line Sense.	31
3.1.2.2	Defining the Transition between Edge and Screw Type.	33
3.1.3	Molecular Statics Simulations	35
3.1.4	Results and Discussion	37
3.1.4.1	Expansion of a Perfect Dislocation Loop.	39
3.1.4.2	Propagation of a Straight Screw Dislocation through Kink-Pair Motion. . .	43
3.1.5	Conclusions	43
3.2	Non-orthogonal Computational Grids for Studying Dislocation Motion in Phase Field Approaches	46
3.2.1	Incorporation of Varying Computational Grids	46
3.2.2	Results and Discussion	49
3.2.2.1	Loop expansion tests on three grids.	51
3.2.2.2	Two loop annihilation test on non-orthogonal grid.	54
3.2.3	Conclusions	56
4	Computational Methods for High-contrast Composites	58
4.1	Classical FFT Method Based on Fixed-Point Iteration	58

4.2	The Proposed RPM-FFT Method	60
4.3	A Variational Perspective	64
4.3.1	Fixed-Point Iterations as Gradient Descent	67
4.4	Numerical Comparisons Between Classical FFT, Accelerated FFT, and RPM-FFT	69
4.4.1	Time to Convergence vs. Elastic Contrast	70
4.4.2	Balancing Newton Iterations against Fixed Point	71
4.4.3	Effect of Volume Fraction and Problem Size	72
4.4.4	Interaction Between Stiff Fibers	74
4.4.5	RPM Applied to the Accelerated FFT Method	76
4.5	Conclusions	79
5	Summary	82

List of Figures

1	Grain size distributions of simulations at different annealing stages.	16
2	$\langle R \rangle^2 - \langle R_0 \rangle^2$ as a function of iteration step.	16
3	Twin-boundary-merged orientation map of the Ni sample at anneal state 0. The size of the map is $369 \times 372 \times 62$. Grains are colored by their orientations. Voxels marked in red do not belong to any grain.	17
4	Left: experimentally measured microstructure of anneal state 0 of 921 grains, middle: experimentally measured microstructure of anneal state 1 of 756 grains and right: the simulated microstructure of the anneal state 1 with 601 grains.	20
5	Visualization of a bulk grain across all anneal states in experiment and simulations. The top row shows experiment grains starting from An 0 to An 5 and the bottom row shows the simulated grains from An 1 to An 5.	21
6	Change in volume versus the difference between the number of neighbors and the average number of neighbors of the neighbors in (a) experiment and (b) simulation. For each class of $F - \langle F_{NN} \rangle$, the marker is the mean value and the bar shows one standard deviation of the distribution.	22
7	The grain size distribution and grain volume distribution of experimental and simulation microstructures for all the anneal states.	22
8	The distribution of fractional change in volume for experimental and simulated grains. . . .	23
9	The fractional change in volume vs grain size in experimental and simulated grains.	24
10	The triangle curvatures for all boundaries in the simulation and experiment.	25
11	The volume prediction error as a function of topological error.	26

12	A dislocation loop (black curve surrounding the slipped region (denoted in blue)) with a Burgers vector \mathbf{b} . The gradient of the order parameter $\nabla\zeta^\alpha$ lies in the plane formed by dislocation line normal \mathbf{n} and slip plane normal \mathbf{m}	32
13	Energy barrier $B_o\beta(\theta)$ as a function of line character angle θ for Ta and Nb.	35
14	$\langle 111 \rangle$ trace of the γ -surfaces predicted by MS simulations for Ta and Nb. Note the shallow minima in Nb.	37
15	Figure (a) presents a schematic of the 3D simulation cell for the PFDD simulations of expansion of a single dislocation loop. Figure (b) presents the initial conditions on the glide plane for these simulations.	38
16	Figure (a) presents a schematic of the 3D simulation cell for the PFDD simulations propagation of a kink pair. Figure (b) presents the initial conditions on the glide plane for this simulation.	39
17	Ta loop expansion snapshots in (a) PFDD (b) MS at normalized time $t = 0, 0.2, 0.4$. The time for each snapshots is normalized with respect to the time that loops reach their steady state. The loops are colored by character with screw-type dislocation shown in red, and edge-type dislocations shown in blue.	40
18	Nb loop expansion snapshots in (a) PFDD (b) MS at normalized time $t = 0, 0.2, 0.4$. Time for each snapshots is normalized with respect to the time that loops reach their steady state. The loops are colored by character with screw-type dislocation shown in red, and edge-type dislocations shown in blue.	41
19	Quantitative comparisons between PFDD and MS for Ta and Nb: (a) Ratio of major to minor axis of dislocation loop (b) Fraction of screw segment.	42
20	PFDD simulation of screw dislocation motion by propagation of kinks with edge character. Snapshots are shown at normalized time, $t = 0, 0.2, 0.3, 1.0$	44
21	An example of the rotated, cubic and non-orthogonal grids for FCC crystallography. The red lines indicate the $\langle 111 \rangle$ slip planes.	47

22	Stresses normalized with shear modulus left: σ_{xx} , middle: σ_{zz} , right: σ_{xz} of a Cu straight edge dislocation $[1\bar{1}0](111)$ calculated with PFDD rotated and cubic grids and compared to the analytical solution. σ_{xx} and σ_{zz} are plotted along $z[111]$ direction and σ_{xz} is plotted along $x[1\bar{1}0]$ direction at the dislocation.	50
23	Stresses normalized with shear modulus left: σ_{xx} , middle: σ_{zz} , right: σ_{xz} of a Cu straight edge dislocation $[1\bar{1}0](111)$ calculated with analytical solution, the PFDD rotated grid $64b \times 64b \times 64b$ and the refined rotated grid $256b \times 256b \times 256b$. σ_{xx} and σ_{zz} are plotted along $z[111]$ direction and σ_{xz} is plotted along $x[1\bar{1}0]$ direction at the dislocation.	51
24	Cu dislocation loops on the (111) slip planes of (a) rotated grid (b) cubic grid and (c) non-orthogonal grid. The sizes of the loops are $r = 10b$ and the lengths of the dashed yellow lines which follow the b direction are $64b$	52
25	Stresses normalized with shear modulus left: σ_{xx} , middle: σ_{zz} , right: σ_{xz} of a Cu dislocation loop $[1\bar{1}0](111)$ calculated with the non-orthogonal grid, the cubic grid and the rotated grid at step 0. σ_{xx} and σ_{zz} are plotted along $z[111]$ direction and σ_{xz} is plotted along $x[1\bar{1}0]$ direction at the edge segments.	53
26	Dislocation loops in (a) rotated (b) cubic and (c) non-orthogonal grids at step 100. Top row shows the loops on their slip plane and bottom row shows the zoomed-in loop shapes. . . .	54
27	Stresses normalized with shear modulus left: σ_{xx} , middle: σ_{zz} , right: σ_{xz} of a Cu dislocation loop $[1\bar{1}0](111)$ calculated with the non-orthogonal grid, the cubic grid and the rotated grid at step 100. σ_{xx} and σ_{zz} are plotted along $z[111]$ direction and σ_{xz} is plotted along $x[1\bar{1}0]$ direction at the edge segments.	54
28	Stresses normalized with shear modulus left: σ_{xx} , middle: σ_{zz} , right: σ_{xz} of a Cu dislocation loop $[1\bar{1}0](111)$ calculated with the cubic grid, the refined cubic grid and the non-orthogonal grid at step 0. σ_{xx} and σ_{zz} are plotted along $z[111]$ direction and σ_{xz} is plotted along $x[1\bar{1}0]$ direction at the edge segments.	55

29	Two dislocation loops on non-coplanar slip systems in the non-orthogonal grid. Both loops have the same slip direction, $[1\bar{1}0]$, and different slip plane normals: (111) (red loop) and $(11\bar{1})$ (blue loop).	55
30	Snapshots of two dislocation loops expanding in the non-orthogonal grid. The loops expand, meet and annihilate at screw segment marked in white.	56
31	Snapshots of two dislocation loops expanding in the cubic grid. The loops expand, meet but do not annihilate.	57
32	Top row: ϵ_{12} component of the strain using Classical FFT (left) and RPM-FFT (center) methods. Bottom row: the figure on the right shows ϵ_{12} along the horizontal symmetric axis for both RPM-FFT and Classical FFT; the figure on the left shows the normalized difference. The geometry is given by $a/b = 1/16$, and the figure shows only the region in the vicinity of the fiber. The mesh is 2048×2048 . We use $E_f = 68.9\text{GPa}$ and $E_m = 400\text{GPa}$; the contrast $K \approx 5.8$. We apply shear loading: $E_{12} = 0.5\%$, $E_{11} = E_{22} = 0$	70
33	Time at convergence of three methods with varying K . Note the log scale. The lines are linear best fits.	71
34	Time at convergence of RPM with fixed $n_{max} = 10$ and $n_{max}^{best}(K)$. The lines are linear best fits.	73
35	The best n_{max} for different problem sizes. The line connects datapoints to aid visualization.	74
36	Time to convergence of RPM-FFT with varying λ and K . The lines connect the datapoints to aid visualization.	75
37	Size of unstable subspace with problem size. The lines connect the datapoints to aid visualization.	76
38	Energy density (top row) and ϵ_{11} (bottom row) for almost-rigid fibers, when the fibers are near and far away from each other.	77
39	Number of iterations and times to convergence as a function of reference medium modulus E_o . We examine $K = 10, 10^2, 10^3, 10^4$ in the first, second, third and fourth rows respectively.	80

List of Tables

1	Material parameters calculated from MS simulations and corresponding Young's modulus E , shear modulus G , and Poisson's ratio ν calculated with the Voigt isotropic approximation. All elastic coefficients are specified in units of GPa.	36
2	FCC and BCC non-orthogonal lattice primitive vectors.	47
3	Material parameters in the Voigt form. All elastic coefficients are specified in units of GPa. .	49
4	Number of iterations and time to convergence for the Accelerated-FFT and RPM-Accelerated-FFT for a wide range of K	78

1 Introduction

The three projects that compose the PhD dissertation are all related to the topic of Computational Methods for Structure-Property Relations in Heterogeneous Materials. The dissertation is organized as follows:

- Section 1.1 and Section 2 present the work related to **Grain Evolution with Experimentally-derived Interface Properties**;
- Section 1.2 and Section 3 present the work related to **Modeling of Dislocation Dynamics in Metals**;
- Section 1.3 and Section 4 present the work related to **Computational Methods for High-contrast Composites**.

In this chapter, the motivations and introductions of these three projects are separately presented.

1.1 Grain Evolution with Experimentally-derived Interface Properties

This is joint work with Prof. Gregory Rohrer and Dr. Aditi Bhattacharya in the Department of Material Science and Engineering and Prof. Robert Suter in the Department of Physics at CMU. All experiments were conducted by the collaborators. My contributions are performing the simulations, validating the model, and comparing the simulated and observed microstructures with the collaborators. Some results here are also presented in Dr. Aditi Bhattacharya's dissertation.

Numerous advanced manufacturing processes for metals – ranging from additive manufacturing to single-crystal growth of turbine blades – use annealing or other heat-treatment processes as the final step to achieve vast improvement in properties. A central feature of all these post-processing methods is that they cause the microstructure of polycrystalline materials to change through grain boundary motion, and important physical properties of these materials, such as their yield strength

or electrical conductivity, depend on the grain boundary network structure. This work focus on modeling grain growth during annealing.

The complexity of modeling grain growth lies in many properties of the materials affecting the grain boundary motion. A grain boundary can be determined by 5 parameters, 3 from the mis-orientation between the 2 neighboring grains sharing this boundary and 2 from the inclination of the grain boundary [Sut95]. Local grain boundary velocity depends on its surface energy, mobility and curvature. Except for curvature, which solely depends on the geometry, surface energy and mobility are hard to determine. It has been shown that surface energy is a function of these 5 parameters [Roh11, ROB⁺15]. Some studies of grain boundary velocities of bicrystals suggested that mobility is correlated with the 5 parameters as well [GMS⁺01, RGSM04, GS09], but has not been validated for polycrystalline materials by experiment. Meanwhile, Zhang et al. [ZLZ⁺20] reports no strong correlation between the reduced grain boundary mobility (the product of surface energy and mobility) and the 5 parameters by finding the reduced mobility using phase field simulations with experiment data. This raises the question that what assumptions of these properties should be made in a grain growth model.

Numerous studies are performed to understand grain growth over the years such as Monte Carlo Potts models [SASG84, Sro86], cellular automata models [HG91, Raa05], vertex simulations [BN47, Hum00] and phase field models [KS12, Che02]. In this work, we choose to use threshold dynamics (TD) scheme developed by Merriman et al. [MBO92] and extended to multi-phase anisotropic settings for grain growth simulations by Esedoglu et al. [EO15, EJZ17, EE18]. The reasons come naturally from its benefits: (1) can use experiment image/data directly without additional meshing; (2) implicit representation of the interface as in the phase field or level set methods and tracking topological changes automatically; (3) unconditional stability and high computing efficiency and (4) extension from isotropic formulation to anisotropic formulation can be achieved by replacing isotropic kernel with anisotropic ones constructed with different anisotropic surface energy/mobility forms. All these benefits, especially the last one, give us the flexibility to do isotropic and different anisotropic simulations.

A nickel (Ni) sample with approximately 2,500 grains were measured at 6 anneal states for regular time intervals with near-field high energy X-ray diffraction microscopy [Hef12, HLLS10]. Microstructures of these annealing stages were reconstructed [Li11, Mad16]. The goal of this project is to simulate grain growth by a direct comparison to the experimental data in three dimensions. In this chapter, we use “observed”, “measured”, “reconstructed” and “experimental” interchangeably to refer the reconstructed microstructures from experiments.

As a highly anisotropic metal, Ni has properties such as surface tension, mobility, electrical and magnetic properties varying with crystallographic orientation. The abundant existence of $\Sigma 3$ twin boundaries (about 29% among all boundaries) complicates its grain evolution even more. Thus, to better interpret the experimental microstructure evolution, we start the simulations with isotropic TD scheme. In this framework, each experimental microstructure was modified to merge all grains sharing a twin boundary. This was done to reduce the anisotropy from the odd shaped grains. And the total number of grains is reduced to 921.

While the distributions of grain characteristics between the simulations and experiments match well to each other in general, simulations can not predict individual grain growth correctly. The differences such as volume and topological changes between the isotropic simulated microstructures and the experimental microstructures are investigated and provide insights about what to consider for the anisotropic simulations.

1.2 Modeling of Dislocation Dynamics in Metals

This is joint work with Dr. Abigail Hunter, Dr. Nithin Mathew, Dr. Ricardo Lebensohn at Los Alamos National Laboratory, Prof. Enrique Martinez at Clemson University and Prof. Irene J. Beyerlein at University of California, Santa Barbara. Two topics are covered in this work. **PFDD is extended to BCC metals in Section 1.2.1 and Section 3.1, this part has been published in [PMB⁺20a].** PFDD is adapted to use non-orthogonal grids in Section 1.2.2 and Section 1.2.2, this part is under preparation for publishing.

1.2.1 A 3D Phase Field Dislocation Dynamics Model for Body-centered Cubic Crystals

Dislocations are carriers of plasticity in metals [HB01, HL68, KM03]. While straining, individual crystals, microns across, will contain a collection of dislocations gliding on particular crystallographic slip planes in particular slip directions. They move and are stored heterogeneously throughout the crystal. Dislocations or groups of dislocations have been represented in various ways, atomically including their core to discretely as a line to statistically as a dislocation density to finally crystallographically as slip. Models that represent dislocations discretely, including their Burgers vector and line orientation, have thus far been successful in capturing heterogeneity in slip.

Atomistic approaches, including Molecular dynamics (MD), Molecular Statics (MS), and Density Functional Theory (DFT), are one such example. These methods can model the movement of a few dislocations in small volumes (high dislocation densities) and account for the atomic-scale effects of the dislocation core during motion along with interactions and reactions with other dislocations and boundaries in the system [LeS13, ZRSOB17, WScGI04, WTF13, LBW18]. The chief disadvantage of atomic-scale techniques is that they are limited in the material sizes and time scales they can access.

Moving up in length scale, mesoscale dislocation-dynamics (DD) codes have been emerging over the recent past in an effort to overcome the short time and length scales that limit atomistic methods. These models account for each dislocation as a line in a 3D continuum that interacts with other linear dislocations via elastic fields. The motion and interaction of the individual dislocation lines in a system is modeled over time and under various applied loading conditions. These approaches do not resolve the dislocation lines to the atomic level, hence features such as the dislocation cores cannot be explicitly captured.

One such DD model, classified as discrete DD techniques (DDD), was developed in the late 90s [GTS00, DK97, RZH⁺98, WFVdGN02]. Since then DDD models have become a well-developed approach for modeling a group to several interacting dislocation lines in 3D space. They have been successful in addressing the evolution of many interacting dislocations [ZOAB11, CB04, KDT98,

[WBL08](#), [ZBL11](#)] and the formation of organized dislocation structures in strained crystals. They have also considered a variety of crystal structures including face-centered cubic (FCC), body-centered cubic (BCC) metals and hexagonal close-packed (HCP) metals [[ZdIRRH00](#), [ACT⁺07](#), [BTB⁺14](#), [MDK04](#), [LeS13](#), [BC06](#)]. They were originally developed for bulk crystals but in the past decade have been further developed to account for the barrier effects of interfaces and grain boundaries, twin boundaries, precipitates, and thin films [[EAFH16](#), [HRU⁺17](#), [GFMH15](#)].

In DDD models, the dislocation line is discretized into a finite number of segments, and at each point along the line the equation of motion is solved. Some elementary processes, such as dissociation, climb, non-Schmid effects, or cross slip can be modeled with the help of rules, typically motivated by atomistic simulations, including MS, MD, or DFT [[EABG08](#), [WB11](#), [WBT14](#), [SLB⁺07](#), [WB11](#)]. For instance, the model by Shehadeh *et al.* [[SLB⁺07](#)] incorporates fault energies into the DDD model to simulate slip transmission across an interface, including the possibility of core spreading in the interface. A number of DDD models have incorporated the effects of cross slip [[WBL07](#), [KCC⁺92](#), [WBL08](#)], finding that they lead to formation of slip bands or cellular structures. A recent set of works have applied to examine the effects of precipitates in superalloys [[HRU⁺17](#), [YLH13](#), [HJT12](#), [GFMH15](#)].

Another type of mesoscale mechanics technique for simulating dislocations that has emerged is phase field dislocation dynamics (PFDD). Phase field models have been traditionally used to study phase transformations [[Ste09](#)]. In the last few decades, they have been extended to model dislocation behavior and interactions [[WJCK01](#), [KCO02](#)], giving rise to the name PFDD. PFDD adopts the original basis of phase field models in the sense that system dynamics are directly dependent on minimization of the total system energy. However, in contrast to traditional phase field approaches, the order parameters in PFDD represent individual dislocations rather than different material phases. More specifically, in PFDD, dislocations in each slip system, α , are represented by scalar order parameters, $\zeta^\alpha(\mathbf{x}, t)$; one order parameter per slip plane. At any given point on a slip plane, this phase field parameter records the amount of slip that has occurred due to dislocation motion in units of the Burgers vector [[KCO02](#)]. Transitions in the order parameter can represent the locations of

dislocation lines. A master energy functional is comprised of the elastic strain energy, calculated from continuum linear elastic dislocation theory, and the dislocation lattice energy, which is often informed from atomic scale simulations. The equilibrium positions of the dislocations in the crystal are determined by minimizing this energy functional at every time step. In this way, PFDD enables simulations with much larger crystal sizes and time scales (seconds and 10-100 nanometers), more comparable to those used in experiments, than atomic-scale simulations.

The PFDD model was developed to simulate the evolution of dislocations in any material. Despite this, most PFDD studies have focused on modeling dislocations in FCC materials, with a few modeling BCC dislocations [BH16a, MKO11]. In FCC metals, PFDD studies have considered not only perfect dislocations but also partial dislocations [BH16a, HZB14, HBGK11], heterophase interfaces [ZHBK16, HLB18], and deformation twinning [HB14a, HB15]. In recent years, they have successfully been advanced to model grain boundary sliding [KWLL11], grain boundary dislocation nucleation [HB14b, HZB14], glide in high entropy alloys [ZCK19], formation and glide of partial dislocations in polycrystals [CHBK15], the presence of void space [LMK13], slip transfer across biphasic boundaries [ZHBK16, HLB18], again, all for FCC metals. Recent advancements have been made in predicting dislocation networks in boundaries of BCC metals [QZS⁺19] and transformations to the HCP phase by sequential glide of FCC Shockley partials [LTBL17].

Dislocation motion in FCC materials is fundamentally simpler than that in other metals. First, FCC materials deform predominantly via one slip mode. In comparison, BCC metals have three possible slip modes $\{110\} \langle 111 \rangle$, $\{112\} \langle 111 \rangle$ and $\{123\} \langle 111 \rangle$. Also in contrast to FCC dislocations, the motion of dislocations can be directional, being harder to move in one direction versus another (resulting in the well known tension/compression asymmetry), and can depend on the line-character [UW75, LT62, BH67, TKC98]. These distinctions induce changes in the types of active deformation mechanisms in the metal. For example, low temperature electron microscopy measurements in BCC crystals have shown the presence of long screw dislocations, indicating that non-screw dislocations are more mobile and require a lower resolved shear stress (RSS) for motion [HB01]. Due to the high RSS required, screw dislocations in BCC metals move by nucleation

and propagation of kink-pairs. A kink-pair is first nucleated along the screw-oriented dislocation dislocation line. The kink is bound by a pair of oppositely signed edge oriented components. Due to the low RSS required to propagate edge-oriented dislocations, the sides of the kink can move easily laterally along the dislocation line and the screw dislocation ultimately advances. Thus, to accurately capture dislocation motion in BCC materials, it is important to account for the line-character and capture the dependence of RSS on the line-character.

In this work, we present a 3D PFDD framework that includes dislocation character dependent behavior applicable to BCC metals. The section is structured as follows. First, the PFDD framework traditionally used for perfect dislocation motion in FCC materials is briefly presented in Section 3.1.1. Extensions to account for a line-character dependent Peierls barrier are presented next in Section 3.1.2. Two cases are treated with the extended BCC PFDD model in Section 3.1.4, dislocation loop expansion and the kink-pair motion of a screw dislocation, the former of which is presented with direct comparison to atomistic results.

1.2.2 Non-orthogonal Computational Grids for Studying Dislocation Motion in Phase Field Approaches

Phase Field Dislocation Dynamics (PFDD), as well as many other mesoscale dislocation models [MS15, SW03, BUPC15], use the Fast Fourier Transform (FFT) method [MS98] to solve the stress equilibrium equation. While there are many benefits of using the FFT method, such as high numerical efficiency and easy handling of elastic anisotropy, it also introduces Gibbs oscillations [HH79] which arise from taking Fourier transforms of discontinuous fields. Dislocations induce discontinuous plastic strain/stress fields, so FFT-based mesoscale dislocation models all face the Gibbs effect. Many studies developed effective treatments to suppress the oscillations such as using a “centered” [DMO99] and/or a “rotated” [Wil15] Green operator.

The easiest configuration of a computational grid for dislocations would be having a orthogonal grid that is rotated from the Cartesian grid such that the slip plane is perfectly aligned with the

grid plane. This simplifies assigning the initial configuration and computational work. In Figure 21, the rotated grid has one slip plane (111) aligned with its xy plane, but the same slip plane in the cubic/Cartesian grid is inclined. An inclined slip plane can produce more numerical errors (shown in Section 3.2.2) from the FFT method, which can impact the overall solution. However, when modeling a more complex structure with multiple slip planes and one slip plane is aligned with the rotated grid, then the other planes are bound to be inclined. In this work, we present a new non-orthogonal computational grid that is constructed with lattice primitives. The new non-orthogonal grids can accommodate multiple slip planes in either the face centered cubic (FCC) or body centered cubic (BCC) crystallographic systems. In these computational grids all the slip planes align with point within the computational grid, thus avoiding the possible numerical errors induced by the inclined slip plane.

1.3 Computational Methods for High-contrast Composites

This is joint work with experimentalists at Air Force Research Laboratory, led by Dr. Dhriti Nepal's group in the Composites Branch. This work has been published in [PND20].

This project proposes and applies the Recursive Projection Method (RPM) – a method to adaptively combine Newton and fixed-point iterations – to the problem of finding the effective mechanical response of a periodic heterogeneous linear elastic solid. Specifically, given the average strain or stress, the goal is to compute the stress and strain distribution within the unit cell. While the linear elastic setting is of interest in itself, it is also used extensively as part of the iterative solution process in nonlinear elastic or inelastic settings.

Early numerical works in the periodic setting exploited Fast Fourier Transforms (FFT)¹ to partially simplify the problem; however, due to the heterogeneity of the elastic properties, the problem is not completely decoupled in Fourier space. Therefore, fixed-point methods are used to complete

¹Following common practice in this field, we denote also the class of algorithms that use Fast Fourier Transforms as FFT methods.

the solution process [MS94, MS98, MMS99]. This approach was used to compute the effective properties of heterogeneous materials that are linear, or nonlinear through iteration. However, while the method is extremely fast for small elastic contrasts, the convergence is slow or even lost for higher elastic contrasts. This rules out systems such as materials with voids, where the void is treated as a part of the body with zero stiffness, for instance. This led to the formulation of the Accelerated FFT Method in [MMS01], based on a scheme proposed in [EM99] for scalar conductivity problems, that modified the original method to handle high contrast composites. A further refinement, proposed in [MB12], is the Polarization FFT Method, which has been shown to be a special case of a general class of methods in [MS14]. A separate promising approach is [PL13], based on ideas from energy minimization, though they do not test it on the case of large elastic contrasts.

These methods have been applied in a variety of settings, including in highly nonlinear problems where they are used in each step of the iteration. For instance, in the context of plasticity, we mention application at the macroscale [Leb01, LR20], to continuous dislocation models [BH16b, PMB⁺20b], as well as recent seminal work in coupling discrete dislocations with fast calculation of elastic interactions [GRL16]. Another important area of application is to phase-field models of microstructure formation in multifunctional materials, e.g. [CS13]. The Fourier methods have also proven powerful in simulating experimental images of microstructure because of the ability to apply the method directly on image data without needing the identification of material boundaries and related challenges [PMG⁺15].

The methods mentioned above – starting from the original FFT method to the Accelerated and Polarization FFT methods – are based on fixed-point methods or variations thereof; see [MS14] for a summary. Consequently, though some of these methods can converge for large elastic contrasts, the convergence gets slower as the contrast increases. In addition, an important part of these methods is the notion of a homogeneous reference medium (for details, see Section 4.1). The notion of a reference medium goes back to [Esh59], and has proven to be a powerful concept in homogenization analysis [AP13, Lip93]. However, in the numerical setting, the convergence of the fixed-point

methods can be very sensitive to the choice of the reference medium. These reasons motivate the proposed work in applying the RPM to this problem.

A classical result is that the solution of the elasticity problem can be posed as a minimization of the strain energy density under standard assumptions, e.g. [Cia88]. That is, the balance of linear momentum, represented by $\operatorname{div} \boldsymbol{\sigma} = \mathbf{0}$ where $\boldsymbol{\sigma}$ is the stress and \mathbf{y} is the deformation, is equivalent to $\min_{\mathbf{y}} \int_{\Omega} W(\nabla \mathbf{y})$, where W is the elastic energy density, Ω is the domain, and $\frac{\partial W}{\partial \nabla \mathbf{y}} = \boldsymbol{\sigma}$. For simplicity, we have assumed displacement fixed on the entire boundary. The perspective that the solution of the equilibrium equation is equivalent to the minimization of strain energy leads to useful insights into the solution methods. In particular, consider the case of a heterogeneous elastic material with voids. Typically, the voids are not taken to be part of the body Ω , and instead they are defined through interior surfaces that are traction-free. However, in the FFT method, one cannot easily treat the voids in this manner because the discretization must be uniform for efficiency; hence, the voids are taken to be part of Ω , and treated as regions with zero stiffness. The zero stiffness regions imply that there is infinite elastic contrast, but also *loss of uniqueness* of the solution.

The uniqueness of solutions is an elementary calculation in linear elasticity, e.g. [Cia88]. Assuming a boundary value problem with 2 solutions \mathbf{y}_1 and \mathbf{y}_2 , it can be shown that the difference $\mathbf{u} := \mathbf{y}_1 - \mathbf{y}_2$ satisfies $\int_{\Omega} \boldsymbol{\epsilon}_{\mathbf{u}} : \mathbf{C} \boldsymbol{\epsilon}_{\mathbf{u}} = 0$, where \mathbf{C} is the linear elastic stiffness tensor, and $\boldsymbol{\epsilon}_{\mathbf{u}}$ is the small strain associated with \mathbf{u} . If \mathbf{C} is pointwise positive-definite, then $\boldsymbol{\epsilon}_{\mathbf{u}} \equiv 0$, and we have uniqueness up to rigid motions; Dirichlet boundary conditions on a finite part of the boundary fixes the rigid motion.

From a heuristic perspective, the lack of uniqueness of the solution in a material with zero-stiffness regions is reasonable: the fictitious material points in the void region can have arbitrary displacement (while respecting the required smoothness), and this does not cost any elastic energy or affect the physics of the problem. Hence, we can expect soft or flat directions in energy landscape. When we have large elastic contrast due to regions with very low stiffness, the energy will be shallow

though perhaps not completely flat. Convergence along these directions can be exceedingly slow, or even lost, in a fixed-point method.

We briefly note that for rigid inclusions, the strain within the rigid objects must vanish, while the stress can be arbitrary as long as smoothness and equilibrium are satisfied. The discussion above can be readily adapted to this setting using the *complementary* strain energy density.

Given the expectation that the energy landscape is flat or shallow in some directions, the use of Newton or similar iterations is likely to provide convergence within a relatively small number of iterations. However, each Newton iteration is far more expensive than a fixed-point iteration, and increasingly so as the dimension of the solution space increases. The RPM, proposed in [SK93], provides the possibility of a balance between the fixed-point and the Newton methods. The first key aspect of RPM is that it uses the fixed-point iterations to adaptively identify the unstable subspace. That is, starting from the assumption that fixed-point methods will converge when applied to the problem, RPM examines successive outcomes from the fixed-point iteration scheme to discern if, and how, the basis of the unstable subspace should be augmented. The second key aspect of RPM is that as the unstable subspace is built up, Newton iterations are performed on the unstable subspace. This enables a balance between the less expensive but non-converging fixed-point method and the more expensive but better converging Newton method.

We point out that while Newton iterations are performed only on the unstable subspace, the fixed-point iterations are performed on the *entire* space. The reason to perform fixed-point iterations not only on the stable subspace, but rather on the entire subspace which is slightly more expensive, is that it enables the use of existing fixed-point methods with minimal changes to existing code and algorithm. In fact, we exploit this feature to apply RPM to both the original FFT method [MS98] as well as to the Accelerated FFT method [MS14].

Briefly, the key outcomes of our comparisons of RPM-FFT with the existing methods is that the RPM-FFT method is faster than the other methods for large elastic contrasts. However, an even more important advantage appears to be that the convergence of RPM-FFT is very robust with

respect to the choice of the reference homogeneous material, whereas the fixed-point methods are sensitive to this choice; this is particularly important since there are only some heuristic ideas about how to optimally choose the reference material.

For brevity, we refer below to the method proposed in this project as *RPM-FFT*; the conventional algorithm from [MS98] as *Classical FFT*; the method proposed in [MMS01] as *Accelerated FFT*; and the method proposed in [MB12] as *Polarization FFT*.

2 Grain Evolution with Experimentally-derived Interface Properties

This is joint work with Prof. Gregory Rohrer and Dr. Aditi Bhattacharya in the Department of Material Science and Engineering and Prof. Robert Suter in the Department of Physics at CMU. All experiments were conducted by the collaborators. My contributions are performing the simulations, validating the model and comparing the simulated and observed microstructures with the collaborators. Some results here are also presented in Dr. Aditi Bhattacharya's dissertation.

This chapter is organized as follows: Section 2.1 summarizes threshold dynamics scheme (TD), validates it with classical theories of isotropic grain growth and describes data processing for comparison; Section 2.2 presents the simulated and observed microstructures comparisons.

2.1 Methods

First, we review TD both in a two-phase and multi-phase settings in Section 2.1.1. To validate the model, grain size distribution and average grain size at different simulation steps are plotted in Section 2.1.2. Comparisons are made possible by establishing the common volume and time scale between the simulation and experiment in Section 2.1.3.

2.1.1 Threshold Dynamics

In TD, phases can be represented through the characteristic function (order parameter) $\mathbf{1}_{\Sigma_i}$ of each phase Σ_i .

$$\mathbf{1}_{\Sigma_i} = \begin{cases} 1, & \text{if } \mathbf{x} \in \Sigma_i. \\ 0, & \text{otherwise.} \end{cases} \quad (2.1)$$

The evolution of the interface network is reflected by the change of the phase boundary of $\mathbf{1}_{\Sigma_i}$. The original TD scheme from Merriman, Bence and Osher in the isotropic, two-phase setting is given

as in Algorithm 1 from [MBO92].

Algorithm 1 MBO

- 1: **Initialization** Given Σ^0 and time step size δt
 - 2: **For iterate** $k + 1$
 - 3: $\psi^k = K_{\delta t} * \mathbf{1}_{\Sigma^k}$ ▷ Convolution/Diffusion step
 - 4: $\Sigma^{k+1} = \{\mathbf{x} : \psi^k(\mathbf{x}) \geq \frac{1}{2}\}$ ▷ Threshold/Sharpening step
-

The convolution kernel $K : \mathbb{R}^d \rightarrow \mathbb{R}$, can be any spherically symmetric kernel, and is usually chosen to be the Gaussian for computation purpose:

$$G_{\delta t}(\mathbf{x}) = \frac{1}{(4\pi(\delta t))^{d/2}} \exp\left(-\frac{|\mathbf{x}|^2}{4(\delta t)}\right) \quad (2.2)$$

By this choice of kernel, the MBO scheme evolves the boundary $\partial\Sigma$ by mean curvature motion [MBO92] and the phase boundary velocity is

$$v(\mathbf{x}) = \mu\sigma\kappa(\mathbf{x}) \quad (2.3)$$

where κ is the mean curvature, the boundary mobility μ and the surface energy σ are constants.

The time step size δt is a model variable that has no effect on stability, but should be considered to reach desired accuracy. In [EO15], Esedoglu and Otto introduced an extension of the two-phase MBO scheme to a general multi-phase setting, as showing in the Algorithm 2.

Algorithm 2 EO

- 1: **Initialization** Given $\Sigma_1^0, \dots, \Sigma_N^0$ and time step size δt
 - 2: **For iterate** $k + 1$
 - 3: $\psi_i^k = \sum_{\substack{j=1 \\ j \neq i}}^N K_{\delta t}^{i,j} * \mathbf{1}_{\Sigma_j^k}$ ▷ Convolution/Diffusion step
 - 4: $\Sigma_i^{k+1} = \{\mathbf{x} : \psi_i^k(\mathbf{x}) \leq \min_{j \neq i} \psi_j^k(\mathbf{x})\}$ ▷ Threshold/Sharpening step
-

The main difference between the MBO and the EO schemes is that in the EO scheme the new kernel $K_{\delta t}^{i,j}$ is designated for the boundary between Σ_i and Σ_j . The new kernel in the EO scheme

is constructed to account for non-constant σ and μ between two phases. As mentioned in Section 1.1, σ and μ play far more complex roles in grain growth than being constant. They are affected by both grain boundary normal and misorientation between neighboring grains. Incorporating the anisotropic surface energy and mobility into $K_{\delta t}^{i,j}$ yield to an anisotropic grain growth formulation with the boundary velocity being

$$v(\mathbf{x}) = \mu^{i,j}(\mathbf{n}(\mathbf{x}))\sigma^{i,j}(\mathbf{n}(\mathbf{x}))\kappa(\mathbf{x}) \quad (2.4)$$

In this work, we focus on multi-phase isotropic simulations. We use Algorithm 2 and take the same form as in Equation (2.2) for the kernel $K_{\delta t}^{i,j}$. In the grain growth simulations performed in this work, Algorithm 2 makes direct use of the observed microstructures as the input by assigning one characteristic function $\mathbf{1}_{\Sigma_i}$ to each grain Σ_i , and evolve the grain boundary network by first a convolution/diffusion step and then a threshold/sharpening step.

2.1.2 Model Validation

In this section, we want to validate the isotropic TD model is evolving the grain boundaries isotropically. According to classical grain growth theories, it is expected to observe self-similarity in grain size distribution for ideal isotropic grain growth (normal grain growth) [BT52, Atk88]. The grain size distributions of the simulated microstructures at different anneal states are plotted in Figure 1 and they have self-similar forms.

Burke and Turnbull [BT52] found a linear relation between time and the power of the average grain size (usually is 2nd, 3rd or 4th power according to different studies) using an isotropic curvature-driven model for both 2D and 3D systems. In Figure 2, the difference between the 2nd power of average grain size $\langle R \rangle^2$ and initial average grain size $\langle R_0 \rangle^2$ of a simulation are plotted as a function of iteration step. The iteration steps can be seen as normalized time steps. The linear relation is clearly shown. Grain size is calculated as $R = (\frac{3}{4\pi}V)^{1/3}$ with V being volume of the grain in

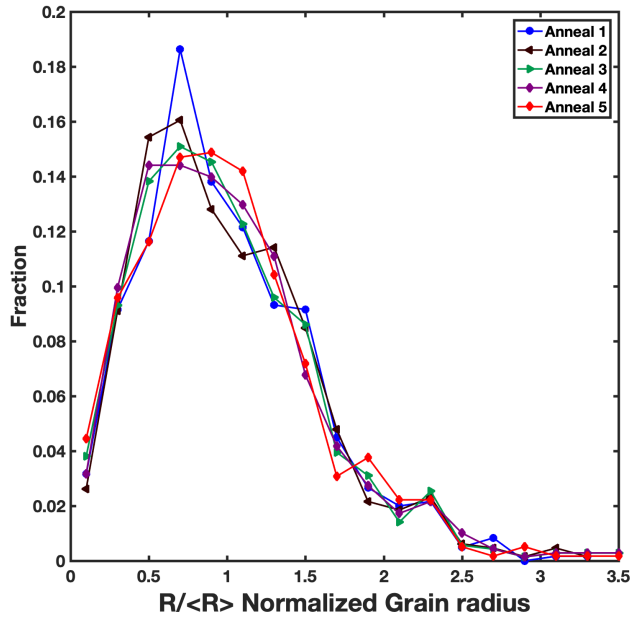


Figure 1: Grain size distributions of simulations at different annealing stages.

voxels.

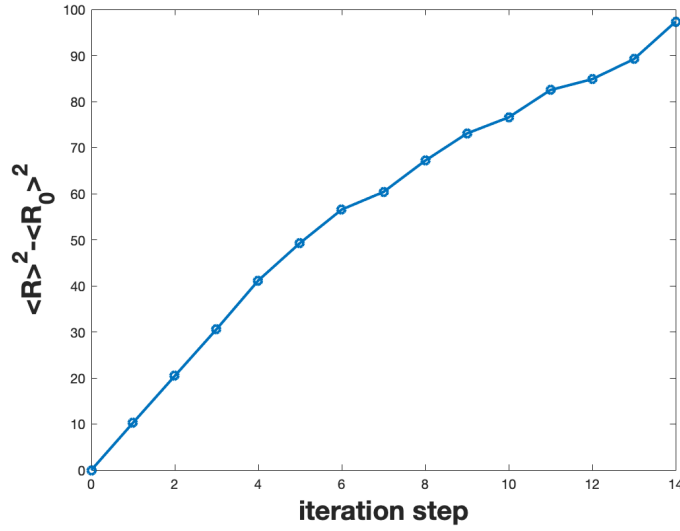


Figure 2: $\langle R \rangle^2 - \langle R_0 \rangle^2$ as a function of iteration step.

Good agreements with the classical theories are presented in this section. More discussions will be included in Section 2.2 when the simulated microstructures are compared to the experimental ones.

2.1.3 Data Processing for Comparison

To compare the simulations with the experiment data, it is important to establish the common volume between experimental anneal states and the time scale in simulations.

2.1.3.1 Establishing the common volume. The Ni sample from experiment is of cylinder shape, and the microstructure is described with an orientation map that are colored according to grain orientations. Figure 3 shows the anneal state 0 with all the twin boundaries merged. Voxels marked in red indicate they do not belong to any grain. The simulation directly uses the orientation map to create characteristic functions $\mathbf{1}_{\Sigma_i}$ as in Equation 2.1, and the phases Σ_i^0 is the input for iterations as in Algorithm 2. Thus, the computational grid of the simulation has the same size of the input microstructure, for example $369 \times 372 \times 62$ for anneal state 0.

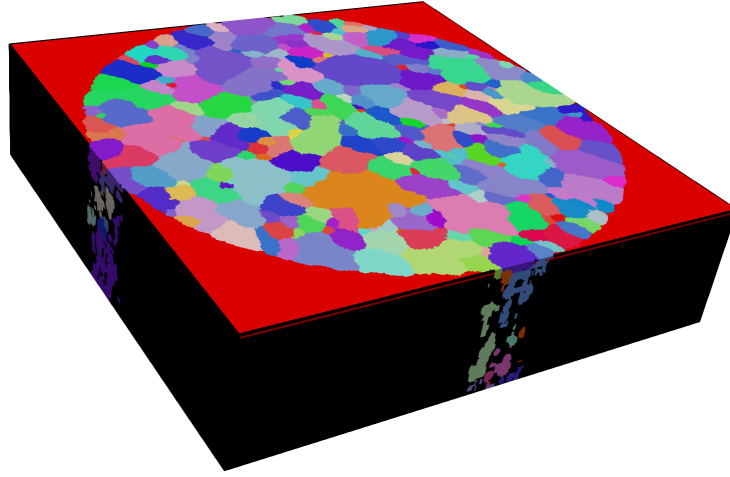


Figure 3: Twin-boundary-merged orientation map of the Ni sample at anneal state 0. The size of the map is $369 \times 372 \times 62$. Grains are colored by their orientations. Voxels marked in red do not belong to any grain.

To simulate the experimental microstructure of the cylinder shape Ni sample with 921 grains (anneal state 0), special treatments have been made to exclude the space that is inside of the computational grid but outside of the actual sample (red region in Figure 3). The easiest way to accomplish this is to manipulate the characteristic function of the red region Σ_0 . By setting $\mathbf{1}_{\Sigma_0} = 0$, if $x \in \Sigma_0$ the contribution to ψ_i ($i = 1, 2, \dots, 921$) from Σ_0 is always 0 in the convolution step in Algorithm

2, and the boundary between Σ_0 and Σ_i will not evolve during the iteration. Thus, the volume is preserved throughout the simulation.

For comparison, we apply cropping and shifting to experimental microstructures for two reasons: (1) the measurements made for the 6 anneal states of Ni sample were taken at slightly different locations; (2) the experimental microstructures have different volumes. Usually the following state has bigger volume than that of the previous state, this is to make sure even with the shift of view, most of the grains in the previous state remain in the following one. The most difference on the size measurements is on the vertical direction of the cylinder (z direction) as one state has 62 layers of voxels and the other has 88. This corresponds to a volume difference of about 3 million voxels. Anneal state 0 to 4 is cropped and shifted respectively to have the same number of layers as its following state.

2.1.3.2 Establishing the time scale. As the simulation goes on, the overall grain size keeps growing through each iteration following isotropic grain growth rules. A stopping criterion needs to be established so it can be compared with experiment. We tried three different criteria:

(1) maximum agreement between the simulation output and the targeted anneal state. It goes through every grain that is matched between the initial and targeted anneal states, and sums up the number of voxels that exist both in the grain of the simulation and the grain in targeted anneal state. Higher the sum, better the agreement.

For example, a simulation that has anneal state 0 (An0) as input and tries to match with An1, for every iteration, we calculate V_{match} , which is:

$$V_{\text{match}} = \sum_{i=1}^M n_i \quad (2.5)$$

where n_i is number of the voxels that exist in both the i -th grain in the current iteration step and the i -th grain in the targeted anneal state (An1 in this case). Note that the calculation is summed over M ($M \leq N$) grains, as not all grains between two anneal states are matched in the experiment.

The lists of the matched grains are provided by the analyses of the reconstructed microstructures, and M varies between different anneal states. After applying this criterion, we observed first a small increase (about 2%) of V_{match} and then a continuous decrease. It indicates that the simulation quickly diverged from the targeted anneal state. However, there is not enough evolution occurred (the overall grain size is still small) when V_{match} is at its maximum. The simulation stopped too early by this criterion.

(2) matching average grain boundary movement. It calculates the movement of each boundary and then its average for each iteration step. It stops when the average reaches the experimental average boundary movement. The calculation of the boundary movement is done by Dr. Aditi Bhattacharya and shown in her dissertation.

The iteration step picked by this criterion has significantly lower number of grains than the target anneal state (the overall grain size is much larger). The simulation stopped too late by this criterion.

(3) matching average grain sizes. It calculates the average grain size for each iteration step and stop when reaches the average grain size of the targeted anneal state. The iteration step picked this way has reasonable amount of evolution that is comparable to the experiment. Therefore, it is chosen to be the stopping criterion. The average grain size V_{ave} is calculated by:

$$V_{\text{ave}} = \frac{1}{N} \sum_{i=1}^N V_i \quad (2.6)$$

where V_i is volume of the i -th grain.

Even though the first two criteria are not used here, they can be good indicators when the model is extended to include anisotropy. We expect them to pick a much better iteration step for the anisotropic model.

2.2 Results

Simulations are performed for each neighboring anneal state pair, so in total of 5 simulations for the 6 anneal states. Figure 4 shows An0 experimental microstructure of 921 grains that is used as simulation input, the targeted experimental microstructure An1 of 756 grains and the simulated microstructure with 601 grains.

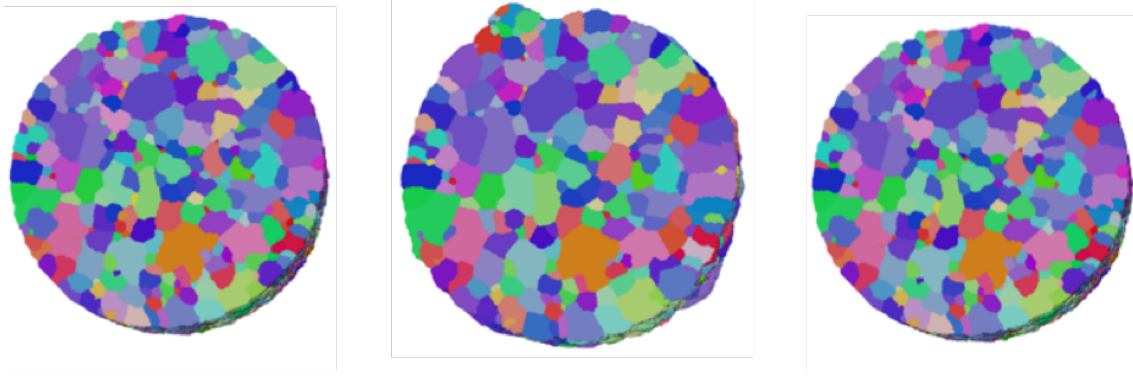


Figure 4: Left: experimentally measured microstructure of anneal state 0 of 921 grains, middle: experimentally measured microstructure of anneal state 1 of 756 grains and right: the simulated microstructure of the anneal state 1 with 601 grains.

Figure 5 shows a single bulk grain across all anneal states in experiment and simulations. This grain shrinks with annealing in the experiment as well as simulation. By comparing each column which has the target grain shape on the top and simulated grain shape on the bottom, it is fair to say that the isotropic model can not predict for individual grain. When comparing every diagonal grain pair (from top left to bottom right), which has the input grain shape and the simulated grain shape, it is clear that the simulations smooth out the grain surface (reduce boundary curvature).

In [BSH⁺19] an assumption based on isotropic grain growth is made that the difference of the number of neighbors F of a grain and the average number of neighbors of the neighboring grains $\langle F_{NN} \rangle$ (F_{NN} is the number of one neighbor's neighbors) serves as a good predictor for the sign of the grain's volume change:

$$(V_F^{2/3} - V_I^{2/3}) \propto (F - \langle F_{NN} \rangle) \quad (2.7)$$

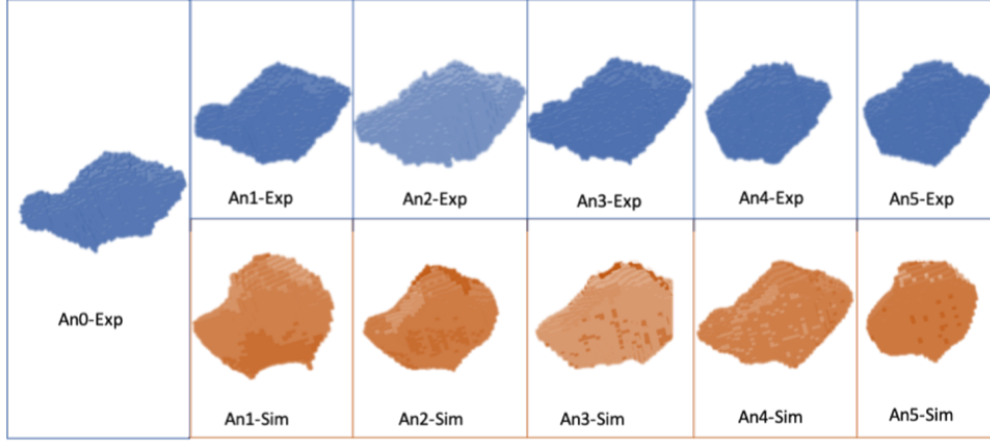


Figure 5: Visualization of a bulk grain across all anneal states in experiment and simulations. The top row shows experiment grains starting from An 0 to An 5 and the bottom row shows the simulated grains from An 1 to An 5.

When a grain is large, thus having more neighbors than its neighbors, it is more likely to grow and vice versa. In Figure 6, the two thirds of the change of volume between the final and initial states $V_F^{2/3} - V_I^{2/3}$ versus $F - \langle F_{NN} \rangle$ is plotted for all grains in both experiment and simulation. Simulation shows a more obvious linear relation that cross x -axis at 0, meaning positive $F - \langle F_{NN} \rangle$ results in an increase of volume.

Figure 7 shows the grain size distribution and grain volume distributions of the experimental and simulated microstructures for all the anneal states. The experiment and simulation distributions are similar with some differences at the small grain size region. The distribution shows simulated microstructure has a significantly higher fraction (0.15%) of smaller grains ($<5\mu\text{m}$) than in experiment (0.01%). In other words, simulation is shrinking more grains than what actually shrunk. This is expected, as in isotropic simulation, small grains have much larger curvature therefore disappear fast according to Equation 2.3. However, the experiment is not isotropic, and small grains are not necessarily disappearing (even growing according to Figure 9).

Figure 8 shows the distribution of volume fraction change between the initial and the final states for experimental and simulated grains. For experiment, this would be $\frac{V_f - V_i}{V_i}$ where V_i is the grain volume at the initial anneal state and V_f is at the following state; for simulation, this would be $\frac{V_s - V_i}{V_i}$

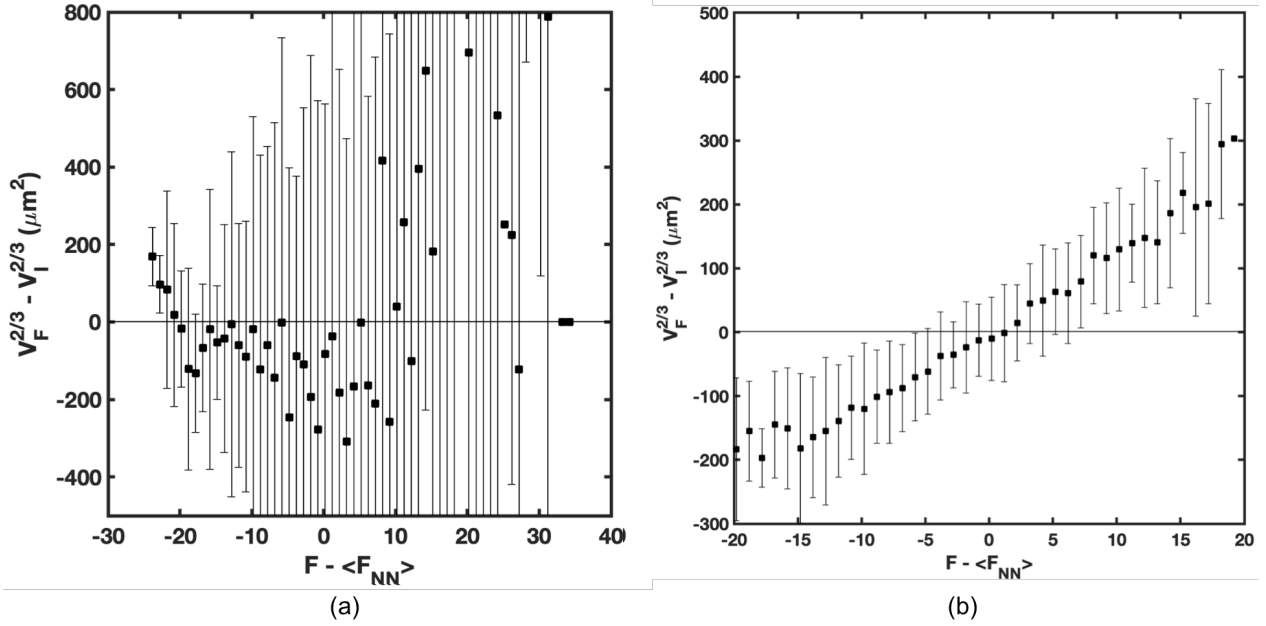


Figure 6: Change in volume versus the difference between the number of neighbors and the average number of neighbors of the neighbors in (a) experiment and (b) simulation. For each class of $F - \langle F_{NN} \rangle$, the marker is the mean value and the bar shows one standard deviation of the distribution.

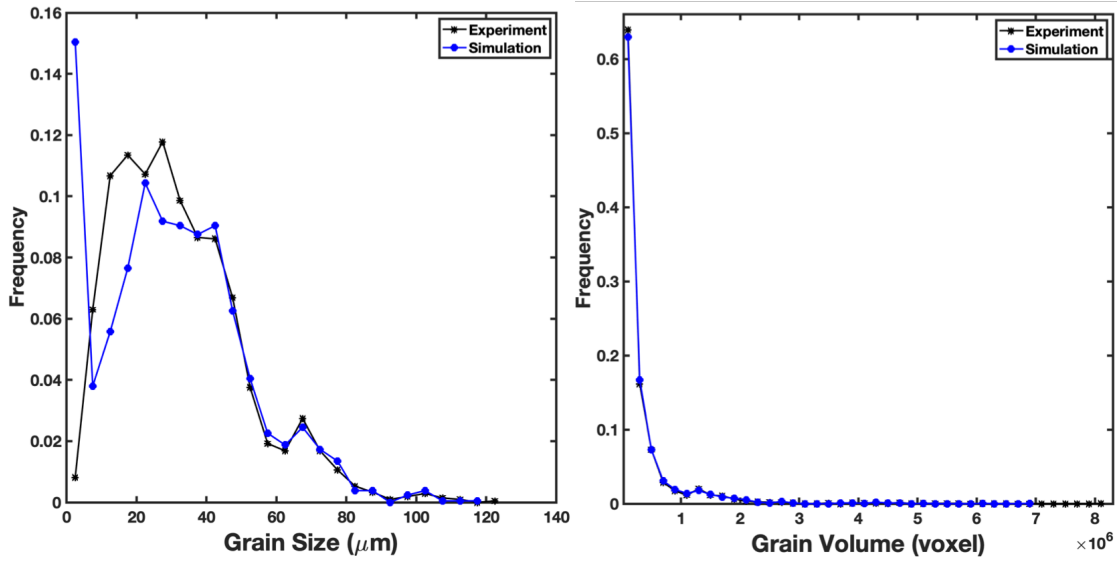


Figure 7: The grain size distribution and grain volume distribution of experimental and simulation microstructures for all the anneal states.

where V_s is the grain volume at the iteration step picked by the stopping criterion in Section 2.1.3.2. While both the experiment and simulation plots have the maximum number of grains around zero volume fraction change (simulation is slightly more than experiment), a higher number of simulated

grains (about 17%) shrunk to zero (these grains completely disappeared) than they actually did in experiment (about 10%). Also the higher end of the plots indicate that experiment has more grains growing, and they could grow as much as almost doubling the size (85%), which is much more than simulation (maximum of 55% increase). This is expected, as in isotropic simulation, large grains have much smaller curvature therefore grows slower.

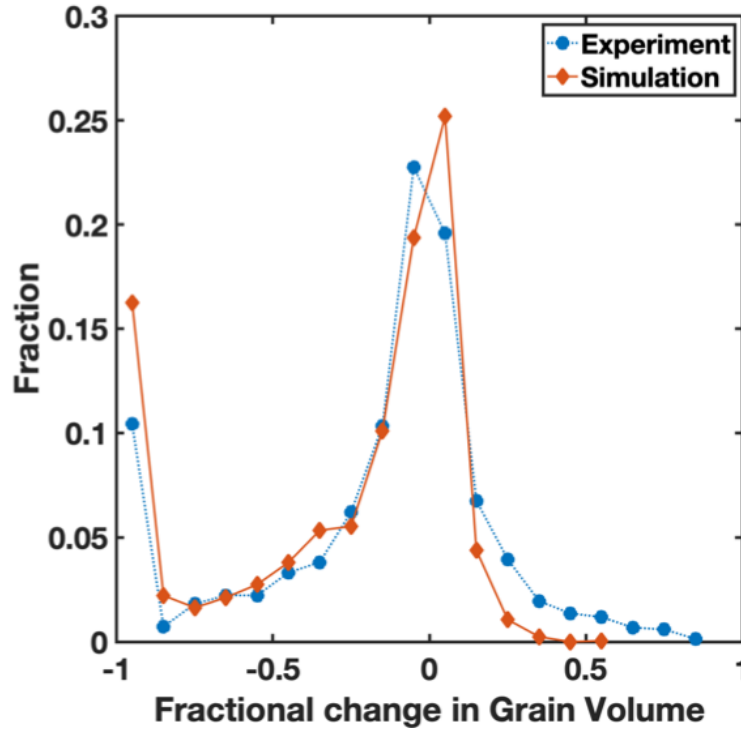


Figure 8: The distribution of fractional change in volume for experimental and simulated grains.

To understand Figure 8 better, we plot the fractional change in grain volume vs grain size in Figure 9. The simulation follows the isotropic grain growth such that smaller grains shrink and larger grains grow, as shown in 9, while in experiment such relation is less apparent with data points spreading out more evenly above and below the 0 volume fraction change. It also shows that in both experiment and simulation, as the grain size gets larger, the magnitude of fractional change is smaller. The data points in experiment having large fractional volume increase are usually the smaller grains. This suggests that the mismatch at the high end of the distribution in Figure 8 is mainly caused by wrong volume predictions of these small grains. Noticed that the grains disappear in simulation are clustering in the small grain size region, whereas in experiment the grains of this

region exhibit significant growth. It is sufficient to say that the simulation is hard to capture this phenomenon and therefore most errors would result from small grains.

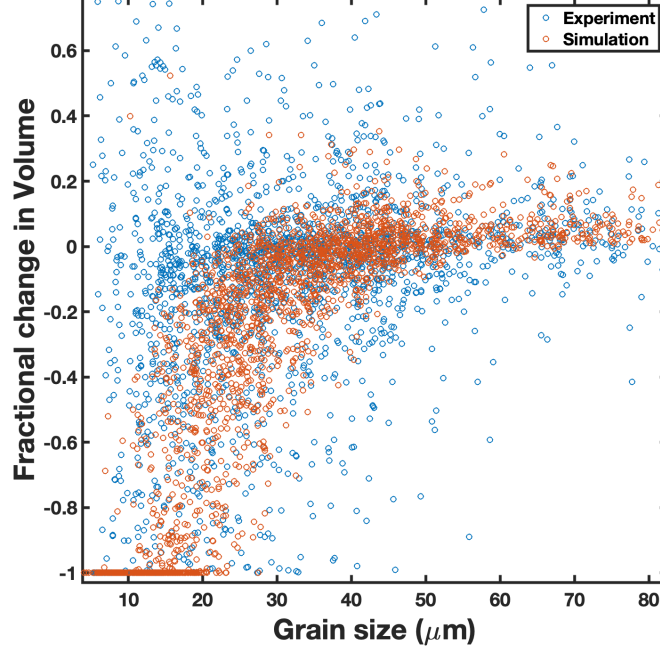


Figure 9: The fractional change in volume vs grain size in experimental and simulated grains.

Figure 10 plots the triangle curvature distributions (grain boundaries are segmented into triangles after meshing and smoothing with Dream.3D, details can be found in Dr. Aditi Bhattacharya's dissertation.) of all boundaries in the simulation and experiment. Experiment curvatures have a higher fraction at the higher end and simulation curvatures have a higher fraction at the lower end, meaning the simulation decreases boundary curvatures. This behavior agrees with the isotropic TD formulation that high curvature boundaries, mostly from smaller grains, move faster and make the small grains disappear faster, so the grain boundary network evolve to a lower curvature state.

Since most mismatches are associated with smaller grains (are size-dependent), we plot the volume prediction error VPE as a function of the topological error TE (topology as in number of faces of

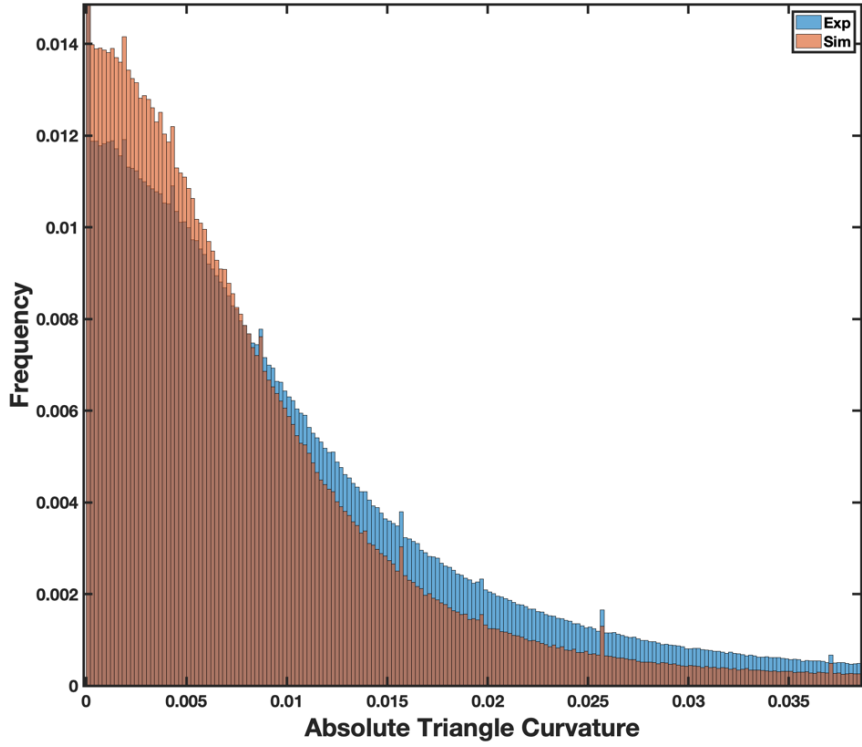


Figure 10: The triangle curvatures for all boundaries in the simulation and experiment.

a grain) in Figure 11. These values are calculated as follows:

$$\Delta N_s = N_{\text{sim}} - N_{\text{exp(initial)}} \quad (2.8)$$

$$\Delta N_e = N_{\text{exp(final)}} - N_{\text{exp(initial)}} \quad (2.9)$$

$$TE = \Delta N_s - \Delta N_e = N_{\text{sim}} - N_{\text{exp(final)}} \quad (2.10)$$

$$VPE = \frac{V_s - V_e}{V_e} \quad (2.11)$$

$$(2.12)$$

where VPE is the relative difference between the volume predicted by simulation V_s and volume at experimental final state V_e . And TE , topological error, is the difference between the number of neighbors predicted by simulation N_{sim} and the number of neighbors at experimental final state $N_{\text{exp(final)}}$. A low VPE indicates small difference between the volume predicted and actual final

volume of the grain. A low TE value means the error of predicting topological evolution of the grains is small. This plot is linear and monotonically increasing, indicating a strong correlation between the wrong prediction of grain topology change and wrong prediction of grain volume change.

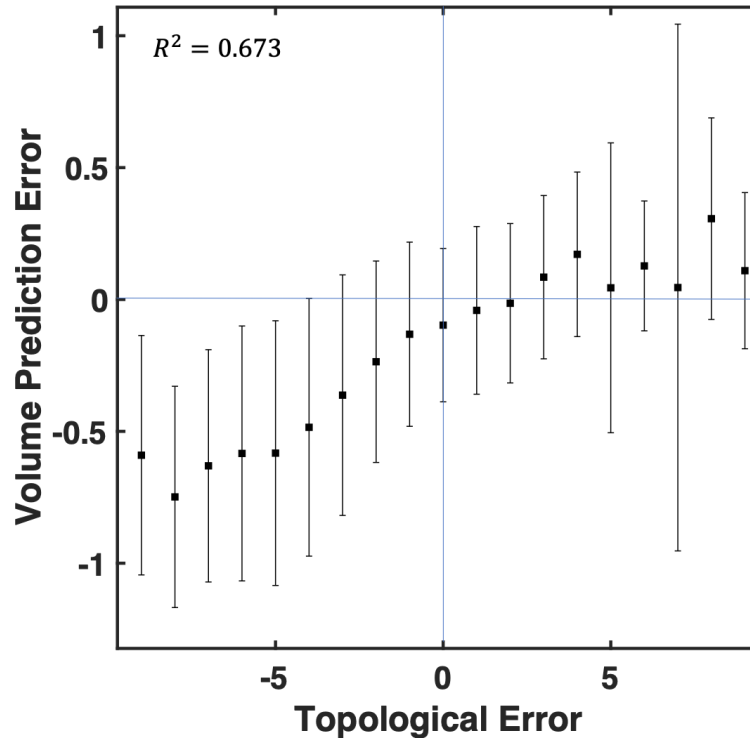


Figure 11: The volume prediction error as a function of topological error.

2.3 Conclusions

Isotropic TD model is applied to simulate 3D grain growth on reconstructed microstructures of a Ni sample during annealing. The model is first validated by checking with classical isotropic grain growth theories. Then simulations of every neighboring anneal state pair are performed. Statistical analysis results of the simulated and experimental microstructures match to each other in general with some differences mostly associated with small grains. Simulations following the isotropic grain growth theories shrink the small grains and grow the larger ones, while small grains in experiment can grow as much as 85% of its original size and large grains can shrink as much as 40%. The wrong prediction of topology change of individual grains further affects the volume prediction in simulations. This motivated the use of anisotropic model briefly mentioned in Section 2.1.1.

The isotropic TD scheme can be extended to include anisotropic surface energy and mobility data from experiment [[EJZ17](#)]. By comparisons between simulations with the isotropic TD scheme and anisotropic TD scheme, different forms of anisotropic kernel can be tested and give insights about how the boundary properties affect grain boundary evolution.

3 Modeling of Dislocation Dynamics in Metals

This is joint work with Dr. Abigail Hunter, Dr. Nithin Mathew, Dr. Ricardo Lebensohn at Los Alamos National Laboratory, Prof. Enrique Martinez at Clemson University and Prof. Irene J. Beyerlein at University of California, Santa Barbara. Two topics are covered in this work. **PFDD is extended to BCC metals in Section 1.2.1 and Section 3.1, this part has been published in [PMB⁺20a].** PFDD is adapted to use non-orthogonal grids in Section 1.2.2 and Section 3.2, this part is under preparation for publishing.

3.1 A 3D Phase Field Dislocation Dynamics Model for Body-centered Cubic Crystals

In this section, the PFDD formulation that has been traditionally used for perfect dislocations in FCC metals is first reviewed [BH16a]. Since BCC metals typically do not mediate plasticity through partial dislocation motion, the formulation for perfect dislocations is extended to account for differences in edge/screw dislocation motion that is common to BCC metals. This extension incorporates a character dependence into the energy functional minimized in the PFDD formulation.

3.1.1 Phase Field Dislocation Dynamics (PFDD)

As briefly described in the previous section, in the PFDD formulation, dislocations are described using scalar-valued order parameters $\zeta^\alpha(\mathbf{x}, t)$ defined on each active slip system α . For example, in an FCC material there can be up to 12 active order parameters, one parameter per slip system. Integer values of these order parameters represent perfect Burgers vector translations (or no translation at all with a zero value order parameter), where atomic bonds have already been broken and reformed and the crystal has undergone slip. A positive perfect dislocation on system corresponds to a positive integer jump in the order parameters and vice versa for a negatively signed dislocation. Order parameters with values between zero to one indicate the location of the dislocation

core, where the atoms in the crystal structure are broken and not perfectly aligned. The total system energy E , can be expressed as a function of these order parameters. To capture the motion of the dislocation network, the system is expected to evolve toward a minimum energy state. Minimization of the total energy is done using a time-dependent Ginzburg-Landau (TDGL) kinetic equation, which also allows for stress equilibrium, $\text{div } \boldsymbol{\sigma} = \mathbf{0}$, to be achieved:

$$\frac{\partial \zeta^\alpha(\mathbf{x}, t)}{\partial t} = -L \frac{\partial E(\zeta)}{\partial \zeta^\alpha(\mathbf{x}, t)} \quad (3.1)$$

with the assumption that the total strain $\boldsymbol{\epsilon}(\mathbf{x}, t) = \boldsymbol{\epsilon}^e(\mathbf{x}, t) + \boldsymbol{\epsilon}^p(\mathbf{x}, t)$, where $\boldsymbol{\epsilon}^e$ is the elastic strain, and $\boldsymbol{\epsilon}^p$ is the plastic strain. The coefficient L governs the rate at which equilibrium is achieved.

We assume that plasticity is mediated by the motion and interaction of dislocations, and hence the plastic strain, $\boldsymbol{\epsilon}^p$, is directly dependent on the active order parameters in a system [KCO02, WJCK01], following

$$\epsilon_{ij}^p(\mathbf{x}, t) = \frac{1}{2} \sum_{\alpha=1}^N b \zeta^\alpha(\mathbf{x}, t) \delta_\alpha (s_i^\alpha m_j^\alpha + s_j^\alpha m_i^\alpha), \quad (3.2)$$

where N is the number of active slip systems, b is the magnitude of the Burgers vector \mathbf{b} , \mathbf{s}^α is the slip direction (normalized Burgers vector $\mathbf{s} \equiv \frac{\mathbf{b}}{b}$), \mathbf{m}^α is the slip plane normal α , and δ_α is a Dirac distribution supported on the slip plane of slip system α .

The total system energy consists of two key energy terms [KCO02]:

$$E = E^{strain} + E^{lattice}. \quad (3.3)$$

The first term, E^{strain} , is the strain energy, which accounts for elastic interactions between dislocations (e.g., attraction and repulsion), and interactions between the applied stress and the dislocations. It can be written as the sum of internal and external interaction terms:

$$E^{strain} = E^{int} + E^{ext} = \frac{1}{2} \int C_{ijkl} \epsilon_{ij}^e(\mathbf{x}, t) \epsilon_{kl}^e(\mathbf{x}, t) d^3x - \int \sigma_{ij}^{appl} \epsilon_{ij}^p d^3x, \quad (3.4)$$

where \mathbf{C} is the elasticity tensor, and $\boldsymbol{\sigma}^{appl}$ is the applied stress. ϵ^e can be solved in terms of ϵ^p through transformation into Fourier space, which provides the following expression of the internal strain energy [KCO02]:

$$E^{int}(\zeta) = \frac{1}{2} \oint \hat{A}_{mnuv}(\mathbf{k}) \hat{\epsilon}_{mn}^p(\mathbf{k}) \hat{\epsilon}_{uv}^{p*}(\mathbf{k}) \frac{d^3k}{(2\pi)^3} \quad (3.5)$$

where $\hat{A}_{mnuv}(\mathbf{k}) = C_{mnuv} - C_{kluv} C_{ijmn} \hat{G}_{ki}(\mathbf{k}) k_j k_l$, $(\hat{\cdot})$ denotes the Fourier transform, and $(*)$ denotes the complex conjugate, \mathbf{k} is the wave vector, $\hat{\mathbf{G}}$ is the Fourier transform of the Green's tensor of linear elasticity [Mur87], and the \oint denotes the Cauchy principal value of the integral.

The second term in Equation (3.3), $E^{lattice}$, accounts for the energy expended on breaking and reforming atomic bonds as dislocations move through the crystal lattice. Due to the periodicity of the crystal lattice, for perfect dislocations, $E^{lattice}$ is modeled with as a sinusoidal function [WJCK01, BH16a]:

$$E^{lattice}(\zeta) = \sum_{\alpha=1}^N \int B \sin^2(n\pi \zeta^\alpha(\mathbf{x}, t)) \delta_\alpha d^3x \quad (3.6)$$

where B is the Peierls barrier, or the magnitude of the energy barrier to activate slip. This parameter can be informed many ways. For a wide range of BCC metals the Peierls potential for screw dislocations have been calculated using DFT [WTF13, LBW18]. It can also be calculated more quickly via MD simulations but with the caveat that accuracy depends on the reliability of the interatomic potential used [LeS13, LBW18, ZBGW11]. More often, this term is informed using information from the material γ -surface, such as specific stacking fault energies or generalized stacking fault energy (GSFE) curves as calculated with atomistic methods [Sch05, Vit68]. Such energetic calculations do not involve the motion of a dislocation but rather shifts of two crystal

halves with respect to one another across a crystallographic plane, and therefore do not correspond directly to the Peierls potential. A relationship has been determined between the Peierls potential and the energy of the atomic bonds across a plane as a function of shifts in the atomic positions [JD97, Pei40, Sch05]. In BCC metals, the peak value of this energy function in the unstable stacking fault energy (γ_U), which can therefore be related to motion of the entire dislocation.

3.1.2 Extension to BCC Metals

It has been shown that in BCC metals the Peierls stress for screw dislocations is one to two orders of magnitude greater than that for edge dislocations [LK79, Vit74]. Consequently edge dislocations move faster through the crystal lattice than screw-type dislocations which, in turn, dominate the plastic response [HB01, HL68, KBC12]. To better model the plastic deformation in BCC metals, we extend the PFDD model to account for differences between edge and screw dislocation motion.

Specifically these extensions primarily modify $E^{lattice}$, so that character dependence of the Peierls energy barrier can be accounted for. As mentioned above, the Peierls barrier itself can be estimated with atomistic modeling approaches. However, to determine the Peierls potential for the all (or even many) dislocation characters is computationally costly. In an effort to approximate the variation of the Peierls potential and also move up in length-scale, we utilize γ_U in conjunction with a transition function. The transition function captures the dependence of the Peierls energy barrier on screw/edge character of a dislocation. Furthermore, this function describes how the energy barrier varies with character in general, and by incorporating such a term into $E^{lattice}$ dependence on dislocation line character is added into the PFDD model. Determining the line character of a general dislocation line requires calculation of the gradient of the order parameter. This is followed by, the development of the transition function which is a function of the character angle, θ .

3.1.2.1 Calculating the Dislocation Line Sense. Figure 12 presents a schematic of a general dislocation loop, with a local coordinate system comprised of orthogonal vectors: one is normal to

the glide plane (also the slip plane normal \mathbf{m} as defined in the global coordinate system), another is normal to the dislocation line \mathbf{n} , and a third that is the local tangent to the dislocation line \mathbf{t} . Within this system, the Burgers vector could be any vector within the \mathbf{t} - \mathbf{n} plane. The tangent vector \mathbf{t} defines the line sense of the dislocation segment at that point along the loop. The angle between this vector and the Burgers vector will define the character of that segment of dislocation, with an angle of 90° indicating dislocations of pure edge type, and an angle of 0° representing segments of pure screw type.

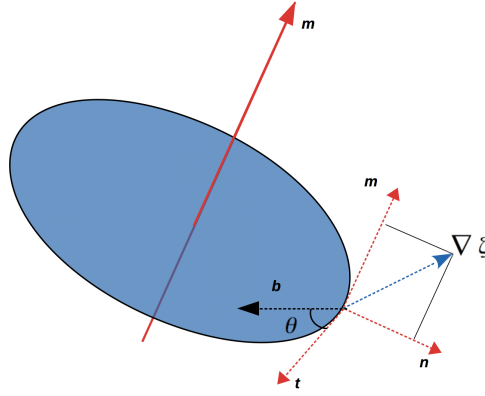


Figure 12: A dislocation loop (black curve surrounding the slipped region (denoted in blue)) with a Burgers vector \mathbf{b} . The gradient of the order parameter $\nabla\zeta^\alpha$ lies in the plane formed by dislocation line normal \mathbf{n} and slip plane normal \mathbf{m} .

Within the PFDD model, such a loop would be modeled with a single active order parameter with a value of unity inside the loop and a value of zero outside the loop. Hence, the gradient of the order parameter, $\nabla\zeta^\alpha$, will only be non-zero at points along the dislocation line, where the order parameter transitions between 0 and 1. In addition, the gradient of the order parameter lies in the \mathbf{n} - \mathbf{m} plane, as shown in Figure 12, and defines the direction in which the order parameter has the most dramatic change.

In order to add character dependence to the total system energy the character angle, θ , is needed for all points along all dislocation lines present in the simulation. To achieve this we first calculate the gradient of all active order parameters across all computational points within a simulation using a central difference approach,

$$\nabla \zeta^\alpha(\mathbf{x}, t) = \left(\frac{\zeta^\alpha(x_{i+1}, t) - \zeta^\alpha(x_{i-1}, t)}{2\Delta x}, \frac{\zeta^\alpha(y_{j+1}, t) - \zeta^\alpha(y_{j-1}, t)}{2\Delta y}, \frac{\zeta^\alpha(z_{k+1}, t) - \zeta^\alpha(z_{k-1}, t)}{2\Delta z} \right) \quad (3.7)$$

where (x_i, y_j, z_k) is any computational grid point, and $(\Delta x, \Delta y, \Delta z)$ are the grid spacings in the (x, y, z) directions, respectively. Taking the cross product of this gradient vector with the slip plane normal produces the vector tangent to the dislocation line, i.e., the line sense. This unit tangent vector can be expressed as:

$$\mathbf{t}^\alpha(\mathbf{x}, t) = \frac{\nabla \zeta^\alpha(\mathbf{x}, t) \times \mathbf{m}^\alpha}{|\nabla \zeta^\alpha(\mathbf{x}, t) \times \mathbf{m}^\alpha|}. \quad (3.8)$$

Finally, the character angle, θ^α , can be calculated by taking a dot product of the tangent vector and the slip direction (i.e., the normalized Burger vector):

$$\theta^\alpha(\mathbf{x}, t) = \mathbf{t}^\alpha(\mathbf{x}, t) \cdot \mathbf{s}^\alpha. \quad (3.9)$$

Recall, $\theta^\alpha = 90^\circ$ represents a point on the dislocation loop that is of pure edge type, and $\theta^\alpha = 0^\circ$ indicates pure screw type. Other values between 0° and 90° represent dislocation segments that are of mixed character.

3.1.2.2 Defining the Transition between Edge and Screw Type. To account for the anisotropy in the Peierls barrier within the PFDD model, Equation 3.6 will be dependent on the line-character such that dislocations that are of screw type must overcome a much larger energy barrier than dislocation of edge type. However, the transition of the height of the energy barrier from screw character (maximum) to edge character (minimum) must also be defined in order to allow simulations of general dislocation segments and configurations. The functional form of such a transition is generally unknown, and the formulation presented here allows for different functions to be tried and tested

against atomistic simulations and/or experimental results.

Perhaps the simplest and easiest definitions of the transition function, $\beta(\theta(\mathbf{x}, t))$, are either a simple linear or a sinusoidal transition. Both of these proposed functional shapes failed to yield matching results to atomistic results (discussed in later sections). Previous work by Kang *et al.* [KBC12] included a large number of MD simulations that determined the Peierls stresses of $\mathbf{b} = \frac{1}{2} [111]$ dislocations on the $(1\bar{1}0)$ slip plane of BCC Ta as a function of dislocation character. As expected, pure screw dislocations required the largest stress to initiate motion. Interestingly, they also found an asymmetric, local maximum in the Peierls stress for a mixed type dislocation with a character angle of $\theta = 70.5^\circ$. Based on this previous study, we chose to incorporate this second peak (preserving the asymmetry) into the transition function producing a local maximum in the energy barrier for this mixed type dislocation in addition to the global maximum for screw type dislocations.

The two-peak transition function was initially determined through interpolating the mobility data from Kang *et al.* [KBC12]. This function is expressed as:

$$\beta(\theta) = \begin{cases} 1.1603\theta^2 - 2.0431\theta + 1 & \theta \leq 0.39\pi \\ 0.5473\theta^2 - 2.0035\theta + 1.8923 & 0.39\pi < \theta \leq \pi \end{cases} \quad (3.10)$$

Using this transition function, Equation 3.6 can be rewritten for BCC materials as:

$$E^{lattice}(\zeta) = \sum_{\alpha=1}^N \int B_o \beta(\theta^\alpha(\mathbf{x}, t)) (\sin n\pi \zeta^\alpha(\mathbf{x}, t))^2 \delta_\alpha d^3x, \quad (3.11)$$

and is now dependent on the character angle, θ . The parameter B_o is analogous to B originally in Equation 3.6 in that it parameterizes the magnitude of the energy barrier. In this case, however, it is different because it will define the magnitude of the energy barrier for only pure screw type dislocations, where the previous parameter B defined the magnitude of the energy barrier for all dislocation character types. For results presented in later section, $B_o = \gamma_U$, where γ_U is determined using MS simulations (described next in Section 3.1.3). Unstable stacking fault energies for Ta

and Nb are calculated to be 950.21 mJ/m^2 and 720.89 mJ/m^2 , respectively. The transition of the magnitude of the energy barrier, $B_o\beta(\theta)$, for Ta and Nb are shown in Figure 13.

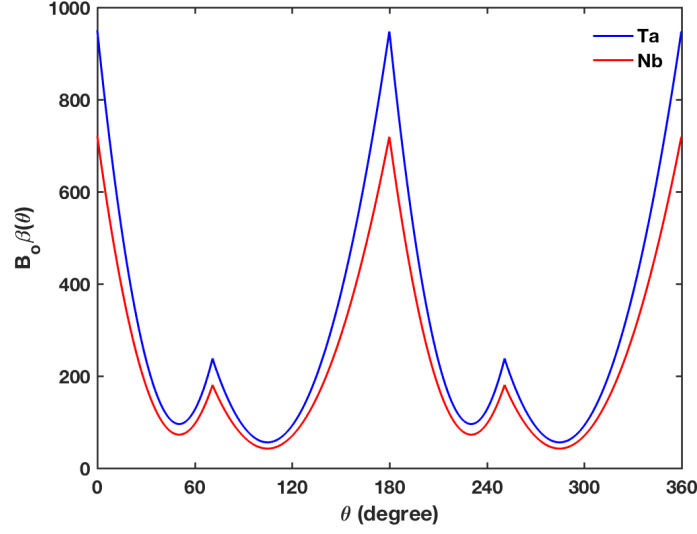


Figure 13: Energy barrier $B_o\beta(\theta)$ as a function of line character angle θ for Ta and Nb.

On implementation of this new formulation for $E^{lattice}$ into the TDGL Equation (Equation 3.1), we note that an approximation must be made. The variation of the lattice energy with respect to the order parameter becomes challenging due to the functional dependence of the transition function on the gradient of the order parameter. Furthermore, $\beta(\theta)$ is a piecewise function making the variation $\partial E^{lattice}/\partial\zeta$ analytically intractable. Hence, in calculation of the variation we have made the following approximation, $\partial E^{lattice}/\partial\zeta = \beta(\theta) (\partial E_{\star}^{lattice}/\partial\zeta)$, where $E_{\star}^{lattice}$ is the lattice energy as defined by Equation 3.6 with $B = B_o$.

3.1.3 Molecular Statics Simulations

All Molecular Statics simulations were conducted by Dr. Nithin Mathew at Los Alamos National Laboratory.

As mentioned in the previous section, the PFDD model was calibrated for Nb and Ta using MS calculations of material parameters such as γ_U and the lattice parameter. In addition, MS predictions of isotropic Voigt moduli calculated from (C) were also used to inform the PFDD model.

All MS simulations were performed using the LAMMPS [Pliov] software. The components of C were calculated using separate MS simulations in which a 3D periodic 5x5x5 simulation cell, with the Cartesian axes x, y, z oriented along the $[100]$, $[010]$, and $[001]$ crystallographic directions, at equilibrium geometry corresponding to $P = 0$ atm and $T = 0$ K. This simulation cell was affinely deformed using a prescribed set of lattice strains. These deformed geometries were used to construct energy-strain curves with respect to the applied strain, from which the C_{ijkl} were obtained. The γ_U were calculated from the γ -surfaces calculated using the standard procedure, [Vit68, DV98] in which, relaxation of atoms are allowed only in the m direction and periodic boundary conditions are used only in the glide plane. The predicted lattice parameters, linear elastic coefficients, and γ_U are provided in Table 1.

Table 1: Material parameters calculated from MS simulations and corresponding Young’s modulus E , shear modulus G , and Poisson’s ratio ν calculated with the Voigt isotropic approximation. All elastic coefficients are specified in units of GPa.

Material	Lattice parameter (Å)	C_{11}	C_{12}	C_{44}	E	G	ν	γ_U (mJ/m ²)
Nb	3.3008	246.58	133.31	28.23	110.27	39.59	0.39	720.89
Ta	3.3040	266.05	160.62	82.65	189.24	70.67	0.34	950.21

The $\langle 111 \rangle$ trace of the γ -surfaces predicted by MS simulations for Ta and Nb are shown in Figure 14. We used the Finnis-Sinclair inter-atomic potential for Nb and Ta [AT06] to ensure consistency of our simulations with the input parameterization provided to our model by Kang *et al.* [KBC12]. We note here that a shallow minimum was predicted at $0.5 * \langle 111 \rangle$ in the γ -surface for Nb for the Finnis-Sinclair potential. In addition, cross-slip of screw components during loop expansion was predicted with EAM-type potentials for Ta (Ta1 potential in [RGG⁺13]) but not with the Finnis-Sinclair potential that was used in the current study.

The PFDD model will be applied to first simulate the expansion of a single dislocation loop (discussed in more detail in the next section). To validate the PFDD results, MS simulations were carried out for similar cases. Initial simulation cells of size $108 \times 39 \times 67$ (in units of lattice parameter in the specific crystallographic orientation) were created using equilibrium lattice parameter

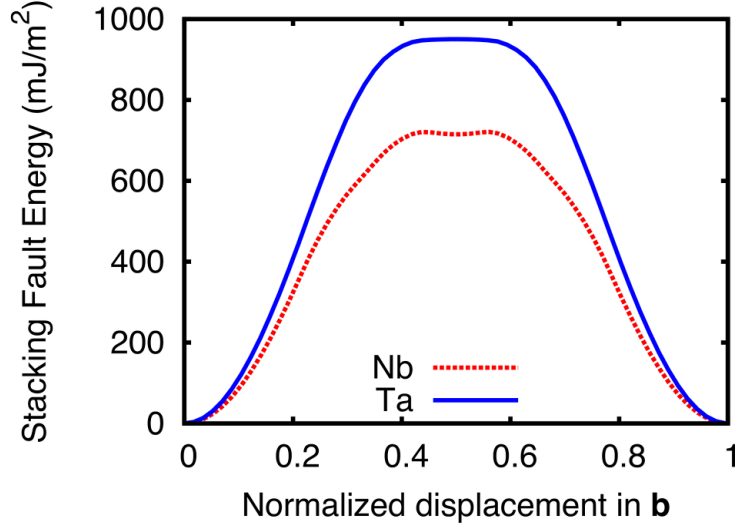


Figure 14: $\langle 111 \rangle$ trace of the γ -surfaces predicted by MS simulations for Ta and Nb. Note the shallow minima in Nb.

corresponding to $P = 0$ atm and $T = 0$ K, with the Cartesian axes x, y, z oriented along the $\langle 111 \rangle$, $\langle 112 \rangle$, and $\langle 110 \rangle$ crystallographic directions and 3D periodic boundary conditions. Following this a dislocation loop of radius $18 \cdot |b|$ was inserted on a $\langle 110 \rangle$ plane close to the center of the simulation cell using the isotropic linear elasticity displacement field of a dislocation loop, as implemented in the ATOMSK software [Hir15]. A RSS was applied to expand the loop on the slip plane in the b direction. The RSS was applied by applying an affine deformation to all the atoms in the simulation cell to result in the strain corresponding to the RSS predicted by a linear elasticity model. Extraction and visualization of the dislocation loops were done using OVITO [Stu09, SBA12, Stu14].

3.1.4 Results and Discussion

To test the extension of the PFDD model described above, we consider two different simulation configurations. The first is expansion of a single, initially circular, dislocation loop and the second is propagation of a kink-pair. The first case is informative because in BCC metals the dislocation loop will not expand symmetrically due to the difference in the energy barrier for the screw, edge, and mixed typed dislocations. A dislocation loop contains the full range of line characters, hence the role played by the character-dependent core energy on dislocation motion can be assessed.

An example of the initial conditions for the expansion of a loop in PFDD is shown in Figure 15. The 3D configuration is shown schematically in Figure 15(a). This consists of a cubic box with dimensions $108 \times 108 \times 108$ (in units of $|b|$) and an applied stress, σ_{xz} , that will cause the loop to expand. Figure 15(b) shows a close-up of the loop on the glide plane as generated from PFDD. A circular dislocation loop with radius $18*|b|$ is initialized on the $(1\bar{1}0)$ slip plane with $b = \frac{1}{2}[111]$. This loop size was chosen to match the loop radius used in the MS simulations. The green region in Figure 15(b) indicates areas that have not been slipped, whereas the blue region are areas that have been slipped by a single perfect dislocation. The red line represents the dislocation line.

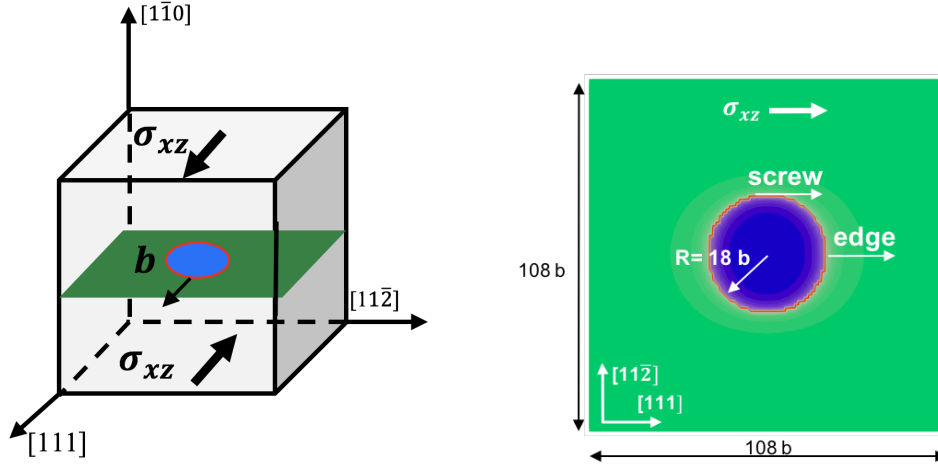


Figure 15: Figure (a) presents a schematic of the 3D simulation cell for the PFDD simulations of expansion of a single dislocation loop. Figure (b) presents the initial conditions on the glide plane for these simulations.

The second simulation configuration is for kink-pair propagation. Kink-pairs are a common mechanism for screw dislocation motion in which the screw dislocation nucleates a small step in the dislocation line. This step is comprised of two oppositely signed edge segments and one screw segment. Due to the ease at which edge dislocations move, the two edge segments will move away from each other (with appropriate loading conditions) along the length of the straight screw dislocation. This, in turn, propagates the screw dislocation. Figure 16 presents the PFDD simulation set-up for the kink-pair simulation. In this work, we do not explicitly address kink-pair nucleation. Hence, the kink-pair is placed along the straight screw dislocation as part of the initial conditions, and allowed to propagate under an applied load.

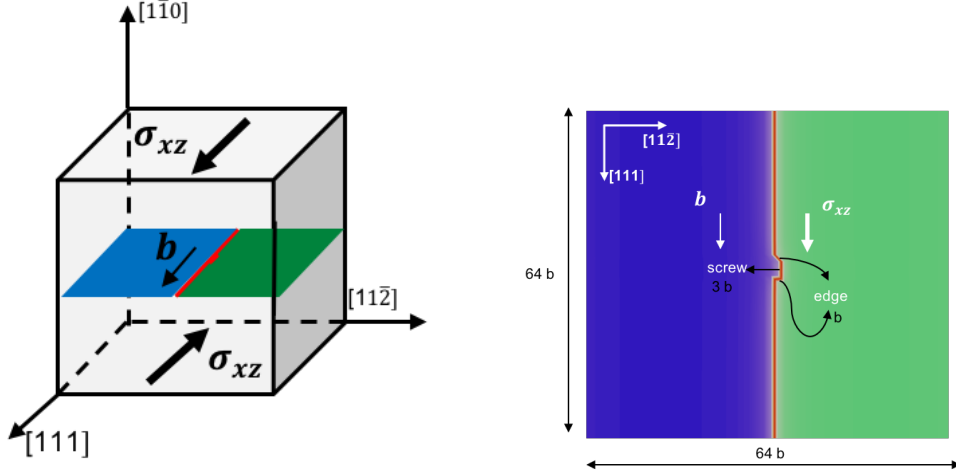


Figure 16: Figure (a) presents a schematic of the 3D simulation cell for the PFDD simulations propagation of a kink pair. Figure (b) presents the initial conditions on the glide plane for this simulation.

All simulations had a computational grid spacing of $1*|b|$ in the x , y , and z directions. In addition, due to the use of a Fourier transform in the calculation of Equation 3.5, all PFDD simulations have periodic boundary conditions. This will result in the presence of some image forces due to dislocations in neighboring periodic cells, which is also the case in the MS simulations. In both methods, the interactions with image dislocations will have an affect on the simulation, particularly when dislocation line are near the edges of the simulation cell. Finally, in these PFDD simulations the materials are assumed to be elastically isotropic. The Voigt isotropic moduli are reported in Table 1.

3.1.4.1 Expansion of a Perfect Dislocation Loop. To test our character-dependent lattice energy, we first simulated the expansion of a perfect dislocation loop in both PFDD and MS for Ta and also Nb. Ta provides the most direct comparison between modeling approaches since the functional form of the transition function is formulated using MD information generated for Ta. In addition, these MD results utilized the same interatomic potential as the MS results presented here. However, the model should be general enough to extend to other BCC metals. Hence, we have also modeled Nb using the same piecewise function for the transition function. This is somewhat of an

extrapolation, since Peierls stress or Peierls energy barrier calculations as a function character have not been previously done for Nb.

Figures 17 and 18 show the expanding dislocation loop at different stages of the minimization for an applied RSS. A RSS value of 2 GPa was used for the Ta and Nb in both the PFDD and MS simulations. This value was selected to be smaller than the Peierls stress for the screw dislocation, but large enough to overcome the elastic attraction between the dislocation segments within the loop. The loops are colored by character, with a continuous red-white-blue coloring scheme transitioning from screw (red) to edge (blue) character. For all quantitative comparisons, screw dislocations were defined as $\theta = 0^\circ \pm 10^\circ$ and edge as $\theta = 90^\circ \pm 10^\circ$.

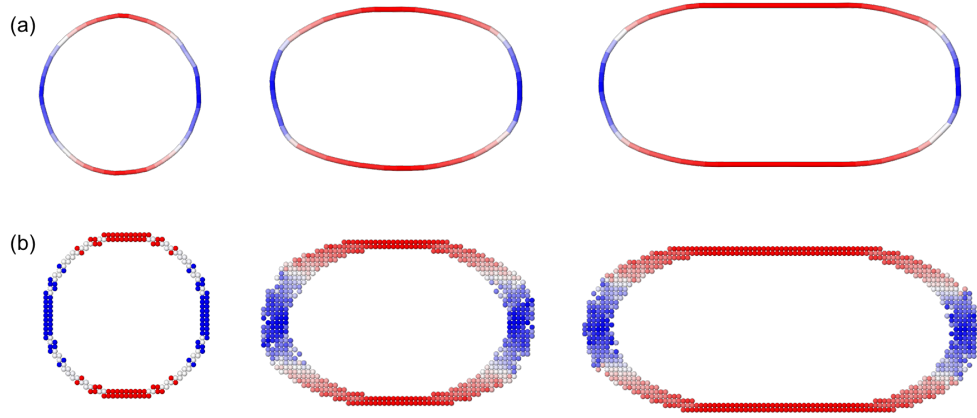


Figure 17: Ta loop expansion snapshots in (a) PFDD (b) MS at normalized time $t = 0, 0.2, 0.4$. The time for each snapshots is normalized with respect to the time that loops reach their steady state. The loops are colored by character with screw-type dislocation shown in red, and edge-type dislocations shown in blue.

Figures 17 and 18 show that, with the addition of line character dependence to the $E^{lattice}$ term, PFDD qualitatively captures the correct loop growth as predicted by MS. Rather than symmetric expansion of the loop, the edge segments propagate while the screw dislocation segments remain relatively stationary and increase in length. This quickly results in an elliptical loop shape. The edge segments continue to propagate until they annihilate with the periodic image dislocations,

leaving two long pure screw dislocation segments. This final configuration is considered to be the steady state solution for these simulations.

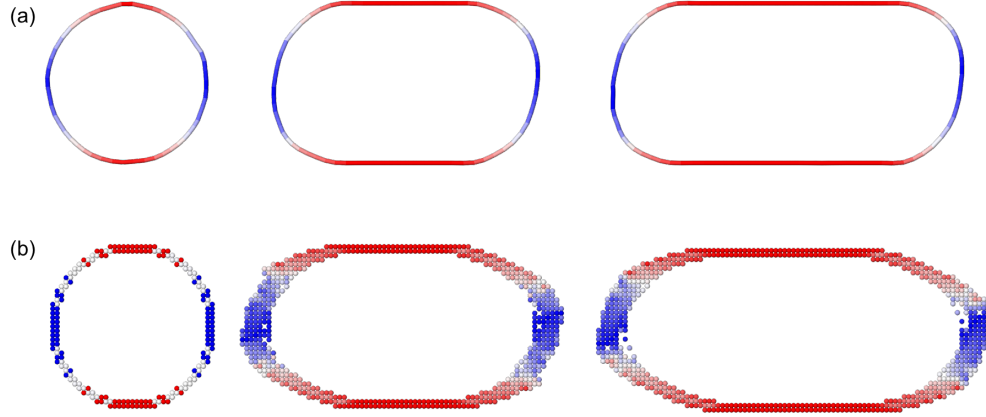


Figure 18: Nb loop expansion snapshots in (a) PFDD (b) MS at normalized time $t = 0, 0.2, 0.4$. Time for each snapshots is normalized with respect to the time that loops reach their steady state. The loops are colored by character with screw-type dislocation shown in red, and edge-type dislocations shown in blue.

Note that, in Figure 18, MS predicts a faceted loop structure for Nb due to the presence of the mixed type dislocation with $\theta = 70.5^\circ$. This is also qualitatively captured by PFDD as the line-character dependent $E^{lattice}$ includes multiple minima as discussed in section 3.1.2.2. This faceted loop structure is slightly more pronounced in the MS results than the PFDD. This may be due in part to the assumption of elastic isotropy used in the PFDD simulations. A more quantitative comparison between the MS and PFDD simulations of dislocation loop expansion is shown in Figure 19. The comparisons are made at different stages of minimization, for which the minimization steps were normalized based on the step at which edge components of the loop interact across the periodic boundaries and annihilate each other.

Figure 19(a) compares the ratio between major and minor axis of the loop. Effectively this metric measures the ratio of the distance between opposite screw components to the distance between the opposite edge components. This ratio is initially close to 1, as the loop is approximately circular, and quickly changes to a value > 1 as the loop expands asymmetrically. A fair agreement is

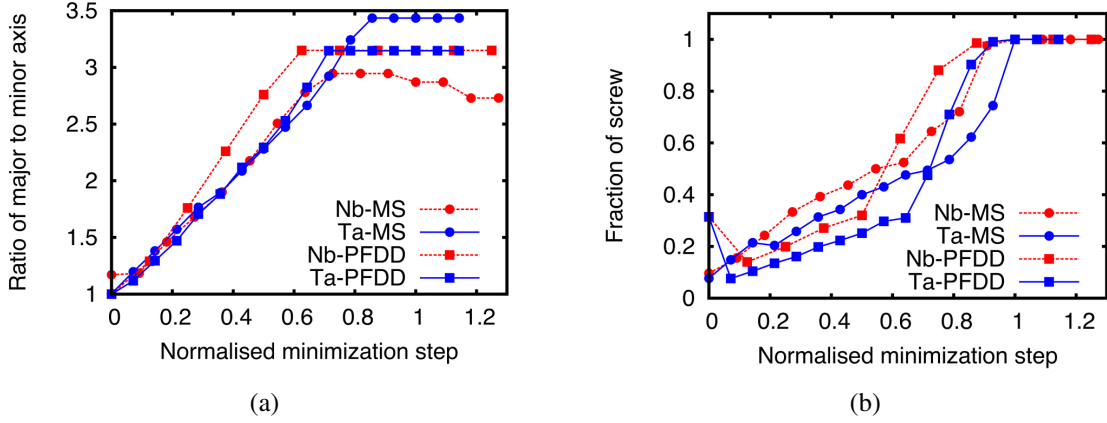


Figure 19: Quantitative comparisons between PFDD and MS for Ta and Nb: (a) Ratio of major to minor axis of dislocation loop (b) Fraction of screw segment.

observed between PFDD and MS predictions, with the ratio saturating to a value ≈ 3 .

The PFDD values more closely match the MS results for Ta. Any differences seen in this case lie primarily in the steady state result, where PFDD slightly under-predicts the MS result. This discrepancy is likely due to the differences in the elastic interaction between the screw type dislocations as captured in MS versus PFDD. The model assumes the material is isotropic and, therefore, the screw and edge segments within the same loop do not interact elastically. As a measure of elastic anisotropy, Zener anisotropy ratios, $A = \frac{2C_{44}}{C_{11}-C_{12}}$, can be calculated as: $A_{Ta} = 1.568$ and $A_{Nb} = 0.499$. Although the departure from unity (signifying isotropy) in the anisotropy ratios is similar for Ta and Nb, $A_{Nb} < 1$ and $A_{Ta} > 1$. In the case of Nb, PFDD shows a very good match in the aspect ratio at the initial stages of loop growth, but quickly starts to over-predict the MS results. Converse to Ta, PFDD over-predicts the steady result calculated by MS for Nb.

Figure 19(b) compares the fraction of the screw dislocation in the expanding loop at various stages of minimization. The fraction was determined by counting all dislocation segments with a line-character $\theta = 0^\circ \pm 10^\circ$ as screw and comparing this to total number of dislocation segments at various stages of minimization. Note that beyond the initial few steps in minimization, both MS and PFDD predict that the expanding loop has a higher screw fraction in Nb compared to Ta. About halfway through the simulation, there is a noticeable change in slope indicating a sudden

growth in screw type dislocations, particularly in the PFDD generated results. This change in slope indicates where elastic interactions with image dislocations start to dominate, motivating the edge type dislocations to annihilate with the neighboring dislocations. This change in slope is present in the MS simulations, although it is more gradual and occurs later in the normalized simulation time.

The PFDD and MS results show reasonable agreement. Interestingly the PFDD results first under-predict the fraction of screw dislocation in the loop, and then over-predict the amount of screw dislocation once the image forces start becoming more dominant. We note that in the initial configuration of the loop in PFDD, there are relatively long screw segments due to the cubic computational grid. Hence, initially the PFDD results show a decrease in the fraction of screw dislocation as the loop quickly relaxes to minimize the amount of screw type dislocation once energy minimization occurs.

3.1.4.2 Propagation of a Straight Screw Dislocation through Kink-Pair Motion. In addition to the expansion of a loop, the propagation of a straight screw dislocation through kink-pair motion in Ta was also modeled in PFDD. Simulation results are shown in Figure 20. The kink-pair is initially placed along the screw dislocation. With an applied stress of 1.77 GPa, the edge segments of the kink-pair rapidly propagate to the end of the simulation cell where they annihilate with the image dislocation in the periodic cells. The screw type-dislocation has then propagated forward by one Burgers vector step.

3.1.5 Conclusions

We have presented a PFDD model extended to BCC metals. In particular, the model extensions are focused on capturing the dependence of the Peierls energy barrier on character. This has been achieved through the addition of a transition function, which describes how the energy for a dislocation to glide through the crystal lattice depends on the dislocation character angle, θ . In this work, the functional form of the energy barrier transition has been informed by MD calculations

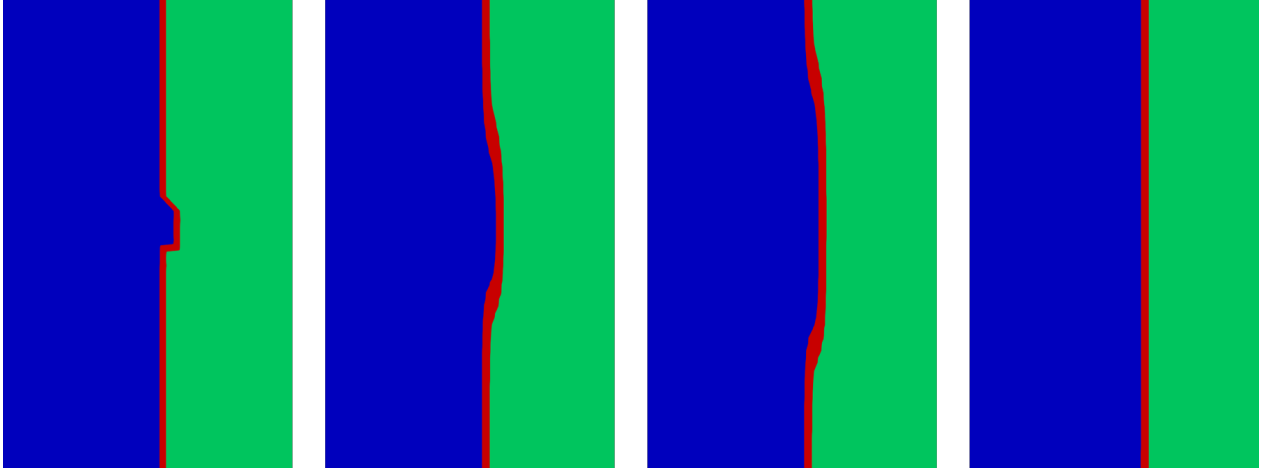


Figure 20: PFDD simulation of screw dislocation motion by propagation of kinks with edge character. Snapshots are shown at normalized time, $t = 0, 0.2, 0.3, 1.0$.

of Peierls stress as a function character for Ta previously reported in [KBC12]. We realize that this approach relies on the quality of the interatomic potential used for the MD simulations, and we note that the form of the transition function could easily be modified as new atomistic data becomes available.

The character dependent PFDD model was demonstrated by modeling expansion of a dislocation loop and propagation of a screw dislocation through kink-pair motion in Ta. In addition, a dislocation loop expansion was modeled in Nb to illustrate the ability of the transition function to extrapolate to other BCC metals beyond Ta. The PFDD results for expansion of a dislocation loop in both Ta and Nb were directly compared to similar simulations completed with MS. The results from the two methods compared reasonably well, with the largest source of error likely being in the calculation of the elastic interactions, which were considered only isotropically in PFDD. Perhaps most notable were the evolution of a faceted loop structure and the higher screw fraction in Nb as shown in the MS calculations, which are also captured by PFDD.

Ultimately, dislocation dynamics in BCC metals are rate dependent, giving rise to a macroscopic deformation response that is highly sensitive to the applied strain rate and temperature. With the mechanistic model in place in the present framework, it is now possible to incorporate temperature and rate effects on dislocation motion. With such additions, this model could model both nucleation

and propagation of kink-pairs for example. Such topics are interesting extensions for future work.

3.2 Non-orthogonal Computational Grids for Studying Dislocation Motion in Phase Field Approaches

In this work, the new non-orthogonal grids are compared to the cubic and rotated grids Previously mentioned. Hence, there are three types of computational grids that are discussed and compared in this work, which we will term as 1) the Rotated Grid, 2) the Cubic or Cartesian Grid and 3) the Non-orthogonal Grid. The “Rotated Grid” and the “Cubic/Cartesian Grid” both rely on a cubic computational grid. However in the “Rotated Grid” the coordinate system is rotated so that the slip plane normal corresponds to the z-direction (e.g., (111) in fcc and (110) in bcc).

This chapter is organized as follows. First in Section 3.2.2, a performance test of the rotated and the cubic grids is first shown, which motivates the use of the non-orthogonal grids. Then in Section 3.2.2.1, a detailed comparison between the three grids is performed with dislocation loop expansion tests. And lastly, an example of two slip planes is illustrated in Section 3.2.2.2 by simulating two loops interacting in the cubic and non-orthogonal grids.

3.2.1 Incorporation of Varying Computational Grids

As mentioned previously, there are three types of grids that are used and compared in this work: 1) the Rotated grid 2) the Cubic or Cartesian grid, and 3) the Non-orthogonal grid, all of which are illustrated in Figure 21. The cubic/Cartesian grid, shown in Figure 21(b), is a fairly standard formulation for computational models, and has the basis $\{e_i^o\}$, with $e_1^o = [1, 0, 0]^T$, $e_2^o = [0, 1, 0]^T$, $e_3^o = [0, 0, 1]^T$. In this case we note that slip planes in general will be at various angles within the computational cell. The example of a (111) FCC slip plane is denoted with red outlines in Figure 21(b).

The rotated, orthogonal grid is similar to the cubic grid. It has the basis $\{e_i\}$, and is rotated from the cubic grid with the rotation matrix being $Q = [e_1|e_2|e_3]$ ($Q^T = Q^{-1}$, $\det Q = 1$). For example, in the case of an FCC crystal, we can rotate the cubic grid such that the slip plane (111) in the cubic

Table 2: FCC and BCC non-orthogonal lattice primitive vectors.

Type	$\bar{\mathbf{p}}_1$	$\bar{\mathbf{p}}_2$	$\bar{\mathbf{p}}_3$
FCC	$\frac{1}{\sqrt{2}}[1\bar{1}0]^T$	$\frac{1}{\sqrt{2}}[01\bar{1}]^T$	$\frac{1}{\sqrt{2}}[101]^T$
BCC	$\frac{1}{\sqrt{3}}[11\bar{1}]^T$	$\frac{1}{\sqrt{3}}[\bar{1}11]^T$	$\frac{1}{\sqrt{3}}[111]^T$

grid is aligned with the xy -plane of the rotated grid, and in this case $\mathbf{e}_1 = \frac{1}{\sqrt{2}}[1, -1, 0]^T$, $\mathbf{e}_2 = \frac{1}{\sqrt{6}}[1, 1, -2]^T$, $\mathbf{e}_3 = \frac{1}{\sqrt{3}}[1, 1, 1]^T$. This example is shown in Figure 21(a), where the (111) glide plane is denoted with a red outline and appears horizontal within the computational cell.

Finally, the non-orthogonal grid has the basis $\{\bar{\mathbf{p}}_i\}$ ($\bar{\cdot}$ – normalization), with $\mathbf{p}_1, \mathbf{p}_2, \mathbf{p}_3$ being the lattice primitives. We denote non-orthogonal lattice primitives as $\{\mathbf{p}_i\}$, so that they are distinguished from orthogonal basis vectors, which are shown as $\{\mathbf{e}_i\}$. Table 2 lists the FCC and BCC primitives that we use to construct their non-orthogonal grids. Figure 21(c) shows an example of the FCC non-orthogonal computational grid. Due to the non-orthogonal primitives, the computational cell no longer appears as a cuboidal cell. Again, a (111) glide plane is highlighted with a red outline.

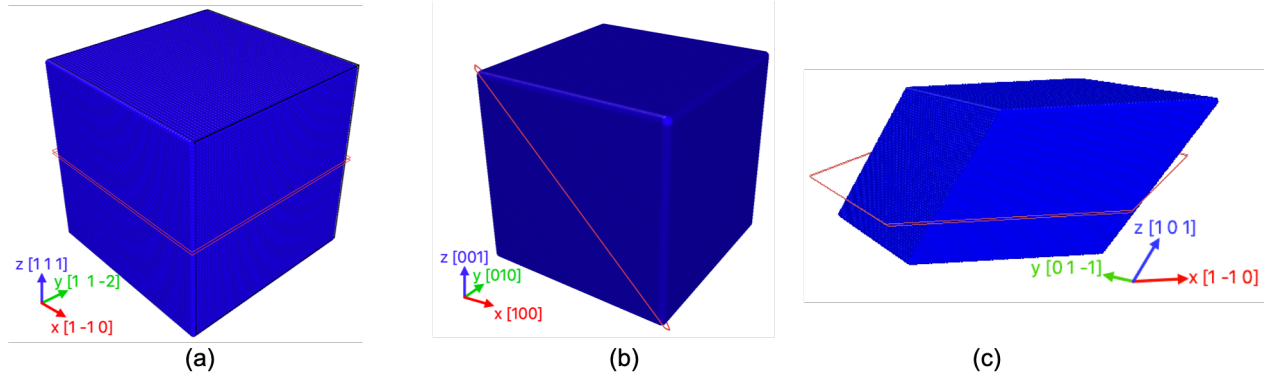


Figure 21: An example of the rotated, cubic and non-orthogonal grids for FCC crystallography. The red lines indicate the (111) slip planes.

For all three computational grids, cubic grid is defined as the global grid where all the calculations are conducted, and the local grid where the dislocation network is assigned can be either of the three grids (rotated/cubic/non-orthogonal). Thus, transformation rules are required between the global and local grids namely for the rotated and non-orthogonal grids. A point $\mathbf{r} \in \mathbb{R}^3$ can be represented

in the global grid as $\mathbf{X}(\mathbf{r})$ and in the local grid as $\mathbf{x}(\mathbf{r})$. The transformation rule between them is:

$$\mathbf{x} = \mathbf{F}^{-1} \mathbf{X} \quad (3.12)$$

where \mathbf{F} is the transformation matrix. $\mathbf{F} = \mathbf{Q}$ when the local grid is a rotated grid; and $\mathbf{F} = [\bar{\mathbf{p}}_1 | \bar{\mathbf{p}}_2 | \bar{\mathbf{p}}_3]$ when the local grid is a non-orthogonal grid. For any $\mathbf{v} \in \mathbb{R}^3$ and $\mathbf{T} \in \mathbb{R}^{3 \times 3}$ the transformation rules are:

$$[\tilde{\mathbf{v}}] = \mathbf{F}^{-1}[\mathbf{v}], \quad (3.13)$$

$$[\tilde{\mathbf{T}}] = \mathbf{F}^{-1}[\mathbf{T}]\mathbf{F} \quad (3.14)$$

where $[\tilde{\cdot}]$ represents the components of \mathbf{v} and \mathbf{T} in the local grid and $[\cdot]$ represents the components in the global grid.

Either choosing a rotated grid or a non-orthogonal grid the transformation rules are the same as in Equation (3.12, 3.13, 3.14), and the rotated grid is a special case when $\mathbf{F} = \mathbf{Q}$. Without loss of generality, the formulation for a local grid will be described for the case of a non-orthogonal grid.

When modeling with non-orthogonal grids for FCC and BCC metals, the dislocation network is assigned to a local non-orthogonal grid. Transformations between the local non-orthogonal grid and the global cubic grid need to be applied in the calculations, including the coordinates of local grid points, the Fourier transform of $\zeta^\alpha(\mathbf{x})$ and the applied stress $\boldsymbol{\sigma}^{appl}$.

The global coordinates of the local grid points follow the transformation rule Equation (3.12):

$$\mathbf{X} = \mathbf{F} \mathbf{x} \quad (3.15)$$

where $\mathbf{x} = (i, j, k)$ is the coordinates of the grid points on the local grid.

The reciprocal lattice (Fourier transform) of the non-orthogonal grid is:

$$[\mathbf{p}_1^f | \mathbf{p}_2^f | \mathbf{p}_3^f] = \mathbf{F}^{-T} \quad (3.16)$$

where $\{\mathbf{p}_i^f\}$ is the basis of the reciprocal lattice. Notice that with orthonormal \mathbf{F} ($\mathbf{F} = \mathbf{I}$ or \mathbf{Q}), which correspond to the cubic and rotated grids respectively, the reciprocal lattice is the same as the original lattice; therefore, the calculation of Equation 3.16 is not required for the cubic and rotated grids. The wave vectors \mathbf{k} is on the reciprocal lattice and can be calculated as:

$$\mathbf{k}(i, j, k) = \frac{i}{N_1} \times \mathbf{p}_1^f + \frac{j}{N_2} \times \mathbf{p}_2^f + \frac{k}{N_3} \times \mathbf{p}_3^f \quad (3.17)$$

where i, j, k are the grid indices and N_1, N_2, N_3 are the grid box size.

3.2.2 Results and Discussion

Here we present two test cases. The first is the expansion of a dislocation loop, presented in Section 3.2.2.1. This problem allows us to compare dislocation motion for all character types in all of the computational grids discussed. This will allow us to verify the newly proposed non-orthogonal computational grid with the more standardly used rotated grids. Following this, in Section 3.2.2.2, we present a test problem in which two loops on different planes interact. This shows some unique advantages of the non-orthogonal grid in comparison to the cubic computational grid.

For all the tests in this work, we use material parameters of Cu (copper) in isotropic Voigt form listed in Table 3. γ_U is the unstable stacking fault energy that corresponds to B in Equation 3.6.

Table 3: Material parameters in the Voigt form. All elastic coefficients are specified in units of GPa.

Material	Lattice parameter (Å)	E	G	ν	γ_U (mJ/m ²)
Cu	3.64	144.4	54.5	0.325	163.7

To better illustrate the numerical errors associated with the commonly used orthogonal computational grids, we first present results for the stress fields surrounding a straight edge dislocations. We calculated the stress field of a Cu straight edge dislocation line $[1\bar{1}0](111)$ in an infinite medium with both PFDD rotated and cubic grids, which are then compared to the analytical solution [HL68] in Figure 22. The grid spacing along the x direction (Burgers vector direction) is b , and along the z direction (slip plane normal direction) is b for the rotated grid and analytical solution, $\sqrt{6}/2b$ for the cubic grid.

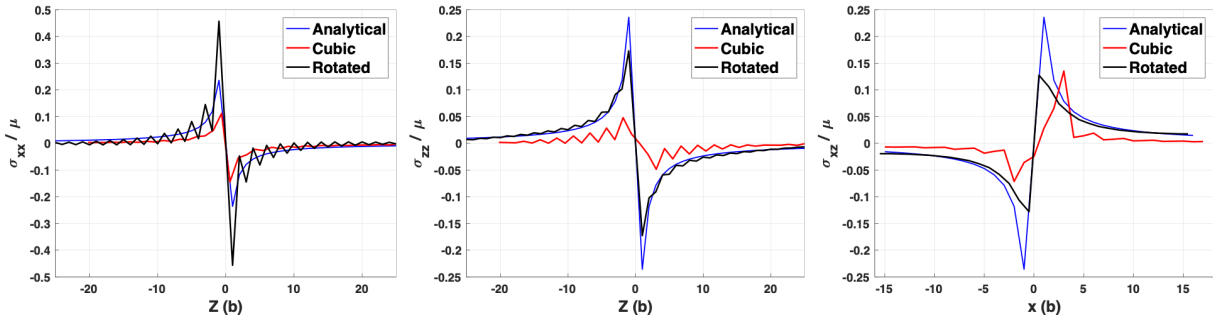


Figure 22: Stresses normalized with shear modulus left: σ_{xx} , middle: σ_{zz} , right: σ_{xz} of a Cu straight edge dislocation $[1\bar{1}0](111)$ calculated with PFDD rotated and cubic grids and compared to the analytical solution. σ_{xx} and σ_{zz} are plotted along $z[111]$ direction and σ_{xz} is plotted along $x[1\bar{1}0]$ direction at the dislocation.

Both the rotated and cubic grids show Gibbs oscillations from the discontinuous stress fields caused by the dislocations. Oscillations are apparent in σ_{zz} and σ_{xz} for the cubic grid, but only in σ_{xx} for the rotated grid. Apart from the oscillations, the rotated grid results match to the analytical ones. The cubic grid also has the peaks less in magnitude and wider than the peaks in the rotated grid and analytical solution.

A simple explanation is that the inclined slip plane in the cubic grid makes the discontinuity spread out onto all three axes of the grid, and make it more difficult for a Fourier series representation. Here by “discontinuity” we mean the out of plane discontinuity of the order parameter. The order parameter is confined on its slip plane, but the system is described with a 3D structure, a cube in this case. Even though there are also discontinuities on the slip plane, the order parameter is smoothed out in the PFDD algorithm on the plane, so less oscillations are expected on the in-plane

component, namely σ_{xz} . Consequently, expanding to systems in which several dislocations are operating on non-coplanar slip systems, these errors in the stress fields could impact dislocation interactions and reactions.

By refining the grid, the Gibbs oscillations can be reduced but not completely eliminated without special treatments. This is shown in Figure 23, which presents the comparison between the analytical solution, the rotated grid with a cell size of $64b \times 64b \times 64b$ and the refined rotated grid, which has a simulation cell size of $256b \times 256b \times 256b$. As expected, oscillations are less in magnitude for the refined grid. Overall the presence of Gibbs oscillations is a common issue with FFT-based methods, but many approaches such as using “centered” [DMO99] and “rotated” [Wil15] Green operator have been proved effective. In this work, however, suppressing the oscillations is not the main focus. We only consider the use of the original FFT method without any treatment directly on the oscillations.

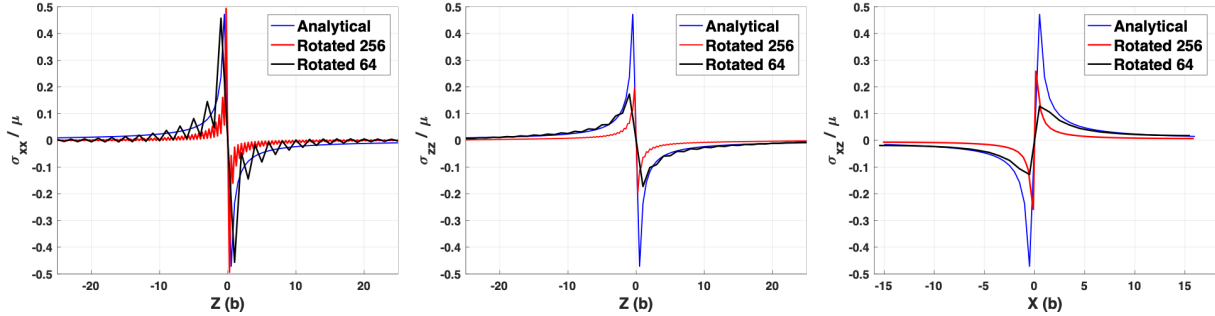


Figure 23: Stresses normalized with shear modulus left: σ_{xx} , middle: σ_{zz} , right: σ_{xz} of a Cu straight edge dislocation $[1\bar{1}0](111)$ calculated with analytical solution, the PFDD rotated grid $64b \times 64b \times 64b$ and the refined rotated grid $256b \times 256b \times 256b$. σ_{xx} and σ_{zz} are plotted along $z[111]$ direction and σ_{xz} is plotted along $x[1\bar{1}0]$ direction at the dislocation.

3.2.2.1 Loop expansion tests on three grids. To show the performance of the non-orthogonal grid, we conduct a test of stress comparisons of a dislocation loop on the rotated, cubic and non-orthogonal grids. In this test problem, a Cu dislocation loop of radius $r = 10b$ is assigned onto a (111) slip plane with $\mathbf{b} = \frac{1}{2}[1\bar{1}0]$ in the different grids. Figure 21 shows these three grids, and Figure 24 shows their corresponding (111) slip planes with the dislocation loops. The grid sizes

are $64b \times 64b \times 64b$ (cubic), $48a \times 48a \times 48a$ (rotated) and $64b \times 64b \times 64b$ (non-orthogonal), so that the length of the yellow dashed lines in Figure 24 are $64b$ and grid spacing along \mathbf{b} is b . While these grid spacings are different, the aim was to keep the same resolution along the Burgers vector direction to enable a fair comparison.

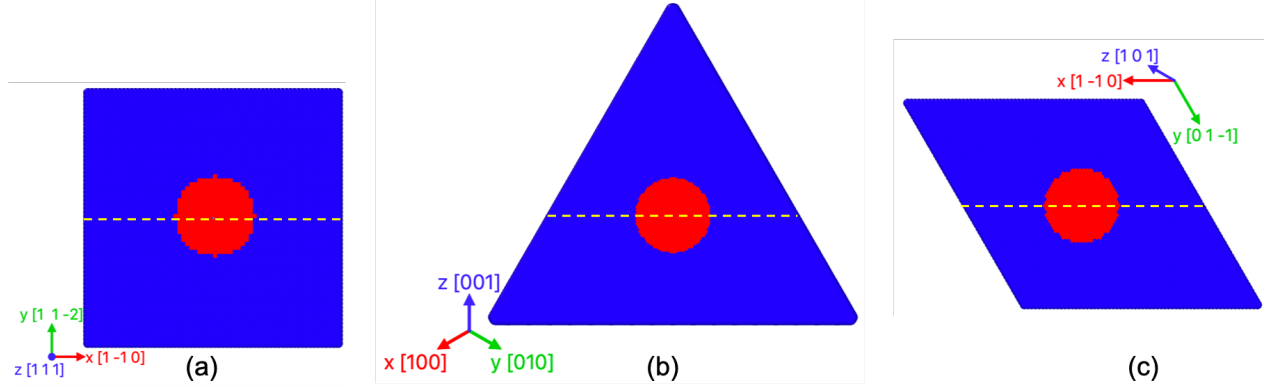


Figure 24: Cu dislocation loops on the (111) slip planes of (a) rotated grid (b) cubic grid and (c) non-orthogonal grid. The sizes of the loops are $r = 10b$ and the lengths of the dashed yellow lines which follow the \mathbf{b} direction are $64b$.

We apply a shear stress to the loops in the crystals for each case. In the rotated grid, the applied stress is $\sigma_{xz} = 0.06\mu$, and directly corresponds to the resolved shear stress on the glide plane. The corresponding applied stress tensor in the cubic and non-orthogonal grids has more non-zero stress components and is determined with the transformation rule shown in Equation (3.14). These stress tensors produce an equivalent resolved shear stress on the glide plane as is specified in the rotated grid.

Under the applied stress, the loops expand. First, in Figure 25, we compare the stresses of the one of the edge segments in the dislocation loops on the rotated, cubic and non-orthogonal grids at step 0 before they start to expand. Figure 25 shows good agreement between the rotated and the non-orthogonal grids in all three stress components. Notably, the stress fields calculated on the non-orthogonal grid show no oscillations. The cubic grid, however, not only fail to match to the other two on σ_{xx} and σ_{zz} (the peaks are less in magnitude and wider than the other two grids' peaks) but also show more noticeable oscillations on σ_{zz} .

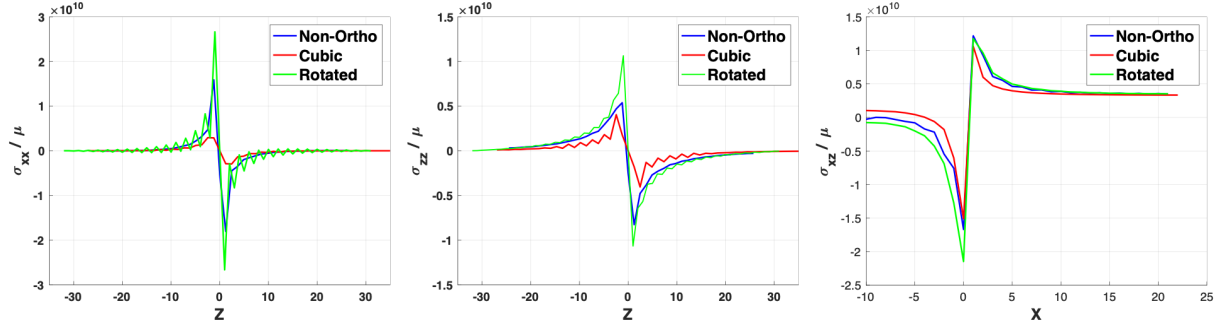


Figure 25: Stresses normalized with shear modulus left: σ_{xx} , middle: σ_{zz} , right: σ_{xz} of a Cu dislocation loop $[1\bar{1}0](111)$ calculated with the non-orthogonal grid, the cubic grid and the rotated grid at step 0. σ_{xx} and σ_{zz} are plotted along $z[111]$ direction and σ_{xz} is plotted along $x[1\bar{1}0]$ direction at the edge segments.

Next, we compare the stresses after the loops have expanded. Figure 26 compares the shape of the loops at time step 100. While the dislocation loops across all three grids have equivalent major axes, the loop shapes themselves show some differences. In the rotated and non-orthogonal grids the loop shapes are not perfectly circular. The oval shape is most apparent in the rotated grid. Even in an FCC metal where edge, screw, and mixed type dislocation have the same mobility, the screw type dislocations have a lower self energy. Since the order parameters in PFDD are evolved base on energy minimization, it becomes energetically favorable to maximize the screw components of the dislocation loop. This effect of the dislocation self energy is lost in the cubic grid, which reproduces nearly a perfectly circular loop shape.

Figure 27 shows the stresses at an edge segment within the dislocation loops. The non-orthogonal and the rotated grids give similar results for all stress components. The out of slip plane stress σ_{xx} of the cubic grid has a much lower peak than the other two grids, and σ_{zz} has more oscillations. Again, only the stress field calculated with the non-orthogonal grid show no oscillations.

To test if by refining the grid, the cubic grid can reduce the oscillations and yield better results, we refine the cubic grid by reducing the grid spacing by half (i.e., to $0.5b$). Figure 28 compares the three stress components among the cubic grid, the refined cubic grid and the non-orthogonal grid. While a finer cubic grid slightly improves the agreement and reduced the oscillations, it is still not as good as the non-orthogonal grid with the coarser spacing.

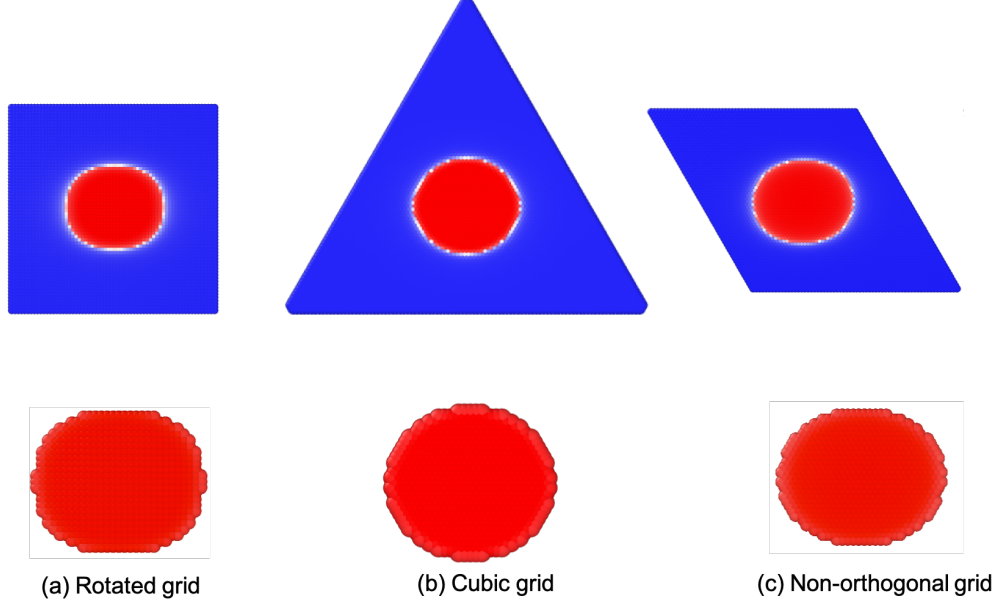


Figure 26: Dislocation loops in (a) rotated (b) cubic and (c) non-orthogonal grids at step 100. Top row shows the loops on their slip plane and bottom row shows the zoomed-in loop shapes.

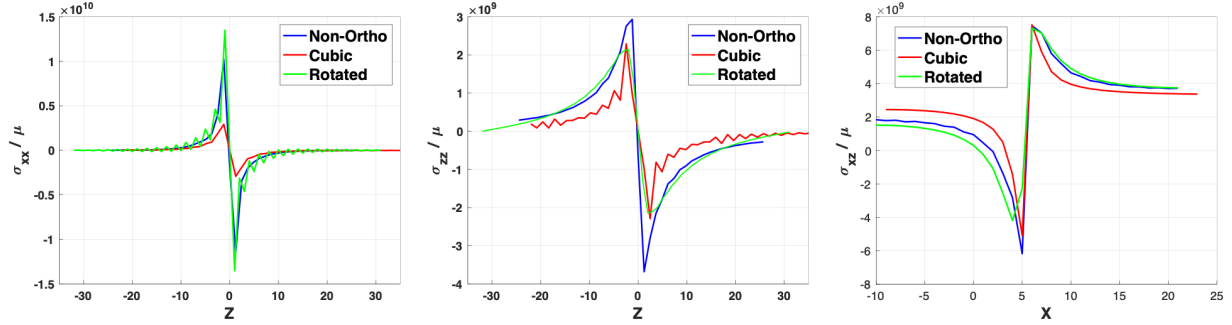


Figure 27: Stresses normalized with shear modulus left: σ_{xx} , middle: σ_{zz} , right: σ_{xz} of a Cu dislocation loop $[1\bar{1}0](111)$ calculated with the non-orthogonal grid, the cubic grid and the rotated grid at step 100. σ_{xx} and σ_{zz} are plotted along $z[111]$ direction and σ_{xz} is plotted along $x[1\bar{1}0]$ direction at the edge segments.

3.2.2.2 Two loop annihilation test on non-orthogonal grid. Next we consider the case where 2 loops lying on different, non-parallel $\{111\}$ planes are driven to interact under an applied stress. With 2 slip planes, the rotated grid can accommodate one so that it is perfectly aligned, but the other slip plane will be inclined. And for the cubic grid, both the 2 slip planes are inclined. Here we use the cubic grid and the non-orthogonal grid to maximize the differences brought by the inclined planes.

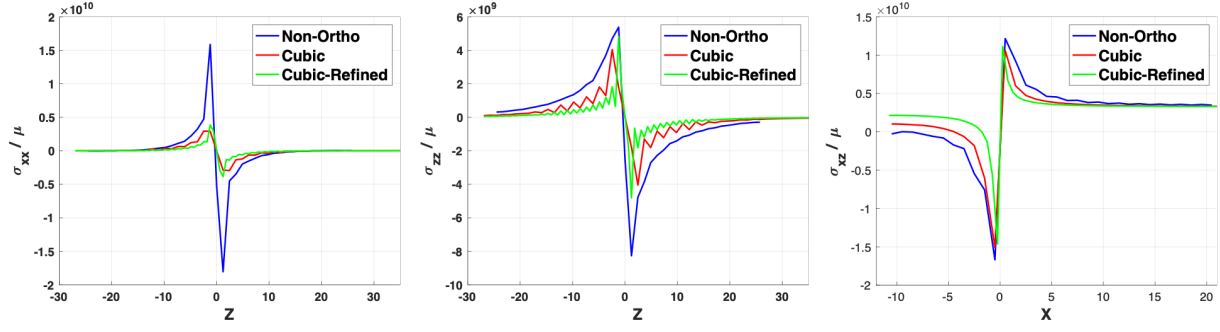


Figure 28: Stresses normalized with shear modulus left: σ_{xx} , middle: σ_{zz} , right: σ_{xz} of a Cu dislocation loop $[1\bar{1}0](111)$ calculated with the cubic grid, the refined cubic grid and the non-orthogonal grid at step 0. σ_{xx} and σ_{zz} are plotted along $z[111]$ direction and σ_{xz} is plotted along $x[1\bar{1}0]$ direction at the edge segments.

Figure 29 shows the set up consisting of 2 dislocation loops of same size $r = 6b$ in a $64b \times 64b \times 64b$ non-orthogonal grid. The loop on slip system $(111)[1\bar{1}0]$ is marked in red and the one on $(11\bar{1})[1\bar{1}0]$ is in blue.

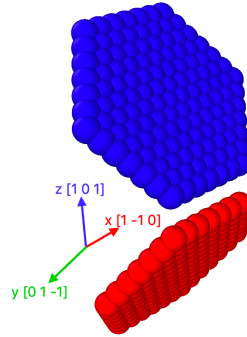


Figure 29: Two dislocation loops on non-coplanar slip systems in the non-orthogonal grid. Both loops have the same slip direction, $[1\bar{1}0]$, and different slip plane normals: (111) (red loop) and $(11\bar{1})$ (blue loop).

Under applied stress (shear stress, equivalent to the σ_{xz} used in the one loop test), both loops grow, and intersect at their screw segments. In this configuration, screw segments from each loop will meet and intersect. These segments have the same slip direction ($[1\bar{1}0]$), but opposite line sense, thus they should annihilate. This is shown in Figure 30. The two loops approach each other, intersect, and then continue to expand within their respective glide planes. The screw segments that meet at the intersection point, do indeed annihilate; this point is highlighted in white in the figure.

In contrast, in the case of the cubic grid, shown in Figure 31, the annihilation between screw

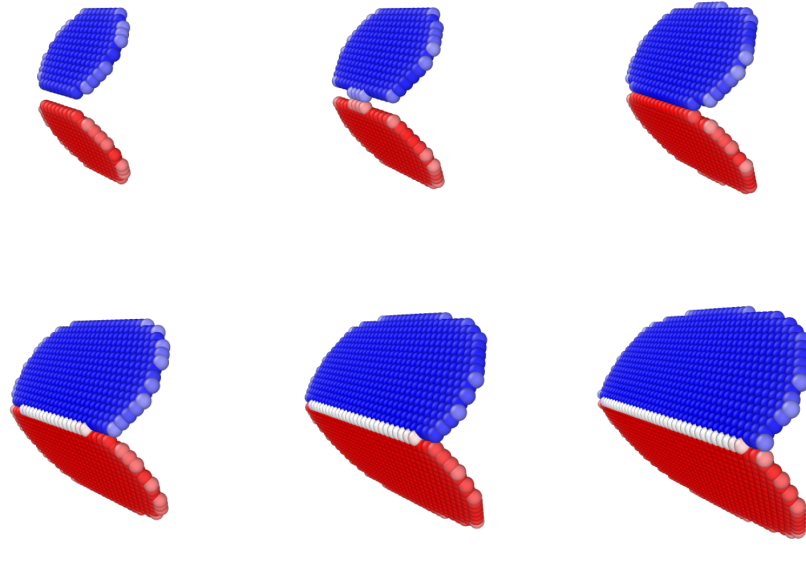


Figure 30: Snapshots of two dislocation loops expanding in the non-orthogonal grid. The loops expand, meet and annihilate at screw segment marked in white.

segments is not capture. Rather as the dislocations expand and meet, they intersect and continue propagating instead of annihilating. In this case, the dislocation reaction is not appropriately captured, resulting in unphysical behavior. The two loops on the two inclined slip planes are assigned such that there is no misalignment (all grid points representing the loops are on the planes, and the planes intersect each other at the same set of grid points). So the fail to annihilation is due to the numerical errors associated with the inclined planes rather than misalignment. This agrees with the what we have seen in the stress calculations, where there is also no misalignment but results from the cubic grids have more errors.

3.2.3 Conclusions

Non-orthogonal grids outperforms the rotated grids that are previously applied to many problems. Without any special treatment to the FFT method used in the PFDD formulation, calculations on the non-orthogonal grids show no oscillations caused by Gibbs effect.

A slip plane lies on the grid plane for the rotated grid but is inclined when using the cubic grid.

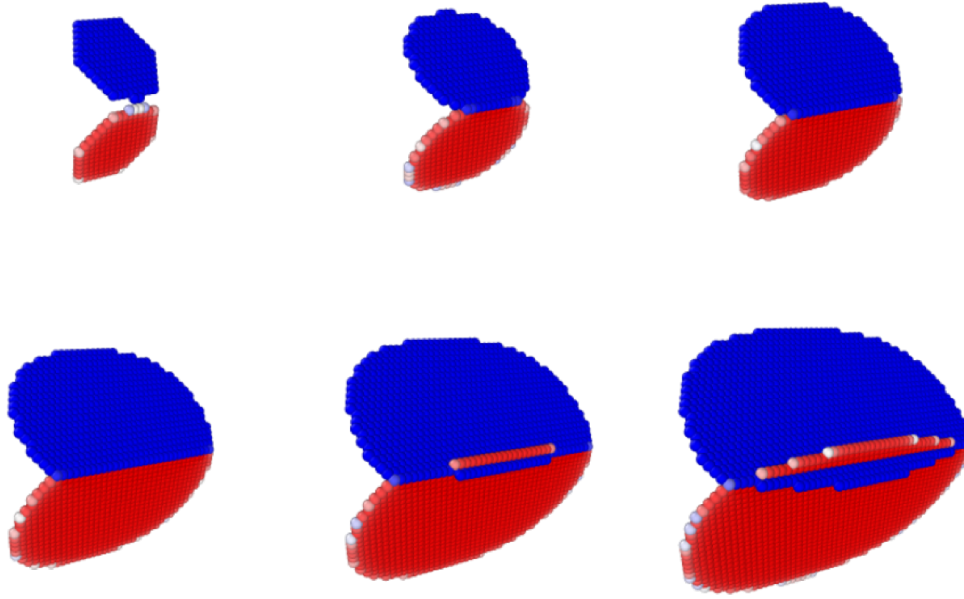


Figure 31: Snapshots of two dislocation loops expanding in the cubic grid. The loops expand, meet but do not annihilate.

This difference of the plane orientations induce numeric errors that are not able to be resolved by refining the grid.

In the two-loop test, the non-orthogonal grid correctly capture the interactions and reactions of the two loops, enables the annihilation at the screw segments when the two loops expand and meet, which the cubic grid fails. Non-orthogonal grids avoid the numerical errors associated with the inclined slip plane and reproduce true physical behaviors. Solving systems with multiple non-coplanar slip planes by the non-orthogonal grids is shown to be effective.

4 Computational Methods for High-contrast Composites

This is joint work with experimentalists at Air Force Research Laboratory, led by Dr. Dhriti Nepal's group in the Composites Branch. This work has been published in [PND20]. This chapter is organized as follows:

- Section 4.1 summarizes the Classical FFT method;
- Section 4.2 describes the RPM-FFT method;
- Section 4.3 provides a variational perspective;
- Section 4.4 provides numerical examples and comparisons.

4.1 Classical FFT Method Based on Fixed-Point Iteration

The original FFT method proposed by Moulinec and Suquet [MS98], and some subsequent improvements, are briefly summarized below in the setting of linear elasticity. The goal is to solve the linear elasticity problem on a unit cell V in a periodic geometry with a heterogeneous medium. The average symmetric strain tensor \mathbf{E} is given.

We use $\mathcal{F}[\cdot]$, $\hat{\cdot}$, $\mathcal{F}^{-1}[\cdot]$ respectively to denote the Fourier transform, Fourier space representation, and inverse Fourier transform.

The displacement field $\mathbf{u}(\mathbf{x})$ is decomposed into a linear part and a zero-mean fluctuating part: $\mathbf{u}(\mathbf{x}) = \mathbf{E} \cdot \mathbf{x} + \mathbf{v}(\mathbf{x})$, ignoring a constant. This implies the strain decomposition $\boldsymbol{\epsilon}_u(\mathbf{x}) = \mathbf{E} + \boldsymbol{\epsilon}_v(\mathbf{x})$, where $\boldsymbol{\epsilon}_{(\cdot)} := \frac{1}{2} (\nabla(\cdot) + \nabla(\cdot)^T)$ is the strain.

We notice that $\hat{\boldsymbol{\epsilon}}_v(\mathbf{k}) = \hat{\boldsymbol{\epsilon}}_u(\mathbf{k}) \forall \mathbf{k} \neq \mathbf{0}$, and $\hat{\boldsymbol{\epsilon}}_u(\mathbf{0}) = \mathbf{E}$ while $\hat{\boldsymbol{\epsilon}}_v(\mathbf{0}) = \mathbf{0}$. Therefore, for conciseness after this section, we will use $\hat{\boldsymbol{\epsilon}}$ to represent both $\hat{\boldsymbol{\epsilon}}_v$ and $\hat{\boldsymbol{\epsilon}}_u$, and $\boldsymbol{\epsilon}$ to represent both $\boldsymbol{\epsilon}_u$ and $\boldsymbol{\epsilon}_v$.

The unit cell problem can then be written as

$$\operatorname{div} \boldsymbol{\sigma}(\mathbf{x}) = \mathbf{0} \quad \forall \mathbf{x} \in V \quad (4.1)$$

$$\boldsymbol{\sigma}(\mathbf{x}) = \mathbf{C}(\mathbf{x}) \boldsymbol{\epsilon}_u(\mathbf{x}) \quad (4.2)$$

where $\boldsymbol{\sigma}$ is the stress field, and is periodic.

We can then introduce, following [MB12, MS14, EM99] and others, a homogeneous linear elastic comparison medium with stiffness \mathbf{C}^0 and the polarization $\boldsymbol{\tau}(\mathbf{x}) := (\mathbf{C}(\mathbf{x}) - \mathbf{C}^0) \boldsymbol{\epsilon}_u(\mathbf{x})$. This enables us to rewrite the stress-strain relation as:

$$\boldsymbol{\sigma}(\mathbf{x}) = \mathbf{C}^0 \boldsymbol{\epsilon}_v(\mathbf{x}) + \boldsymbol{\tau}(\mathbf{x}) + \mathbf{C}^0 \mathbf{E} \quad (4.3)$$

The solution to the unit cell problem can be written in terms of the periodic Greens function $\boldsymbol{\Gamma}^0$ corresponding to \mathbf{C}^0 :

$$\boldsymbol{\epsilon}_v(\mathbf{x}) = -\boldsymbol{\Gamma}^0(\mathbf{x}) * \boldsymbol{\tau}(\mathbf{x}) \quad \forall \mathbf{x} \in V \quad (4.4)$$

The Fourier space representation of this relation is:

$$\hat{\boldsymbol{\epsilon}}_v(\mathbf{k}) = -\hat{\boldsymbol{\Gamma}}^0(\mathbf{k}) \hat{\boldsymbol{\tau}}(\mathbf{k}) \quad \forall \mathbf{k} \neq \mathbf{0}; \quad \hat{\boldsymbol{\epsilon}}_v(\mathbf{0}) = \mathbf{0} \quad (4.5)$$

Typical FFT methods use the fact that taking the (fast) Fourier transform and then multiplying in Fourier space is much faster than convolution in real-space. However, we note that both the real and Fourier representations in (4.4, 4.5) are implicit, through the dependence of the effective forcing $\boldsymbol{\tau}$ on the solution \mathbf{u} . Therefore, further work is required to solve this (linear) implicit equation.

From a linear algebra perspective, the Fourier transform takes us to the eigenbasis in a homogeneous problem; in a heterogeneous problem, the Fourier transform brings us close to the eigenbasis, and further calculations are required to completely diagonalize the operator. Roughly, one can make

an analogy between the effort to completely diagonalize and the effort to solve the implicit equation in Fourier space.

The implicit equations are typically solved with fixed point methods, and variations of these. In [MS98], for instance, they use the iteration $\hat{\epsilon}^{i+1}(\mathbf{k}) = \hat{\epsilon}^i(\mathbf{k}) - \hat{I}^0(\mathbf{k})\hat{\sigma}^i(\mathbf{k})$; see Algorithm 3. Like all fixed point methods, convergence is slow or lost when the problem contains an unstable subspace. This is precisely the case when there is large contrast leading to flat energy landscapes and loss of uniqueness, as has been observed in practice [EM99].

Algorithm 3 Classical FFT algorithm [MS98]

```

1: Initialization
2:  $\epsilon^0 \leftarrow E; \quad \sigma^0 \leftarrow C(x) : \epsilon^0$ 
3: Iteration  $(\epsilon^0, \sigma^0)$ 
4: while error > tolerance do
5:    $\hat{\epsilon}^i \leftarrow \mathcal{F}[\epsilon^i]; \quad \hat{\sigma}^i \leftarrow \mathcal{F}[\sigma^i]$  ▷ FFT on  $\epsilon$  and  $\sigma$ 
6:    $\hat{\epsilon}^{i+1} \leftarrow \hat{\epsilon}^i - \hat{I}^0 : \hat{\sigma}^i$  ▷  $\forall \mathbf{k} \neq \mathbf{0}; \hat{\epsilon}^{i+1}(\mathbf{0}) = E$ 
7:    $\epsilon^{i+1} \leftarrow \mathcal{F}^{-1}[\hat{\epsilon}^{i+1}]$ 
8:    $\sigma^{i+1} \leftarrow C(x) : \epsilon^{i+1}$ 
9:   error  $\leftarrow \frac{(\langle \|\mathbf{k} \cdot \hat{\sigma}(\mathbf{k})\|^2 \rangle)^{1/2}}{\|\hat{\sigma}(\mathbf{0})\|} \equiv \frac{(\langle \|\text{div } \sigma\|^2 \rangle)^{1/2}}{\|\langle \sigma \rangle\|}$ 
10: end while

```

4.2 The Proposed RPM-FFT Method

We first outline the key elements of the recursive projection method following the seminal work of Shroff and Keller [SK93], and then the application of RPM to the FFT approach.

When using fixed-point iterative procedures to solve nonlinear problems, slow convergence or even divergence can be caused by a small number of eigenvalues of the Jacobian matrix approaching or leaving the unit disk $\{|z| < 1\}$. The Recursive Projection Method (RPM) is a stabilization procedure that can recover the convergence.

Consider a problem in N dimensions posed on \mathbb{R}^N . The method begins by dividing the space \mathbb{R}^N into \mathbb{P} , that we denote as the *unstable eigenspace*, and its orthogonal complement \mathbb{Q} . \mathbb{P} and \mathbb{Q} correspond respectively to the eigenspace of those eigenvalues leaving the disk and those inside

the disk. Then, the fixed-point iteration is performed only on the complement \mathbb{Q} while Newton's method – or, in practice, a variation such as quasi-Newton – is performed on the unstable eigenspace \mathbb{P} .

Writing the original problem to be solved in the fixed-point form as follows:

$$\mathbf{u} = \mathbf{F}(\mathbf{u}), \quad \mathbf{F}: \mathbb{R}^N \rightarrow \mathbb{R}^N \quad (4.6)$$

the fixed-point iteration can be written:

$$\mathbf{u}^{(\nu+1)} = \mathbf{F}(\mathbf{u}^{(\nu)}) \quad (4.7)$$

where ν indicates the iteration number. While the eigenvalues of the Jacobian matrix $\mathbf{F}_u := \frac{\partial \mathbf{F}}{\partial \mathbf{u}}$ lie inside of the disk

$$K_\delta = \{|z| \leq 1 - \delta\} \quad \text{for some } \delta > 0 \quad (4.8)$$

and the initial value $\mathbf{u}^{(0)}$ is sufficiently close to the solution, the fixed-point iteration will converge. A small positive constant δ is used to ensure that one is sufficiently far from the boundary between stable and unstable fixed point iterations.

Suppose now that m eigenvalues lie outside the disk K_δ

$$|\mu_1| \geq \dots \geq |\mu_m| > 1 - \delta \geq |\mu_{m+1}| \geq \dots \geq |\mu_N| \quad (4.9)$$

Let $\mathbf{Z} \in \mathbb{R}^{N \times m}$ be the orthonormal basis for \mathbb{P} . The projectors of the subspaces \mathbb{P} and \mathbb{Q} are respectively $\mathbf{P} = \mathbf{Z}\mathbf{Z}^T$ and $\mathbf{Q} = \mathbf{I} - \mathbf{Z}\mathbf{Z}^T$. For each $\mathbf{u} \in \mathbb{R}^n$, there is a unique decomposition:

$$\mathbf{u} = \mathbf{p} + \mathbf{q}, \quad \mathbf{p} \equiv \mathbf{P}\mathbf{u} \in \mathbb{P}, \quad \mathbf{q} \equiv \mathbf{Q}\mathbf{u} \in \mathbb{Q} \quad (4.10)$$

This allows the introduction of $\mathbf{f}(\mathbf{p}, \mathbf{q}) := \mathbf{P}\mathbf{F}(\mathbf{p} + \mathbf{q})$ and $\mathbf{g}(\mathbf{p}, \mathbf{q}) := \mathbf{Q}\mathbf{F}(\mathbf{p} + \mathbf{q})$.

Applying Newton's method on the unstable subspace \mathbb{P} :

$$\mathbf{p}^{(\nu+1)} = \mathbf{p}^{(\nu)} + (\mathbf{I} - \mathbf{f}_p^{(\nu)})^{-1}(\mathbf{f}(\mathbf{p}^{(\nu)}, \mathbf{q}^{(\nu)}) - \mathbf{p}^{(\nu)}) \quad (4.11)$$

where $\mathbf{f}_p(\mathbf{p}^{(\nu)}, \mathbf{q}^{(\nu)}) = \mathbf{P}\mathbf{F}_u(\mathbf{u}^{(\nu)})\mathbf{P}$ is the derivative of \mathbf{f} with respect to \mathbf{p} .

We continue to use fixed-point iteration on \mathbb{Q} :

$$\mathbf{q}^{(\nu+1)} = \mathbf{g}(\mathbf{p}^{(\nu)}, \mathbf{q}^{(\nu)}) \quad (4.12)$$

Efficiently identifying the unstable eigenspace \mathbb{P} is an essential feature of RPM. This corresponds to finding the basis \mathbf{Z} ; or, in practice, an approximation of \mathbf{Z} since the Jacobian matrix can be expensive to compute. In [SK93], this is accomplished directly by monitoring the convergence rate of $\mathbf{q}^{(\nu)}$, without computing the Jacobian matrix. This is an important feature that significantly reduces the computational cost, and we follow that procedure here.

The method begins by assuming that the unstable eigenspace \mathbb{P} is 0-dimensional and $\mathbf{Z} = \mathbf{0}$. We then iteratively build up the unstable eigenspace by adding to \mathbf{Z} the eigenspace corresponding to those eigenvalues that approach the unit disk. The eigenspace that corresponds to the eigenvalues approaching the unit disk corresponds to the dominant eigenspace of $\mathbf{g}_q = \mathbf{Q}\mathbf{F}_u\mathbf{Q}$.

If the fixed-point iteration does not converge within the specified limit of iterations n_{max} , the eigenspace corresponding to the eigenvalues approaching the unit disk is identified as follows. In [SK93], it is shown that $\Delta\mathbf{q}^{(\nu)} \equiv \mathbf{q}^{(\nu+1)} - \mathbf{q}^{(\nu)} \approx (\mathbf{g}_q)^\nu \Delta\mathbf{q}^{(0)}$, i.e., a power iteration with \mathbf{g}_q applied to $\Delta\mathbf{q}^{(0)}$. From the properties of power iterations, $\Delta\mathbf{q}^{(\nu)}$ identifies the eigenspace of \mathbf{g}_q that corresponds to the largest eigenvalue, assuming that $\Delta\mathbf{q}^{(0)}$ has a nonzero component in this space.

Following [SK93], we approximate the dominant eigenspace of \mathbf{g}_q using QR factorization to write:

$$\mathbf{D} \equiv [\Delta\mathbf{q}^{(\nu)}, \Delta\mathbf{q}^{(\nu-1)}] =: \tilde{\mathbf{D}}\mathbf{T} \quad (4.13)$$

where $\tilde{\mathbf{D}} \in \mathbb{R}^{N \times 2}$ is orthogonal and $\mathbf{T} \in \mathbb{R}^{2 \times 2}$ is upper triangular. When $T_{11} \gg T_{22}$, we add the first column of $\tilde{\mathbf{D}}$ to the basis \mathbf{Z} , corresponding to one real eigenvalue approaching the unit disk. Else, we add both columns of $\tilde{\mathbf{D}}$ to the basis \mathbf{Z} , corresponding to a complex conjugate pair of eigenvalues approaching the unit disk. Alternate approximations are further discussed in [SK93].

To apply the RPM method to the specific context of the FFT fixed-point algorithm, we formally define the fixed-point operator \mathbf{F} from Algorithm 3 through the equation:

$$\epsilon^{i+1} = \mathcal{F}^{-1} \left[\mathcal{F}[\epsilon^i] - \hat{\Gamma}^0 : \mathcal{F}[\mathbf{C}(\mathbf{x}) : \epsilon^i] \right] \quad (4.14)$$

Define $\mathbf{z} := \mathbf{Z}^T \mathbf{p} \in \mathbb{R}^m$ to represent \mathbf{p} in the basis \mathbf{Z} . Then the stable / unstable decomposition can also be written as:

$$\mathbf{u} = \mathbf{Z}\mathbf{z} + \mathbf{q}, \quad \mathbf{p} = \mathbf{Z}\mathbf{z}, \quad \mathbf{q} = (\mathbf{I} - \mathbf{Z}\mathbf{Z}^T)\mathbf{u} \quad (4.15)$$

It is suggested in [SK93] that it is often sufficient for convergence to simply compute only once the quantity $(\mathbf{I} - \mathbf{f}_p)^{-1}$ using finite differences. In our calculations in this work, we have also found this to be sufficient for convergence, and of course very efficient.

Defining $\mathbf{H} := \mathbf{Z}^T \mathbf{F}_u \mathbf{Z}$, the iteration (4.11, 4.12) can now be rewritten in a form that is more efficient and transparent for implementation:

$$\mathbf{z}^{(\nu+1)} = \mathbf{z}^{(\nu)} + (\mathbf{I} - \mathbf{H})^{-1}(\mathbf{Z}^T \mathbf{F}(\mathbf{u}^{(\nu)}) - \mathbf{z}^{(\nu)}) \quad (4.16)$$

$$\mathbf{q}^{(\nu+1)} = (\mathbf{I} - \mathbf{Z}\mathbf{Z}^T)\mathbf{F}(\mathbf{u}^{(\nu)}) \quad (4.17)$$

$$\mathbf{u}^{(\nu+1)} = \mathbf{Z}\mathbf{z}^{(\nu+1)} + \mathbf{q}^{(\nu+1)} \quad (4.18)$$

Finally, integrating the FFT method into RPM, gives us Algorithm 4.

An important feature is that the fixed-point iteration is conducted on the entire solution space and not only on the stable subspace. After the fixed-point iteration, only that part of the outcome corre-

Algorithm 4 RPM-FFT algorithm

```
1: Initialization
2:  $\epsilon^0 \leftarrow E; \xi^0 \leftarrow F(\epsilon^0)$ 
3: Iteration ( $\epsilon^0, \xi^0$ )
4: while error > tolerance do
5:    $z^{(\nu)} \leftarrow Z^T \epsilon^{(\nu)}; \zeta^{(\nu)} \leftarrow Z^T \xi^{(\nu)}$  ▷ Project to unstable subspace
6:    $z^{(\nu+1)} \leftarrow z^{(\nu)} + (I - H)^{-1}(\zeta^{(\nu)} - z^{(\nu)})$  ▷ Newton iteration
7:    $q^{(\nu+1)} \leftarrow \xi^{(\nu)} - Z \zeta^{(\nu)}$ 
8:    $\epsilon^{(\nu+1)} \leftarrow Z z^{(\nu+1)} + q^{(\nu+1)}$ 
9:    $\xi^{(\nu+1)} \leftarrow F(\epsilon^{(\nu+1)})$  ▷ Fixed-point iteration
10:   $\nu = \nu + 1$ 
11:  if  $\nu > n_{max}$  then ▷ Start Newton iteration if number of fixed-point iterations exceeds  $n_{max}$ 
12:     $Z \leftarrow \text{In}(q, Z)$  ▷ Increase basis size
13:     $H \leftarrow F_u Z$  ▷ Compute additional column of  $H$ 
14:     $\nu = 0$ 
15:  end if
16:  error  $\leftarrow \frac{(\|k \cdot \hat{\sigma}(k)\|^2)^{1/2}}{\|\hat{\sigma}(0)\|}$ 
17: end while
```

sponding to the stable part is retained in constructing the next iterate of the approximate solution. While marginally more computationally expensive than using a fixed-point iteration only on the stable subspace, it has the important advantage that standard existing fixed-point codes can directly be used with minimal modification as the RPM “wraps around” the fixed-point method.

4.3 A Variational Perspective

We begin with noting an analogy between the problem of interest here and the energy-minimization formulation of electrostatic fields in matter. The field equations and constitutive response of electrostatic fields in matter are respectively:

$$\text{div } \nabla \phi = \text{div } \mathbf{p} \text{ on } \Omega, \quad \mathbf{p}(\mathbf{x}) = \tilde{\mathbf{p}}(\nabla \phi(\mathbf{x}), \mathbf{x}), \quad \text{BCs: } \phi(\mathbf{x}) = V_0(\mathbf{x}) \forall \mathbf{x} \in \partial\Omega \quad (4.19)$$

where ϕ is the electric potential, \mathbf{p} is the dipole per unit volume induced by the electric field $\nabla \phi$, and $\tilde{\mathbf{p}}$ is the material-dependent response function that can be an explicit function of position. For

simplicity, we have assumed Dirichlet boundary conditions V_0 on the boundary $\partial\Omega$ of the domain Ω , but it is straightforward to use more general BCs. Note that we neglected various constants such as the permittivity of vacuum.

Under some physically-motivated conditions on $\tilde{\mathbf{p}}$, this can be reformulated as the minimization of electrostatic energy. For instance, we consider the case of a linear dielectric which is analogous to the linear elastic medium considered in this work, in which case $\tilde{\mathbf{p}}$ takes the form:

$$\tilde{\mathbf{p}}(\mathbf{E}(\mathbf{x}), \mathbf{x}) = \chi(\mathbf{x})\mathbf{E} \quad (4.20)$$

where $\chi(\mathbf{x})$ is the second-order electrical susceptibility tensor.

Following [JK90] for magnetostatics – see also [SB01] and [YD11] for electrostatics – we can write this as an energy minimization with a nonlocal constraint:

$$\min E_{electro}[\mathbf{p}, \phi], \text{ with } E_{electro}[\mathbf{p}, \phi] = \frac{1}{2} \int_{\Omega} (\mathbf{p} \cdot \chi^{-1} \mathbf{p} + |\nabla \phi|^2), \text{ subject to } \operatorname{div} \nabla \phi = \operatorname{div} \mathbf{p} \text{ on } \Omega \quad (4.21)$$

with BCs $\phi(\mathbf{x}) = V_0(\mathbf{x}) \forall \mathbf{x} \in \partial\Omega$.

From the fundamental physics of electrostatics problems, related to the motion of charges under an electric field, we have χ is positive-definite pointwise. Therefore, from an elementary application of the direct method of the calculus of variations, a unique minimizer exists; loosely, the energy is bounded below and grows quadratically in all directions from the positive-definiteness of χ . The nonlocal constraint, while somewhat nonstandard, can be readily dealt with, e.g. [JK90].

We turn now to linear inhomogeneous elasticity. We recall the balance of linear momentum:

$$\operatorname{div} \mathbf{C}(\mathbf{x}) \boldsymbol{\epsilon}_u = 0 \quad (4.22)$$

posed on the periodic unit cell V with periodic BCs. We decompose $\mathbf{C}(\mathbf{x}) = \mathbf{C}_0 + \mathbf{d}(\mathbf{x})$, where

C_0 is the homogeneous reference medium. This gives:

$$\operatorname{div} C_0 \epsilon_u = -\operatorname{div} d\epsilon_u \quad (4.23)$$

Recall from Section 4.1 that we defined the polarization field $\tau := d\epsilon_u$. Following closely the electrostatic case, we can pose this as a nonlocally-constrained critical-point problem. Define the energy E :

$$E[\tau, u] = \frac{1}{2} \int_V (\tau : d^{-1}\tau + \epsilon_u : C_0 \epsilon_u), \text{ subject to } \operatorname{div} C_0 \epsilon_u = -\operatorname{div} \tau \quad (4.24)$$

Use the variation $\tau \rightarrow \tau + \epsilon\omega$ and $u \rightarrow u + \epsilon w$:

$$\delta E = \int_V (\omega : d^{-1}\tau + \epsilon_u : C_0 \epsilon_w) \quad (4.25)$$

The variations ω and w are not independent; they are constrained to satisfy:

$$\operatorname{div} C_0 \epsilon_w = -\operatorname{div} \omega \quad (4.26)$$

On both sides of the equation above, do the following: (1) take the inner product with ϵ_u ; (2) integrate over V ; (3) use integration-by-parts to move the derivatives. The result of these operations is:

$$\int_V \epsilon_u : C_0 \epsilon_w = \int_V -\omega : \epsilon_u \quad (4.27)$$

where the boundary terms cancel out due to periodicity.

Using (4.27) in (4.25), and requiring $\delta E = 0$ for arbitrary ω , we have:

$$d^{-1}\tau - \epsilon_u = 0, \quad \operatorname{div} C_0 \epsilon_u = -\operatorname{div} \tau \quad (4.28)$$

We highlight here that the tensor $\mathbf{d}(\mathbf{x})$ is generally not positive-definite pointwise, particularly in the important case of high elastic contrasts. For instance, consider a material with voids, where the non-voided material is stable, i.e. $\mathbf{C}(\mathbf{x})$ is positive-definite in the non-voided material, and $\mathbf{C}(\mathbf{x}) = \mathbf{0}$ in the void region. The reference medium is taken to be stable, i.e. \mathbf{C}_0 is positive-definite to enable solution of the constraint equation. Then, $\mathbf{d} = -\mathbf{C}_0$ in the voids, and is not positive-definite pointwise. Therefore, in general, we do not expect existence of minimizers for E .

Loosely, the energy has unstable directions which are not bounded below. Therefore, gradient descent methods – which can be written as fixed-point methods as shown below for this energy formulation and by [Sch17] – do not converge. On the other hand, using Newton iterations along the unstable directions – once these are identified – can greatly improve convergence, which is precisely the role of the Recursive Projection Method.

4.3.1 Fixed-Point Iterations as Gradient Descent

We consider a gradient / steepest descent approach to minimizing the energy E :

$$E = \frac{1}{2} \int_{\Omega_{\#}} \left(\boldsymbol{\tau} : \mathbf{d}^{-1} \boldsymbol{\tau} + \frac{1}{2} \boldsymbol{\epsilon}_u : \mathbf{C}_0 \boldsymbol{\epsilon}_u \right), \text{ subject to } \operatorname{div} \mathbf{C}_0 \boldsymbol{\epsilon}_u = \operatorname{div} \boldsymbol{\tau} \quad (4.29)$$

The gradient direction in function space is given by $\mathbf{d}^{-1} \boldsymbol{\tau} - \boldsymbol{\epsilon}_u$, and a gradient flow in the standard L^2 norm is $\dot{\boldsymbol{\tau}} \sim \mathbf{d}^{-1} \boldsymbol{\tau} - \boldsymbol{\epsilon}_u$.

Consider an explicit update scheme where the constraint equation is also updated at each iteration. We obtain the following fixed-point algorithm:

1. given $\boldsymbol{\epsilon}_u^i$
 2. $\boldsymbol{\tau}^{i+1} = \boldsymbol{\tau}^i + a(\mathbf{d}^{-1} \boldsymbol{\tau}^i - \boldsymbol{\epsilon}_u^i)$
 3. $\operatorname{div} \mathbf{C}_0 \boldsymbol{\epsilon}_u^{i+1} = \operatorname{div} \boldsymbol{\tau}^{i+1}$
 4. loop
- (4.30)

where a is related to the fictitious timestep and mobility, and the superscript indexes the iterations. Notice that the constraint update (step 3 above) requires solution of a homogeneous periodic linear elastic problem with a given right side. This can be done very efficiently using fast Fourier transforms. Each iteration in the loop above is therefore extremely quick, but the key question is whether the algorithm converges and, if so, how many iterations it takes. Given that E may not possess minimizers, it follows that gradient descent may not converge.

The Classical FFT, summarized in [MS14], can be written in the fixed point form:

$$\begin{aligned}
& 1. \text{ given } \epsilon_u^i \\
& 2. \tau^{i+1} = d\epsilon_u^i \\
& 3. \operatorname{div} C_0 \epsilon_u^{i+1} = \operatorname{div} \tau^{i+1} \\
& 4. \text{ loop}
\end{aligned} \tag{4.31}$$

This can be considered as derived from the explicit update scheme above, except that the update for τ in step 2 goes directly to the minimum – for a given ϵ_u^i – using that the energy is quadratic. As in the explicit update scheme, this is very fast for each iteration, but whether it converges, and the rate of convergence, depend on the structure of the energy landscape.

The Polarization FFT proposed by [MB12] can be rewritten in the form:

$$\begin{aligned}
& 1. \text{ given } \epsilon_u^i \\
& 2. \tau^{i+1} = d\epsilon_u^i \\
& 3. \operatorname{div} C_0 \epsilon_u^{i+1} = \operatorname{div} C_0 d^{-1} \tau^{i+1} + \beta \operatorname{div} C_0 d^{-1} C_0 \epsilon_u^i - \operatorname{div} C_0 d^{-1} C_0 \tilde{\epsilon}_u^i \\
& \quad \text{where } \tilde{\epsilon}_u^i \text{ solves } \operatorname{div} C_0 \tilde{\epsilon}_u^i = \operatorname{div} (\alpha \tau^i + (\alpha + \beta) C_0 \epsilon_u^i) \\
& 4. \text{ loop}
\end{aligned} \tag{4.32}$$

While this form is not as transparent or convenient, it enables us to compare the methods in the context of gradient descent. We notice that in this form, the polarization method can be considered

as a relaxation method that mixes in the value from the previous iteration, with α and β being the relaxation parameters.

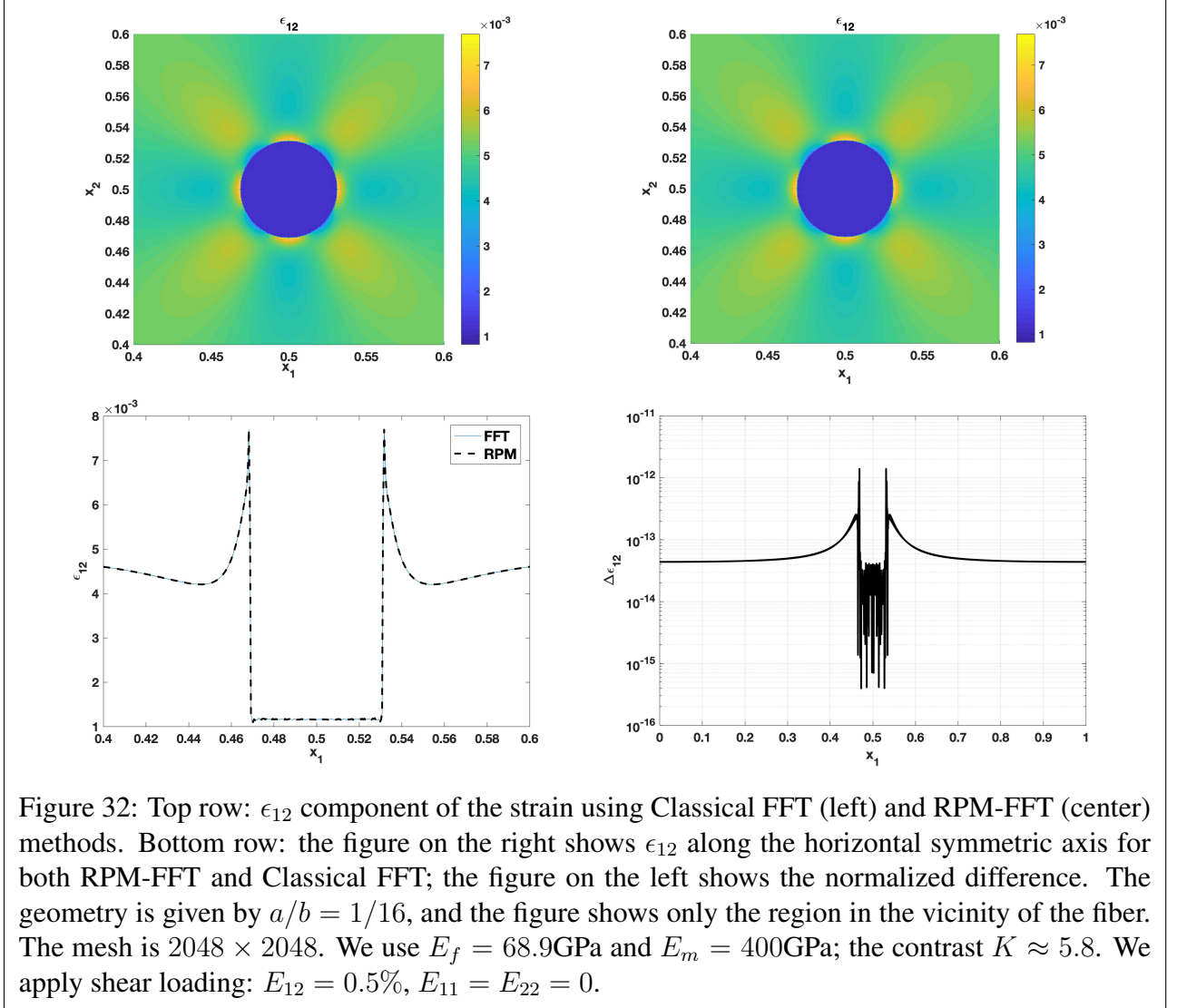
4.4 Numerical Comparisons Between Classical FFT, Accelerated FFT, and RPM-FFT

As a canonical problem for many of the calculations below, we follow [MS98] in using a circular stiff fiber embedded in a compliant matrix, at the center of a square unit cell and periodic boundary conditions (Fig. 32). This example is chosen because of the availability of approximate closed-form solutions. We use the following notation: a denotes the fiber radius; b denotes the size of the square unit cell; E_f and $\nu_f = 0.35$ denote respectively the elastic modulus and the Poisson's ratio of the fiber, noting that we assume isotropic elasticity; E_m and $\nu_m = 0.23$ denote respectively the elastic modulus and the Poisson's ratio of the matrix, again assuming isotropic elasticity; and $K = E_f/E_m$ is the elastic contrast, where particular focus will be on large values of K . The average strain is denoted by the components E_{12}, E_{11}, E_{22} . For all tests in this section except Section 5.5, the reference medium is assumed to be isotropic and we choose the elastic modulus $E_o = \frac{E_f + E_m}{2}$ and the Poisson's ratio $\nu_o = \nu_f = \nu_m$.

As a first test, we simply confirm that RPM-FFT converges to the correct solution in Fig. 32. There is no discernible difference² in the solutions obtained from the Classical FFT and RPM-FFT methods. Further, Classical FFT takes less time³ than RPM-FFT. This is unsurprising given that the elastic contrast is small ($K \approx 5.8$). As K increases, the advantages of the RPM-FFT method over the Classical FFT method become clear. We examine this and other issues below, with a more detailed reporting of computational time.

²The tolerance in all calculations reported in this work is taken to be 10^{-4} .

³All times reported in this work are wall-clock times.



4.4.1 Time to Convergence vs. Elastic Contrast

We next compare the time taken for convergence across the Classical FFT, Accelerated FFT, and RPM-FFT methods. We continue with the circular fiber in matrix setting, with K going from 10 to 10^5 , and $\nu_m = \nu_f = 0.25$. We use a 256×256 discretization, and apply an average shear strain: $E_{12} = 0.5\%$, $E_{11} = E_{22} = 0$.

Fig. 33 shows the now well-known dramatic improvement between the Classical FFT and the Accelerated FFT methods; [MMS01] show that the rate of convergence in the Classical FFT method

goes as the contrast K , while for the Accelerated FFT method the rate of convergence goes as the square root of the contrast K .

Fig. 33 also compares the Accelerated FFT method and RPM-FFT method. When the contrast is below 10^3 , the Accelerated FFT method converges faster. However, as the contrast increases, RPM-FFT is increasingly competitive, and surpasses Accelerated FFT. The rate of convergence of RPM goes as $K^{0.43}$ for this particular class of examples. The exponent appears to be roughly the same in a few other problems that we tested.

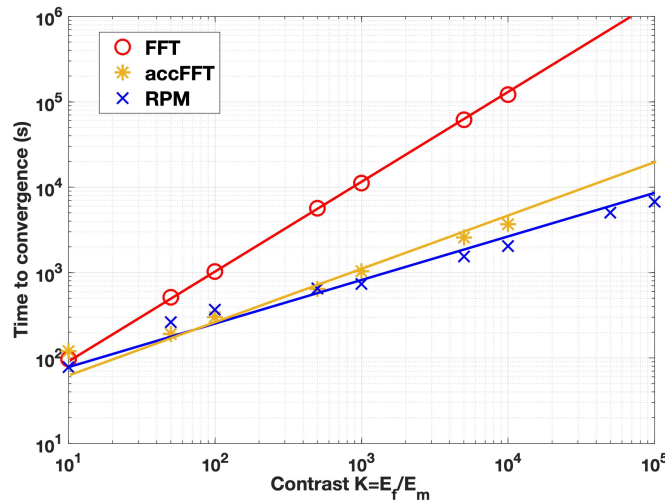


Figure 33: Time at convergence of three methods with varying K . Note the log scale. The lines are linear best fits.

We note that the comparisons for all of these methods was conducted by implementing the codes in Matlab with no additional optimization of any of the methods to ensure fair comparisons.

4.4.2 Balancing Newton Iterations against Fixed Point

As can be expected, the speed of RPM-FFT depends strongly on the size of the unstable subspace on which Newton iterations must be performed. While the Newton's method has better convergence properties, each Newton iteration is also far more expensive than the fixed point iteration, particularly as the dimension of the unstable subspace increases. On the other hand, the fixed point

method converges slowly, or not at all, on the unstable subspace, which also increases the expense as it requires a large number of iterations.

In this section, the term “unstable subspace” refers to the subspace that the RPM-FFT method identifies; this is not necessarily the true unstable subspace whose corresponding eigenvalues are outside the unit disk.

An optimal method has to balance between the opposing issues identified above. Denoting by n_{max} the number of fixed-point iterations before increasing the size of the unstable subspace, we notice that setting n_{max} too low causes the dimensionality of the unstable subspace to increase quickly and makes each Newton iteration expensive; on the other hand, if n_{max} is too high, there will be minimal progress from the large number of fixed-point iterations before switching to Newton iterations.

We examine this interplay numerically for the model problem described previously, for varying K . We first fix K , and then compare the times obtained for a large range of n_{max} going from 1 to 50. We then repeat over a range of K . Of these, we denote the value of n_{max} with the best (least) time as $n_{max}^{best}(K)$. Fig. 34 shows the times to convergence for a fixed value of $n_{max} = 10$, as well as the times to convergence for $n_{max}^{best}(K)$, as a function of K . An immediate conclusion is that there is almost no difference at low K , and not much difference at higher K .

We next compare the effect of the size of the problem on $n_{max}^{best}(K)$, for a fixed value of $K = 50$. Fig. 35 shows n_{max}^{best} for different problem sizes, here identified with the number of grid points in each direction. An immediate conclusion is that n_{max}^{best} increases with the problem size.

4.4.3 Effect of Volume Fraction and Problem Size

In the model problem of a stiff fiber in a soft matrix, the volume fraction of the stiff fiber has been taken to be small; for $a/b = 1/16$, the stiff fiber has a volume fraction $\lambda = 0.3\%$. Note that we use the term volume fraction though we are working in the 2D setting.

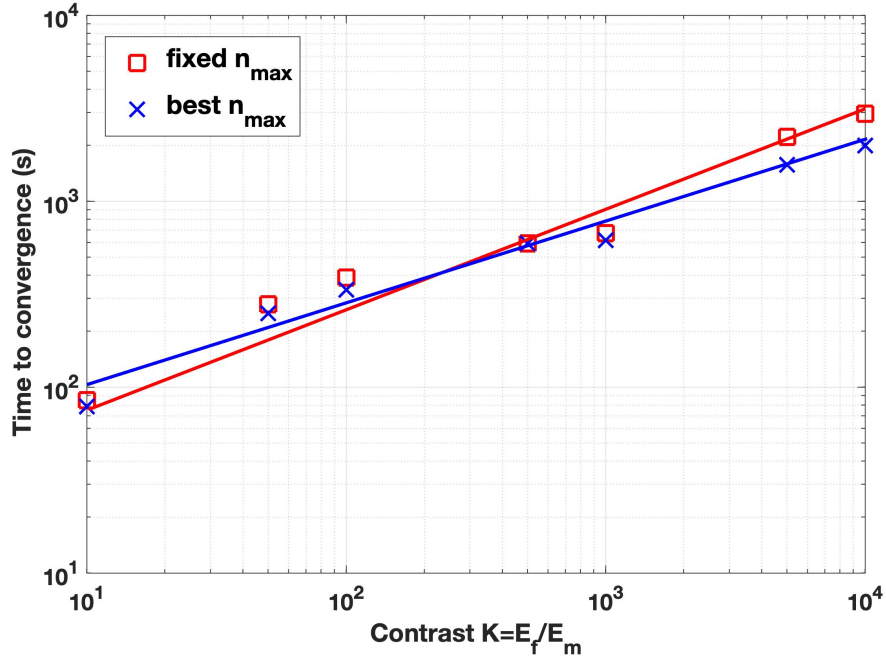


Figure 34: Time at convergence of RPM with fixed $n_{max} = 10$ and $n_{max}^{best}(K)$. The lines are linear best fits.

We expect that the size of the unstable subspace is related to the size of the fiber based on the heuristics discussed in Sections 1.3, 4.2 and 4.3. As the volume fraction increases, we therefore expect a larger unstable subspace and consequently more expensive Newton iterations.

We examine this issue through numerical experiments, and find that RPM-FFT works well even at the combination of large elastic contrast K and volume fraction of fiber λ . For instance, even with $K \approx 10^4$ or higher, and $a/b = 9/10 \Rightarrow \lambda = 63.6\%$, RPM-FFT is easily able to converge. Fig. 36 shows the time to convergence as a function of λ . While larger elastic contrasts require more time to converge – in line with our observations above – we notice that the time to converge is almost insensitive to λ for volume fractions larger than 5%.

We next consider the case of fixed λ but with changing problem size with a fixed geometry. That is, we compare discretizations of varying coarseness. The number of grid points within the fiber, as well as overall, increases as the discretization is made finer. We consequently expect the unstable subspace identified by RPM to also increase. Fig. 37 shows the relation between the size of the

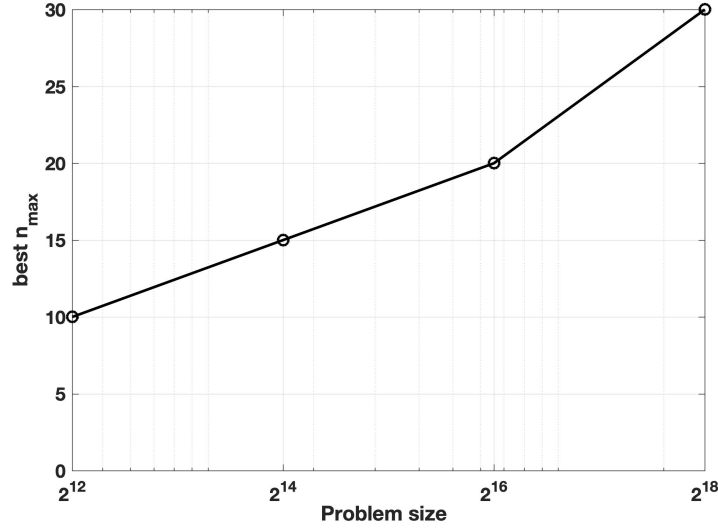


Figure 35: The best n_{\max} for different problem sizes. The line connects datapoints to aid visualization.

unstable subspace as the problem size increases from 32×32 to 512×512 , for different values of elastic contrast K . The volume fraction λ is held fixed 1.2%. Roughly, we observe a logarithmic scaling between the size of the unstable subspace and the number of grid points within the fiber.

4.4.4 Interaction Between Stiff Fibers

Motivated by recent advances in functional composites [HSP⁺19, RRWN17], we examine the setting of two circular carbon fibers embedded in a polyurethane matrix. It is a significant challenge to characterize the effective properties of heterogeneous materials such as nanofiber- and nanoparticle-reinforced nanocomposites starting from the scale of resolving the entire microstructure. This makes it challenging to develop physics-based high-fidelity model that predict the performance of such nanocomposite systems. The FFT methods can help to make stronger direct connections between mechanics modeling and experimental data, which in turn can have a significant impact on understanding the structure-property relations of these complex heterogeneous nanocomposite systems.

We consider the geometry of Fig. 38 with two fibers that are either close to each other – the

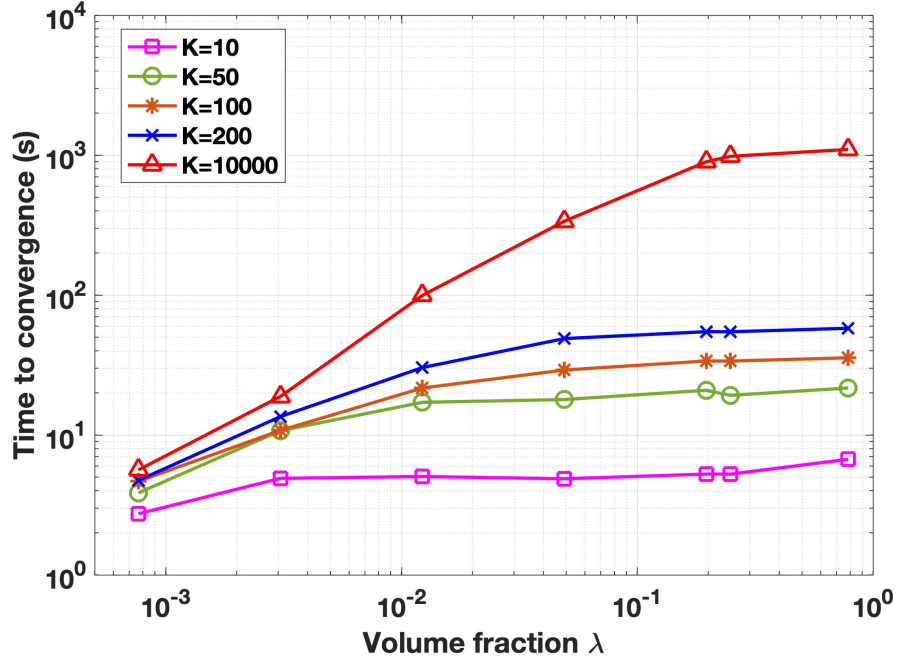


Figure 36: Time to convergence of RPM-FFT with varying λ and K . The lines connect the datapoints to aid visualization.

separation is smaller than the smaller fiber diameter – and when they are further apart. The moduli are assumed to be $E_f = 900$ GPa for the carbon fiber and $E_m = 0.03$ GPa for the polyurethane, giving an elastic contrast of $K = 3 \times 10^4$. Two fibers, radius a and $2a$, are located in a rectangular unit cell of size $2b \times b$, with $b = 10a$. We examine two cases: when the fibers are far apart with distance b between the centers of the fibers, and when the fibers are closer with distance $0.4b$, see Fig. 38. We apply a uniaxial average strain: $E_{11} = 5\%$, $E_{22} = E_{12} = 0$.

Fig. 38 shows strain and strain energy density fields for the two configurations. In all of these configurations, the strain and strain energy density fields are essentially 0 within the stiff fibers, and also show good convergence properties with no obvious spurious oscillations near the transition from matrix to fiber. We notice that in the case where the fibers are further apart, the energy density and strain fields suggest that the fibers can be essentially considered dilute and non-interacting. However, when the fibers are closer together – as is typical of experimental specimens [HSP⁺19, RRWN17] – there is a clear interaction between the fields, and the energy density and strain fields take their largest values in the region between the fibers.

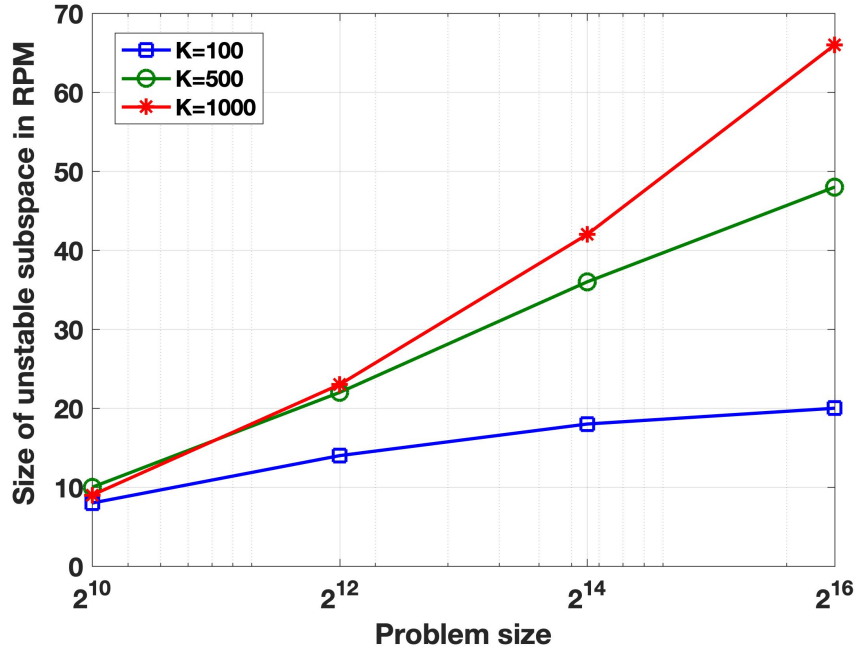
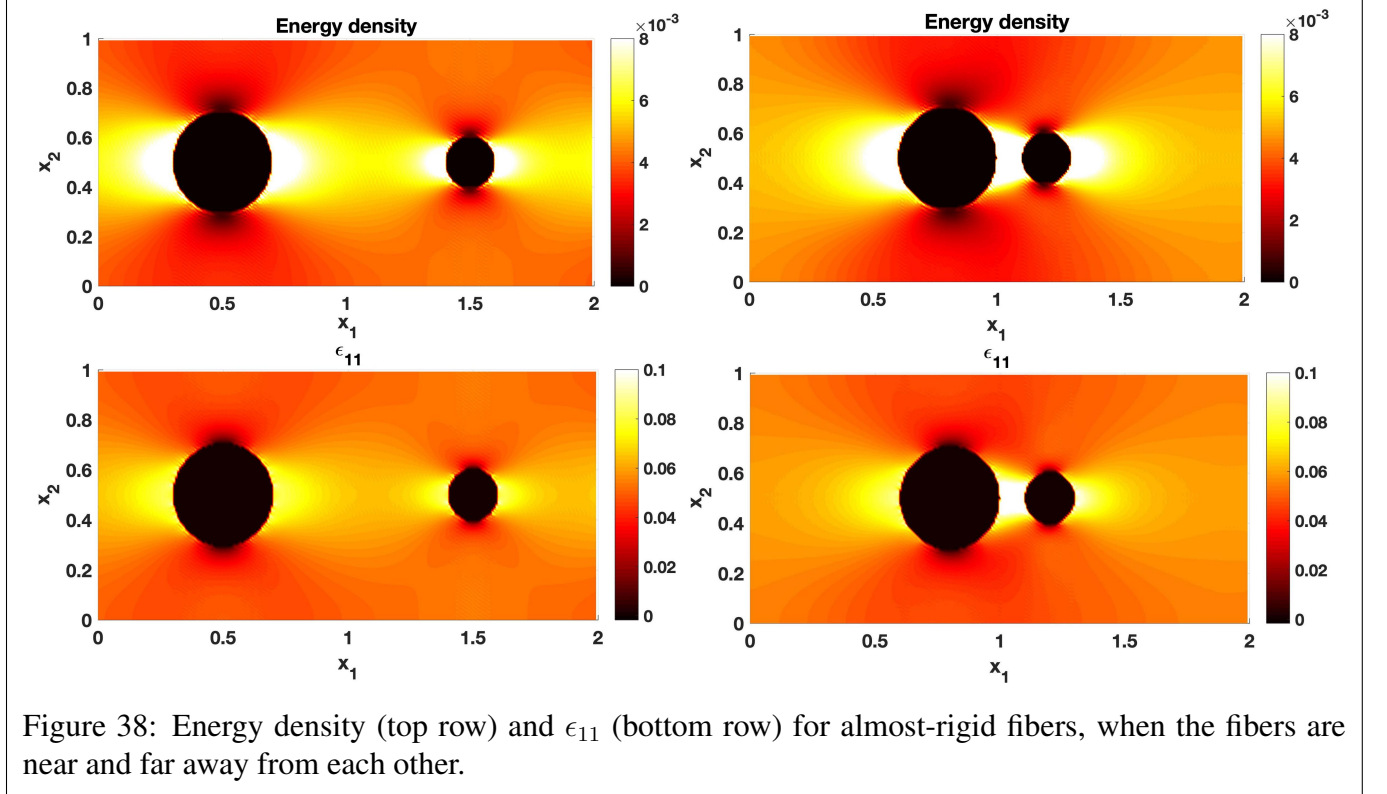


Figure 37: Size of unstable subspace with problem size. The lines connect the datapoints to aid visualization.

4.4.5 RPM Applied to the Accelerated FFT Method

Two important advantages of the RPM approach are, first, that it uses the fixed-point iterations to identify the unstable subspace; and, second, once identified, it performs Newton iterations on the unstable subspace with fixed-point iterations on the *entire* space. This makes it easy to apply the RPM strategy to existing fixed-point methods with minimal changes to algorithm / code. We therefore exploit this to apply the RPM approach to the Accelerated FFT method which is also based on a fixed-point framework. Given that the Accelerated FFT method has much superior performance compared to the Classical FFT method, we might expect that a RPM-Accelerated FFT method likely performs even better. We examine this issue below.

In [MS14], it is shown that the Accelerated FFT method is a special case of the general polarization-based fixed-point method developed by [MB12]. Algorithm 5 is the general polarization-based method, where α and β can take any value within a range. For the choice $\alpha = \beta = 2$, the polarization-based method reduces to the Accelerated FFT method. In [MS14], they also discuss



and compare the Accelerated FFT method with other polarization-based methods, corresponding to the choices $\alpha = \beta = 1.5$ and $\alpha = \beta = 1$.

All of these methods are fixed-point based methods, and therefore require that the eigenvalues of the Jacobian are within the unit disk for convergence. The Accelerated FFT method has the lowest upper bound [MS14], and we therefore combine this with the RPM method.

In all of these methods, an important part of the method is the additive decomposition of the heterogeneous stiffness into a homogeneous reference medium and a fluctuation; see Section 4.3. The convergence rate is typically very sensitive to the choice of reference medium.

It has been observed that the choice of the reference medium affects the rate of convergence in many fixed-point based schemes. In the classical FFT method [MS98], the best choice was found to be the average of the supremum and infimum of the elastic moduli. In Accelerated FFT [MMS01] and Polarization FFT [MB12] the optimum is shown to be $E_o/E_f = \sqrt{K}$ when computing with a

K	Number of Iterations		Time (seconds)	
	Acc-FFT	RPM-Acc-FFT	Acc-FFT	RPM-Acc-FFT
500	234	83	6.46	4.47
1000	335	81	8.51	4.42
5000	335	81	20.24	4.40
10000	1136	82	28.29	4.44
50000	2741	82	68.56	4.45
100000	3863	161	98.60	11.13

Table 4: Number of iterations and time to convergence for the Accelerated-FFT and RPM-Accelerated-FFT for a wide range of K .

very high precision (10^{-10}).

However, as also discussed in Section 4.3, we expect the RPM-based approach to be insensitive to this choice. Therefore, we apply the RPM approach to the Accelerated FFT method, which is readily obtained by simply replacing the fixed-point operation in algorithm 4 with the iteration procedure in algorithm 5.

Algorithm 5 Polarization-FFT algorithm

- 1: **Iteration** $i + 1$ (given ϵ^i)
 - 2: $\sigma^i \leftarrow C(x) : \epsilon^i$
 - 3: $s_a^i = \sigma^i + (1 - \beta)C^0 : \epsilon^i$
 - 4: $s_b^i = \alpha\sigma^i + \beta C^0 : \epsilon^i$
 - 5: $\hat{s}_b^i \leftarrow \mathcal{F}[s_b^i]$
 - 6: $\hat{\epsilon}_b^i \leftarrow -\hat{I}^0 : \hat{s}_b^i \quad \forall k \neq 0 \text{ and } \hat{\epsilon}_b(0)^i = \beta E$
 - 7: $\epsilon_b^i \leftarrow \mathcal{F}^{-1}[\hat{\epsilon}_b^i]$
 - 8: $\epsilon^{i+1} = (C(x) + C^0)^{-1} : (s_a^i + C^0 : \epsilon_b^i)$
-

Table 4 compares the number of iterations and the time for Accelerated FFT and RPM-Accelerated FFT for a wide range of contrasts. The enhancement provided by RPM is increasingly large as the elastic contrast K increases.

We next examine the sensitivity to the choice of reference medium for Accelerated FFT and RPM-Accelerated FFT. Fig. 39 compares the time to convergence and number of iterations – for a wide range of K – for the usual Accelerated FFT method against the RPM-Accelerated FFT method, for various choices of reference medium.

When K is small, the performance of the Accelerated FFT follows what has been observed in [MS14]: namely, the best choice is at when $E_o/E_f = \sqrt{K}$. But this is not the case for $K = 10^3, 10^4$. Meanwhile, RPM-Accelerated FFT is much less affected by the different choices of the reference over all of the K s being tested. As pointed out in [MS14], the $E_o/E_f = \sqrt{K}$ choice is valid when the precision is high (10^{-10}), which explains Fig. 39 (e,f,g,h), as all tests here are computed with 10^{-4} precision which is more in line with standard practice.

We notice, particularly at high contrast, that the use of RPM in conjunction with Accelerated FFT makes the method much more robust with regard to the choice of reference medium.

4.5 Conclusions

We have applied RPM [SK93] to the problem of determining the stress and strain in the unit cell of a periodic linear elastic material. Existing methods for this problem, e.g. Classical FFT [MS98] and Accelerated FFT [MMS01] methods, are fixed-point methods, and can have difficulty converging when the eigenvalues of the Jacobian lie outside the unit disk. While Newton methods can recover the convergence, they are very expensive on the high-dimensional problems of interest. RPM [SK93] provides an elegant and efficient balance between fixed-point and Newton methods: it uses the fixed-point iterations to adaptively identify the unstable subspace that requires Newton, and performs Newton only on that subspace. Fixed-point iterations can be performed on the complementary stable subspace. For practical reasons of not changing existing algorithms and code, fixed-point is performed on the entire space, but is then projected to the complementary stable subspace.

A variational perspective, using analogies from electromagnetism, provides insight into the reason that the RPM decomposition can work well. In particular, we expect that there are flat or unstable directions in the energy landscape in the context of certain formulations of heterogeneous linear elasticity, particularly when the stiffness tensor can vanish, as in the case of voids in materials. The RPM-FFT method proposed in this work exploits this structure to perform Newton iterations in

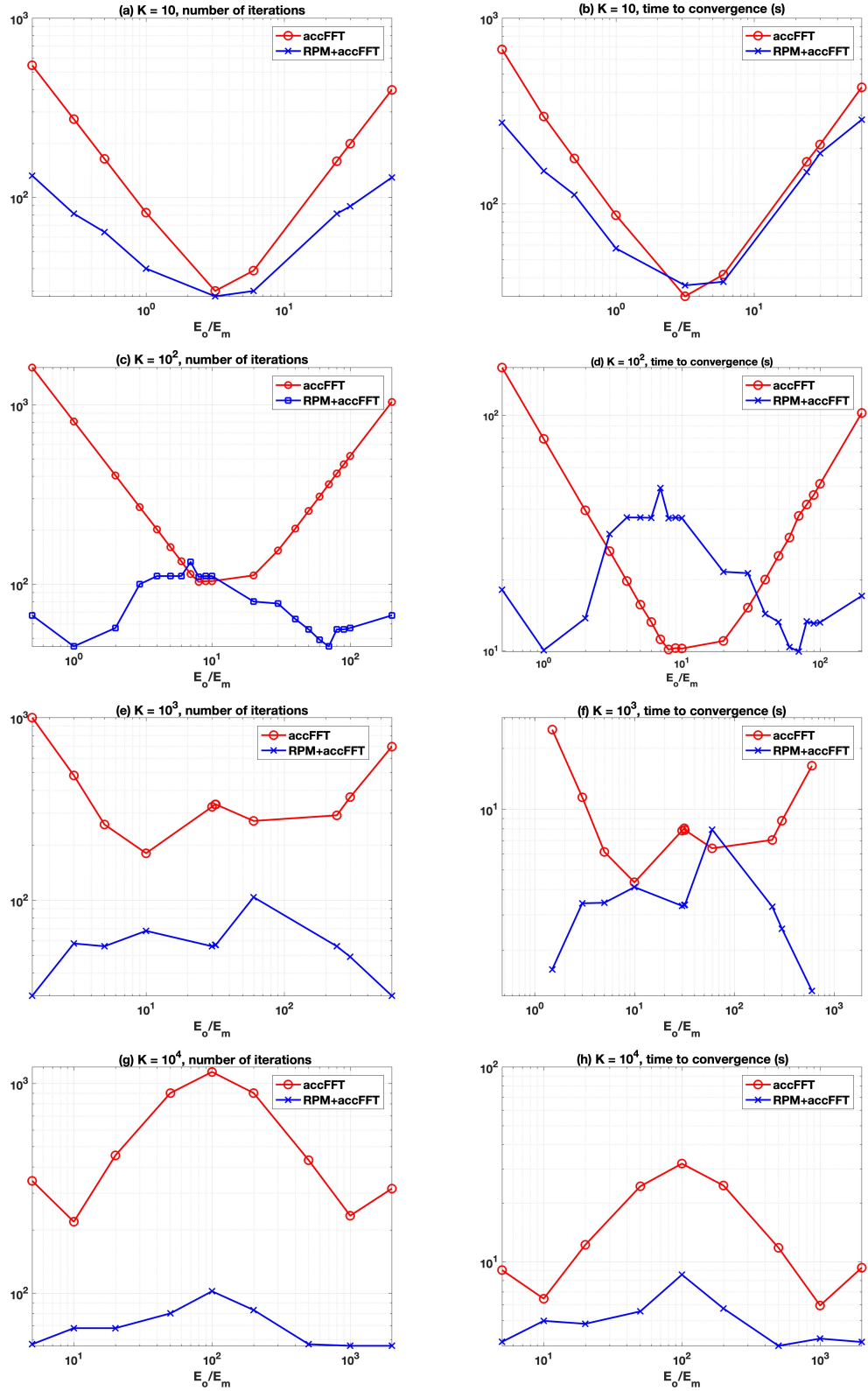


Figure 39: Number of iterations and times to convergence as a function of reference medium modulus E_o . We examine $K = 10, 10^2, 10^3, 10^4$ in the first, second, third and fourth rows respectively.

directions along which the fixed-point would be unstable.

Our results show that the RPM-FFT is more efficient than the fixed-point methods as the contrast is increased. Further, all of the fixed-point methods mentioned above require the use of a homogeneous reference medium as an important part of the method, but there is typically no systematic approach to selecting the reference medium. We see that while the fixed-point methods can be sensitive to the choice of reference medium, the RPM-FFT method is extremely robust in terms of convergence for a wide range of choices for the reference medium.

We also note the feature of RPM that it can be easily used to “wrap-around” any fixed-point algorithm. Consequently, while we have used it here for two specific instances of FFT-based methods, it can be easily combined with other formulations if they are found to be more efficient.

While we have applied RPM-FFT to the context of mechanical response, our overall approach is applicable to numerous linear problems with the same structure in homogenization [Mil02]. Further, while we have not examined nonlinear problems here, it is relatively straightforward to do this. Briefly, most methods for nonlinear problems using the FFT consist of the repeated use of linear solves [LR20], and the method presented can readily the other approaches in a modular way.

Finally, we note that while we have used Newton iterations for the space that is unstable under fixed-point iterations, it is possible to replace or combine Newton iterations with a conjugate gradient or other solver that could provide better performance [VZM14, GMC13, KBS14]. Potential improvement can be achieved by combining the model order reduction techniques for FFT solvers as proposed in [KMG⁺19] with RPM. This provides a direction for future exploration. In this context, we particularly highlight the recent interesting approach proposed in [Sch17], where a different variational principle is shown to provide promising results.

5 Summary

In Section 2, 3D isotropic grain growth simulations were performed with experimental microstructures. Comparisons between the simulated and the experimental microstructures show that the isotropic model cannot capture the grain growth on the grain-to-grain basis. Possible reasons are studied and motivate the use of anisotropic model. For the future work on this topic, the isotropic TD formulation will be extended to include anisotropy using anisotropic surface energy and mobility from experiment. References to anisotropic TD scheme with arbitrary surface and mobility data can be found in [EJZ17]. By comparisons between simulations with the isotropic TD scheme and anisotropic TD schemes, different forms of anisotropic kernels can be tested and give insights about how the boundary properties affect grain boundary evolution.

In Section 3.1, PFDD is extended to BCC metals. Tests designed to show this new capability are performed and compared to Molecular Statics simulations. Ultimately, dislocation dynamics in BCC metals are rate dependent, giving rise to a macroscopic deformation response that is highly sensitive to the applied strain rate and temperature. With the mechanistic model in place in the present framework, it is now possible to incorporate temperature and rate effects on dislocation motion. With such additions, this model could model both nucleation and propagation of kink-pairs for example. Such topics are interesting extensions for future work. A new kind of computational grids – non-orthogonal grids are constructed and applied in Section 3.2. Non-orthogonal grids outperform other grids used previously, and reproduce the correct physical behaviors with systems of multiple non-coplanar planes.

Section 2 and Section 3 focus on modeling grain boundary and dislocation respectively. Different models are used but share similarities in the formulations. Multiple phases are prescribed with order parameters, which represent different grains in polycrystals and different slip systems of the dislocations. The phase boundaries are evolved and tracked implicitly, corresponding to grain boundaries and dislocations respectively.

Original FFT method is used in the PFDD formulation and motivates the study of the non-orthogonal grids in Section 3.2. RPM-FFT in Section 4 is an adapted FFT method that recovers the convergence for heterogeneous materials with high contrast elastic properties. It can be a useful tool for PFDD when it comes to modeling such materials. While RPM-FFT uses Newton iterations for the space that is unstable under fixed-point iterations, it is possible to replace or combine Newton iterations with a conjugate gradient or other solver that could provide better performance [VZM14,GMC13,KBS14]. Potential improvement can be achieved by combining the model order reduction techniques for FFT solvers as proposed in [KMG⁺19] with RPM. This provides a direction for future exploration.

References

- [ACT⁺07] A. Arsenlis, W. Cai, M. Tang, M. Rhee, T. Oppelstrup, G. Hommes, T. G. Pierce, and V. V. Bulatov. Enabling strain hardening simulations with dislocation dynamics. *Modelling and Simulation in Materials Science and Engineering*, 15:553–595, 2007.
- [AP13] M. Agoras and P. Ponte Castañeda. Iterated linear comparison bounds for viscoplastic porous materials with “ellipsoidal” microstructures. *Journal of the Mechanics and Physics of Solids*, 61(3):701–725, 2013.
- [AT06] G J Ackland and R Thetford. An improved N -body semi-empirical model for body-centred cubic transition metals. *Phil. Mag. A*, 8610, 2006.
- [Atk88] HV Atkinson. Overview no. 65: Theories of normal grain growth in pure single phase systems. *Acta Metallurgica*, 36(3):469–491, 1988.
- [BC06] V. V. Bulatov and W. Cai. *Computer Simulations of Dislocations*. Oxford University Press, Great Britain, 2006.
- [BH67] J. F. Byron and D. Hull. Plastic deformation of tantalum single crystals. i. the surface morphology of yield. *Journal of Less-Common Metals*, 13:71–84, 1967.
- [BH16a] I J Beyerlein and A Hunter. Understanding nanoscale dislocation mechanics using phase field dislocation dynamics. *Philos. Trans. R. Soc. A*, 374(2066):20150166, 2016.
- [BH16b] IJ Beyerlein and A Hunter. Understanding dislocation mechanics at the mesoscale using phase field dislocation dynamics. *Philosophical Transactions of the Royal Society A: Mathematical, Physical and Engineering Sciences*, 374(2066):20150166, 2016.

- [BN47] William Lawrence Bragg and JF Nye. A dynamical model of a crystal structure. *Proceedings of the Royal Society of London. Series A. Mathematical and Physical Sciences*, 190(1023):474–481, 1947.
- [BSH⁺19] Aditi Bhattacharya, Yu-Feng Shen, Christopher M Hefferan, Shiu Fai Li, Jonathan Lind, Robert M Suter, and Gregory S Rohrer. Three-dimensional observations of grain volume changes during annealing of polycrystalline ni. *Acta Materialia*, 167:40–50, 2019.
- [BT52] JE Burke and D Turnbull. Recrystallization and grain growth. *Progress in metal physics*, 3:220–292, 1952.
- [BTB⁺14] N. Bertin, C. N. Tomé, I. J. Beyerlein, M. R. Barnett, and L. Capolungo. On the strength of dislocation interactions and their effect on latent hardening in pure magnesium. *International Journal of Plasticity*, 62:72–92, 2014.
- [BUPC15] Nicolas Bertin, MV Upadhyay, C Pradalier, and L Capolungo. A fft-based formulation for efficient mechanical fields computation in isotropic and anisotropic periodic discrete dislocation dynamics. *Modelling and Simulation in Materials Science and Engineering*, 23(6):065009, 2015.
- [CB04] W. Cai and V. V. Bulatov. Mobility laws in dislocation dynamics simulations. *Materials Science and Engineering A*, 387-389:277–281, 2004.
- [CHBK15] L. Cao, A. Hunter, I. J. Beyerlein, and M. Koslowski. The role of partial mediated slip during quasi-static deformation of 3d nanocrystalline metals. *J. Mech. Phys. Solids*, 78:415–426, 2015.
- [Che02] Long-Qing Chen. Phase-field models for microstructure evolution. *Annual review of materials research*, 32(1):113–140, 2002.
- [Cia88] Philippe G Ciarlet. *Three-dimensional elasticity*, volume 20. Elsevier, 1988.

- [CS13] HZ Chen and YC Shu. Phase-field modeling of martensitic microstructure with inhomogeneous elasticity. *Journal of Applied Physics*, 113(12):123506, 2013.
- [DK97] B. Devincre and L. P. Kubin. Mesoscopic simulations of dislocations and plasticity. *Materials Science and Engineering A*, 8:14, 1997.
- [DMO99] W Dreyer, WH Müller, and J Olschewski. An approximate analytical 2d-solution for the stresses and strains in eigenstrained cubic materials. *Acta mechanica*, 136(3):171–192, 1999.
- [DV98] M.S. Duesbery and V. Vitek. Plastic anisotropy in b.c.c. transition metals. *Acta Materialia*, 46(5):1481 – 1492, 1998.
- [EABG08] J. A. El-Awady, S. B. Biner, and N. M. Ghoniem. A self-consistent boundary element, parametric dislocation dynamics formulation of plastic flow in finite volumes. *Journal of the Mechanics and Physics of Solids*, 56(5):2019–2035, 2008.
- [EAFH16] J. A. El-Awady, H. Fan, and A. M. Hussein. Advances in discrete dislocation dynamics modeling of size-affected plasticity. In C. Weinberger and G. Tucker, editors, *Multiscale Materials Modeling for Nanomechanics*, *Springer Series in Materials Science*, volume 245. Springer, 2016.
- [EE18] Matt Elsey and Selim Esedoğlu. Threshold dynamics for anisotropic surface energies. *Mathematics of Computation*, 87(312):1721–1756, 2018.
- [EJZ17] Selim Esedoğlu, Matt Jacobs, and Pengbo Zhang. Kernels with prescribed surface tension & mobility for threshold dynamics schemes. *Journal of Computational Physics*, 337:62–83, 2017.
- [EM99] DJ Eyre and GW Milton. A fast numerical scheme for computing the response of composites using grid refinement. *The European Physical Journal-Applied Physics*, 6(1):41–47, 1999.

- [EO15] Selim Esedoğlu and Felix Otto. Threshold dynamics for networks with arbitrary surface tensions. *Communications on pure and applied mathematics*, 68(5):808–864, 2015.
- [Esh59] John Douglas Eshelby. The elastic field outside an ellipsoidal inclusion. *Proceedings of the Royal Society of London. Series A. Mathematical and Physical Sciences*, 252(1271):561–569, 1959.
- [GFMH15] S. Gao, M. Fivel, A. Ma, and A. Hartmaier. Influence of misfit stresses on dislocation glide in single crystal superalloys: a three-dimensional discrete dislocation dynamics study. *J. Mech. Phys. Solids*, 76:276, 2015.
- [GMC13] Lionel Gélébart and Romain Mondon-Cancel. Non-linear extension of fft-based methods accelerated by conjugate gradients to evaluate the mechanical behavior of composite materials. *Computational Materials Science*, 77:430–439, 2013.
- [GMS⁺01] G Gottstein, DA Molodov, LS Shvindlerman, DJ Srolovitz, and M Winning. Grain boundary migration: misorientation dependence. *Current opinion in solid state and materials science*, 5(1):9–14, 2001.
- [GRL16] JT Graham, AD Rollett, and R LeSar. Fast fourier transform discrete dislocation dynamics. *Modelling and Simulation in Materials Science and Engineering*, 24(8):085005, 2016.
- [GS09] Gunter Gottstein and Lasar S Shvindlerman. *Grain boundary migration in metals: thermodynamics, kinetics, applications*. CRC press, 2009.
- [GTS00] N. M. Ghoniem, S. H. Tong, and L. Z. Sun. Parametric dislocation dynamics: A thermodynamics-based approach to investigations of mesoscopic plastic deformation. *Physical Review B*, 61(2):913–927, 2000.
- [HB01] D. Hull and D.J. Bacon. *Introduction to dislocations*. Elsevier Butterworth-Heinemann, Oxford, 2001.

- [HB14a] A. Hunter and I. J. Beyerlein. Predictions of an alternative pathway for grain-boundary driven twinning. *Applied Physics Letters*, 104(233112):1–4, 2014.
- [HB14b] A. Hunter and I. J. Beyerlein. Stacking fault emission from grain boundaries: Material dependencies and grain size effects. *Materials Science and Engineering A*, 600:200–210, 2014.
- [HB15] A. Hunter and I. J. Beyerlein. Relationship between monolayer stacking faults and twins in nanocrystals. *Acta Materialia*, 88:207–217, 2015.
- [HBGK11] A. Hunter, I. J. Beyerlein, T. C. Germann, and M. Koslowski. Influence of the stacking fault energy surface on partial dislocations in fcc metals with a three-dimensional phase field model. *Phys. Rev. B*, 84(144108):1–10, 2011.
- [Hef12] Christopher M Hefferan. *Measurement of annealing phenomena in high purity metals with near-field high energy x-ray diffraction microscopy*. PhD thesis, Carnegie Mellon University, 2012.
- [HG91] Hanfried W Hesselbarth and IR Göbel. Simulation of recrystallization by cellular automata. *Acta Metallurgica et Materialia*, 39(9):2135–2143, 1991.
- [HH79] Edwin Hewitt and Robert E Hewitt. The gibbs-wilbraham phenomenon: an episode in fourier analysis. *Archive for history of Exact Sciences*, 21(2):129–160, 1979.
- [Hir15] Pierre Hirel. AtomsK: A tool for manipulating and converting atomic data files. *Computer Physics Communications*, 197:212 – 219, 2015.
- [HL68] J. P. Hirth and J. Lothe. *Theory of Dislocations*. McGraw-Hill, New York, 1968.
- [HLB18] A. Hunter, B. Leu, and I. J. Beyerlein. A review of slip transfer: applications of mesoscale techniques. *J. Mater. Sci.*, 53:5584–5603, 2018.

- [HLLS10] CM Hefferan, SF Li, J Lind, and RM Suter. Tests of microstructure reconstruction by forward modeling of high energy x-ray diffraction microscopy data. *Powder Diffraction*, 25(2):132–137, 2010.
- [HRU⁺17] A. M. Hussein, S. I. Rao, M. D. Uchic, T. A. Parthasarathy, and J. A. El-Awady. The strength and dislocation microstructure evolution in superalloy microcrystals. *J. Mech. Phys. Solids*, 99:146, 2017.
- [HSP⁺19] Spencer A. Hawkins, Ali Sarvestani, Xiaoyao Peng, Evan Sullivan, Evan Mungall, Kaushik Dayal, and Dhriti Nepal. In situ visualization of nanoscale damage and strain induced crystallization in polyurethane via atomic force microscopy. *submitted*, 2019.
- [Hum00] FJ Humphreys. Modelling microstructural evolution during annealing. *Modelling and Simulation in Materials Science and Engineering*, 8(6):893, 2000.
- [HZB14] A. Hunter, R. F. Zhang, and I. J. Beyerlein. The core structure of dislocation and their relationship to the material γ -surface. *Journal of Applied Physics*, 115:134314, 2014.
- [HZT12] M. Huang, L. Zhao, and J. Tong. Discrete dislocation dynamics modelling of mechanical deformation of nickel-based single crystal superalloys. *Inter. J. Plas.*, 28:141–158, 2012.
- [JD97] B. Joós and M. S. Duesbery. The peierls stress of dislocations: An analytic formula. *Phys. Rev. Lett.*, 78(2):266–269, 1997.
- [JK90] Richard D James and David Kinderlehrer. Frustration in ferromagnetic materials. *Continuum Mechanics and Thermodynamics*, 2(3):215–239, 1990.
- [KBC12] K. Kang, V. V. Bulatov, and W. Cai. Singular orientations and faceted motion of dislocations in body-centered cubic crystals. *Proceedings of the National Academy of Sciences*, 109(38):15174–15178, 2012.

- [KBS14] Matthias Kabel, Thomas Böhlke, and Matti Schneider. Efficient fixed point and newton–krylov solvers for fft-based homogenization of elasticity at large deformations. *Computational Mechanics*, 54(6):1497–1514, 2014.
- [KCC⁺92] L. P. Kubin, G. Canova, M. Condat, B. Devincre, V. Pontikis, and Yves Bréchet. Dislocation microstructures and plastic flow: A 3d simulation. In *Non Linear Phenomena in Materials Science II*, volume 23 of *Solid State Phenomena*, pages 455–472. Trans Tech Publications, 1 1992.
- [KCO02] M. Koslowski, A. M. Cuitiño, and M. Ortiz. A phase-field theory of dislocation dynamics, strain hardening and hysteresis in ductile single crystals. *Journal of the Mechanics and Physics of Solids*, 50(12):2597–2635, 2002.
- [KDT98] L. P. Kubin, B. Devincre, and M. Tang. Mesoscopic modelling and simulation of plasticity in fcc and bcc crystals: Dislocation intersection and mobility. *Journal of Computer-Aided Materials Design*, 5:31–54, 1998.
- [KM03] U. F. Kocks and H. Mecking. Physics and phenomenology of strain hardening: the fcc case. *Progress in Material Sciences*, 48(3):171–273, 2003.
- [KMG⁺19] Julian Kochmann, Kiran Manjunatha, Christian Gierden, Stephan Wulfinhoff, Bob Svendsen, and Stefanie Reese. A simple and flexible model order reduction method for fft-based homogenization problems using a sparse sampling technique. *Computer Methods in Applied Mechanics and Engineering*, 347:622–638, 2019.
- [KS12] Reza Darvishi Kamachali and Ingo Steinbach. 3-d phase-field simulation of grain growth: topological analysis versus mean-field approximations. *Acta Materialia*, 60(6-7):2719–2728, 2012.
- [KWLL11] M. Koslowski, D. Wook Lee, and L. Lei. Role of grain boundary energetics on the maximum strength of nano crystalline nickel. *Journal of the Mechanics and Physics of Solids*, 59:1427–1436, 2011.

- [LBW18] H. Lim, C. C. Battaile, and C. R. Weinberger. Simulating dislocation plasticity in bcc metals by integrating fundamental concepts with macroscale models. In M. F. Horstemeyer, editor, *Integrated Computational Materials Engineering (ICME) for Metals: Concepts and Case Studies*, chapter 4, pages 71–106. John Wiley & Sons, 2018.
- [Leb01] Ricardo A Lebensohn. N-site modeling of a 3d viscoplastic polycrystal using fast fourier transform. *Acta materialia*, 49(14):2723–2737, 2001.
- [LeS13] R. LeSar. *Introduction to Computational Materials Science Fundamentals to Applications*. Cambridge University Press, United Kingdom, 2013.
- [Li11] Shiu Fai Frankie Li. *Imaging of orientation and geometry in microstructures: development and applications of high energy x-ray diffraction microscopy*. PhD thesis, figshare, 2011.
- [Lip93] Robert Lipton. Inequalities for electric and elastic polarization tensors with applications to random composites. *Journal of the Mechanics and Physics of Solids*, 41(5):809–833, 1993.
- [LK79] F. Louchet and L. P. Kubin. In situ deformation of b.c.c. crystals at low temperatures in a high-voltage electron microscope: Dislocation mechanisms and strain-rate equation. *Phil. Mag. A*, 39:433–454, 1979.
- [LMK13] L. Lei, J. L. Marian, and M. Koslowski. Phase-field modeling of defect nucleation and propagation in domains with material inhomogeneities. *Model. Simul. Mater. Sci. Eng.*, 21(025009):1–15, 2013.
- [LR20] Ricardo A Lebensohn and Anthony D Rollett. Spectral methods for full-field micromechanical modelling of polycrystalline materials. *Computational Materials Science*, 173:109336, 2020.

- [LT62] J. R. Low and A. M. Turkalo. Slip band structure and dislocation multiplication in silicon-iron crystals. *Acta Metallurgica*, 10:215–227, 1962.
- [LTBL17] M. A. Louchez, L. Thuinet, R. Besson, and A. Legris. Microscopic phase-field modeling of hcp/fcc interfaces. *Comp. Mater. Sci.*, 132:62–73, 2017.
- [Mad16] Siddharth Maddali. *Computational mining of meso-scale physics from high-energy X-ray data sets*. PhD thesis, figshare, 2016.
- [MB12] Vincent Monchiet and Guy Bonnet. A polarization-based fft iterative scheme for computing the effective properties of elastic composites with arbitrary contrast. *International Journal for Numerical Methods in Engineering*, 89(11):1419–1436, 2012.
- [MBO92] Barry Merriman, James Kenyard Bence, and Stanley Osher. *Diffusion generated motion by mean curvature*. Department of Mathematics, University of California, Los Angeles, 1992.
- [MDK04] G. Monnet, B. Devincere, and L. P. Kubin. Dislocation study of prismatic slip systems and their interactions in hexagonal close packed metals: application to zirconium. *Acta Materialia*, 52:4317–4328, 2004.
- [Mil02] Graeme W Milton. The theory of composites. *The Theory of Composites*, by Graeme W. Milton, pp. 748. ISBN 0521781256. Cambridge, UK: Cambridge University Press, May 2002., page 748, 2002.
- [MKO11] H. Mori, H. Kimizuka, and S. Ogata. Microscopic phase-field modeling of edge and screw dislocation core structures and peierls stresses of bcc iron. *J. Japan Inst. Metals*, 75(2):104–109, 2011.
- [MMS99] JC Michel, H Moulinec, and P Suquet. Effective properties of composite materials with periodic microstructure: a computational approach. *Computer methods in applied mechanics and engineering*, 172(1-4):109–143, 1999.

- [MMS01] JC Michel, H Moulinec, and P Suquet. A computational scheme for linear and non-linear composites with arbitrary phase contrast. *International Journal for Numerical Methods in Engineering*, 52(1-2):139–160, 2001.
- [MS94] Herve Moulinec and Pierre Suquet. A fast numerical method for computing the linear and nonlinear mechanical properties of composites. *Comptes rendus de l’Académie des sciences. Série II, Mécanique, physique, chimie, astronomie*, 318(11):1417–1423, 1994.
- [MS98] H Moulinec and P Suquet. A numerical method for computing the overall response of nonlinear composites with complex microstructure. *Computer methods in applied mechanics and engineering*, 157(1-2):69–94, 1998.
- [MS14] Hervé Moulinec and Fabrice Silva. Comparison of three accelerated fft-based schemes for computing the mechanical response of composite materials. *International Journal for Numerical Methods in Engineering*, 97(13):960–985, 2014.
- [MS15] Jaber Rezaei Mianroodi and Bob Svendsen. Atomistically determined phase-field modeling of dislocation dissociation, stacking fault formation, dislocation slip, and reactions in fcc systems. *Journal of the Mechanics and Physics of Solids*, 77:109–122, 2015.
- [Mur87] Toshio Mura. General theory of eigenstrains. In *Micromechanics of defects in solids*, pages 1–73. Springer, 1987.
- [Pei40] R. Peierls. The size of a dislocation. *Proceedings of the Physical Society*, 52(1):24–37, 1940.
- [PL13] Marcel Porta and Turab Lookman. Heterogeneity and phase transformation in materials: Energy minimization, iterative methods and geometric nonlinearity. *Acta Materialia*, 61(14):5311–5340, 2013.

- [Pliov] S. Plimpton. Fast parallel algorithms for short-range molecular dynamics. *Journal of Computational Physics*, 117:1–19, 1995; Also see <http://lammps.sandia.gov/>.
- [PMB⁺20a] Xiaoyao Peng, Nithin Mathew, Irene J Beyerlein, Kaushik Dayal, and Abigail Hunter. A 3d phase field dislocation dynamics model for body-centered cubic crystals. *Computational Materials Science*, 171:109217, 2020.
- [PMB⁺20b] Xiaoyao Peng, Nithin Mathew, Irene J Beyerlein, Kaushik Dayal, and Abigail Hunter. A 3d phase field dislocation dynamics model for body-centered cubic crystals. *Computational Materials Science*, 171:109217, 2020.
- [PMG⁺15] S Piazzolo, M Montagnat, F Grennerat, H Moulinec, and J Wheeler. Effect of local stress heterogeneities on dislocation fields: Examples from transient creep in polycrystalline ice. *Acta Materialia*, 90:303–309, 2015.
- [PND20] Xiaoyao Peng, Dhriti Nepal, and Kaushik Dayal. Effective response of heterogeneous materials using the recursive projection method. *Computer Methods in Applied Mechanics and Engineering*, 364:112946, 2020.
- [QZS⁺19] D. Qiu, P. Zhao, C. Shen, W. Lu, D. Zhang, M. Mrovec, and Y. Wang. Predicting grain boundary structure and energy in bcc metals by integrated atomistic and phase-field modeling. *Acta Mater.*, 164:799–809, 2019.
- [Raa05] Dierk Raabe. Recrystallization simulation by use of cellular automata. In *Handbook of Materials Modeling*, pages 2173–2203. Springer, 2005.
- [RGG⁺13] R. Ravelo, T. C. Germann, O. Guerrero, Q. An, and B. L. Holian. Shock-induced plasticity in tantalum single crystals: Interatomic potentials and large-scale molecular-dynamics simulations. *Phys. Rev. B*, 88:134101, Oct 2013.
- [RGSM04] AD Rollett, G Gottstein, LS Shvindlerman, and DA Molodov. Grain boundary mobility—a brief review. *Zeitschrift für Metallkunde*, 95(4):226–229, 2004.

- [ROB⁺15] Sutatch Ratanaphan, David L Olmsted, Vasily V Bulatov, Elizabeth A Holm, Anthony D Rollett, and Gregory S Rohrer. Grain boundary energies in body-centered cubic metals. *Acta Materialia*, 88:346–354, 2015.
- [Roh11] Gregory S Rohrer. Grain boundary energy anisotropy: a review. *Journal of materials science*, 46(18):5881–5895, 2011.
- [RRWN17] Samit Roy, John Ryan, Samantha Webster, and Dhriti Nepal. A review of in situ mechanical characterization of polymer nanocomposites: Prospect and challenges. *Applied Mechanics Reviews*, 69(5):050802, 2017.
- [RZH⁺98] M. Rhee, H. M. Zbib, J. P. Hirth, H. Huang, and T. de la Rubia. Models for long-/short-range interactions and cross slip in 3d dislocation simulation of bcc single crystals. *Modelling and Simulation in Materials Science and Engineering*, 6:467–492, 1998.
- [SASG84] DJ Srolovitz, Michael P Anderson, Paramdeep S Sahni, and Gary S Grest. Computer simulation of grain growth—ii. grain size distribution, topology, and local dynamics. *Acta metallurgica*, 32(5):793–802, 1984.
- [SB01] YC Shu and K Bhattacharya. Domain patterns and macroscopic behaviour of ferroelectric materials. *Philosophical Magazine B*, 81(12):2021–2054, 2001.
- [SBA12] Alexander Stukowski, Vasily V Bulatov, and Athanasios Arsenlis. Automated identification and indexing of dislocations in crystal interfaces. *Modelling and Simulation in Materials Science and Engineering*, 20(8):085007, 2012.
- [Sch05] G. Schoeck. The peierls model: Progress and limitations. *Materials Science and Engineering A*, 400-401:7–17, 2005.
- [Sch17] Matti Schneider. An fft-based fast gradient method for elastic and inelastic unit cell homogenization problems. *Computer Methods in Applied Mechanics and Engineering*, 315:846–866, 2017.

- [SK93] Gautam M Shroff and Herbert B Keller. Stabilization of unstable procedures: the recursive projection method. *SIAM Journal on numerical analysis*, 30(4):1099–1120, 1993.
- [SLB⁺07] M. A. Shehadeh, G. Lu, S. Banerjee, N. Kioussis, and N. Ghoniem. Dislocation transmission across the cu/ni interface: a hybrid atomistic-continuum study. *Philosophical Magazine*, 87(10):1513–1529, 2007.
- [Sro86] DJ Srolovitz. Grain growth phenomena in films: A monte carlo approach. *Journal of Vacuum Science & Technology A: Vacuum, Surfaces, and Films*, 4(6):2925–2931, 1986.
- [Ste09] I. Steinbach. Phase-field models in materials science. *Model. Simul. Mater. Sci. Eng.*, 17:073001, 2009.
- [Stu09] Alexander Stukowski. Visualization and analysis of atomistic simulation data with OVITO—the Open Visualization Tool. *Modelling and Simulation in Materials Science and Engineering*, 18(1):015012–1–7; Also see <http://www.ovito.org/>, 2009.
- [Stu14] Alexander Stukowski. A triangulation-based method to identify dislocations in atomistic models. *Journal of the Mechanics and Physics of Solids*, 70(1):314–319, 2014.
- [Sut95] Adrian P Sutton. Interfaces in crystalline materials. *Monographs on the Physice and Chemistry of Materials*, pages 414–423, 1995.
- [SW03] C. Shen and Y. Wang. Phase field model of dislocation networks. *Acta Materialia*, 51(9):2595–2610, 2003.
- [TKC98] M. Tang, L. P. Kubin, and G. R. Canova. Dislocation mobility and the mechanical response of bcc single crystals: A mesoscopic approach. *Acta Materialia*, 46(9):3221–3235, 1998.

- [UW75] N. Urabe and J. Weertman. Dislocation mobility in potassium and iron single crystals. *Materials Science and Engineering*, 18:41–49, 1975.
- [Vit68] V. Vitek. Intrinsic stacking faults in body-centered cubic crystals. *Phil. Mag.*, 18(154):773–786, 1968.
- [Vit74] V. Vitek. Theory of core structures of dislocations in bcc metals. *Cryst. Latt. Defects*, 5:1, 1974.
- [VZM14] Jaroslav Vondřejc, Jan Zeman, and Ivo Marek. An fft-based galerkin method for homogenization of periodic media. *Computers & Mathematics with Applications*, 68(3):156–173, 2014.
- [WB11] Z. Q. Wang and I. J. Beyerlein. An atomistically-informed dislocation dynamics model for the plastic anisotropy and tension-compression asymmetry of bcc metals. *International Journal of Plasticity*, 27(10):1471–1484, 2011.
- [WBL07] Z. Q. Wang, I. J. Beyerlein, and R. LeSar. The importance of cross-slip in high-rate deformation. *Model. Simul. Mater. Sci. Eng.*, 15(6):675–690, 2007.
- [WBL08] Z. Q. Wang, I. J. Beyerlein, and R. LeSar. Slip band formation and mobile dislocation density generation in high rate deformation of single fcc crystals. *Philosophical Magazine*, 88:1321–1343, 2008.
- [WBT14] J. Wang, I. J. Beyerlein, and C. N. Tomé. Reactions of lattice dislocations with grain boundaries in mg: implications on the micro scale from atomic-scale. *International Journal of Plasticity*, 56:156–172, 2014.
- [WVdGN02] D. Weygand, L. H. Friedman, E. Van der Giessen, and A. Needleman. Aspects of boundary-value problem solutions with three-dimensional dislocation dynamics. *Model. Simul. Mater. Sci. Eng.*, 10:437, 2002.

- [Wil15] François Willot. Fourier-based schemes for computing the mechanical response of composites with accurate local fields. *Comptes Rendus Mécanique*, 343(3):232–245, 2015.
- [WJCK01] Y. U. Wang, Y. M. Jin, A. M. Cuitiño, and A. G. Khachaturyan. Nanoscale phase field microelasticity theory of dislocations: Model and 3D simulations. *Acta Materialia*, 49(10):1847–1857, 2001.
- [WScGI04] G. Wang, A. Strachan, T. Çağın, and W. A. Goddard III. Calculating the peierls energy and peierls stress from atomistic simulations of screw dislocation dynamics: application to bcc tantalum. *Model. Simul. Mater. Sci. Eng.*, 12:S371–S389, 2004.
- [WTF13] C. R. Weinberger, G. J. Tucker, and S. M. Foiles. Peierls potential of screw dislocations in bcc transition metals: Predictions from density functional theory. *Phys. Rev. B*, 87:054114, 2013.
- [YD11] Lun Yang and Kaushik Dayal. A completely iterative method for the infinite domain electrostatic problem with nonlinear dielectric media. *Journal of Computational Physics*, 230(21):7821–7829, 2011.
- [YLH13] H. Yang, Z. Li, and M. Huang. Modeling dislocation cutting the precipitate in nickel-based single crystal superalloy via the discrete dislocation dynamics with sif dissociation scheme. *Comp. Mater. Sci.*, 75:52–59, 2013.
- [ZBGW11] R. F. Zhang, I. J. Beyerlein, T. C. Germann, and J. Wang. Deformation twinning in bcc metals under shock loading: a challenge to empirical potentials. *Phil. Mag. Lett.*, 91(12):731–740, 2011.
- [ZBL11] C. Zhou, I. J. Beyerlein, and R. LeSar. Plastic deformation mechanisms of fcc single crystals at small scales. *Acta Materialia*, 59(20):7673–7682, 2011.
- [ZCK19] Y. Zeng, X. Cai, and M. Koslowski. Effects of the stacking fault energy fluctuations on the strengthening of alloys. *Acta Mater.*, 164:1–11, 2019.

- [ZdlRRH00] H. M. Zbib, T. D. de la Rubia, M. Rhee, and J. P. Hirth. 3d dislocation dynamics: Stress strain behavior and hardening mechanisms in fcc and bcc metals. *Journal of Nuclear Materials*, 276:154–165, 2000.
- [ZHBK16] Y. Zeng, A. Hunter, I. J. Beyerlein, and M. Koslowski. A phase field dislocation dynamics model for a bicrystal interface system: An investigation into dislocation slip transmission across cube-on-cube interfaces. *Inter. J. Plas.*, 79:293–313, 2016.
- [ZLZ⁺20] Jin Zhang, Wolfgang Ludwig, Yubin Zhang, Hans Henrik B Sørensen, David J Rowenhorst, Akinori Yamanaka, Peter W Voorhees, and Henning F Poulsen. Grain boundary mobilities in polycrystals. *Acta Materialia*, 191:211–220, 2020.
- [ZOAB11] H. M. Zbib, C. T. Overman, F. Akasheh, and D. Bahr. Analysis of plastic deformation in nanoscale metallic multilayers with coherent and incoherent interfaces. *International Journal of Plasticity*, 27(10):1618–1639, 2011.
- [ZRSOB17] Luis A. Zepeda-Ruiz, Alexander Stukowski, Tomas Oppelstrup, and Vasily V. Bulatov. Probing the limits of metal plasticity with molecular dynamics simulations. *Nature*, 550(7677):492–495, 2017.